Low Frequency Attenuation of Sound with Acoustic Metamaterials

Alexander James Dell

A thesis submitted in partial fulfilment of the requirements for the degree of
Doctor of Philosophy

The University of Sheffield
Faculty of Engineering
Department of Mechanical Engineering

Submission Date
August 2022

For my wife, Jasmine,
and my son, Lachlan.

Abstract

The work presented within this thesis pertains to the use of acoustic metamaterials for low frequency absorption and attenuation of sound. Acoustic metamaterials are structures composed of periodic and sub-wavelength locally resonant unit cells and are typically an order of magnitude or smaller than the associated wavelength of the frequency they are designed to manipulate. All naturally occurring materials have both positive mass density and bulk modulus; acoustic metamaterials have the ability to artificially manipulate these properties to have negative effective quantities dependant on the frequency of the incident acoustic wave.

Within this thesis, a general analytical method based upon the linear superposition of terms derived with the transfer matrix method are used to derive simple analytical expressions for complex acoustical systems. Good agreement is found when in comparison to results produced using the transfer matrix method and numerically. One limitation with the effective property models presented is the inability to capture the evanescent coupling between Helmholtz resonators.

The mechanism to achieve perfect absorption for one port systems has been explored with the development of single frequency and broadband frequency perfect absorbing acoustic metamaterial unit cells. Through the use of Helmholtz resonators with porous inclusions within their cavities, one port perfect absorbers have been developed that obtain perfect absorption at 290 Hz using a single Helmholtz resonator with a sample thickness of $\lambda/28$, and over a broadband frequency range between 275 and 625 Hz using a system of three Helmholtz resonators with a sample thickness of $\lambda/10$.

In a two port system, Helmholtz resonators with porous inclusions within the cavity have been utilised to achieve perfect absorption at a single frequency and over a broadband frequency range. The single frequency perfect absorber has a sample thickness of $\lambda/16$ at a frequency of 300 Hz. The broadband perfect absorber pre-

sented within this chapter exhibited perfect absorption at 312, 426 and 576 Hz, with a sample thickness of $\lambda/8$ at the lowest critically coupled frequency.

A method of simplification has been proposed for impedance terms derived by the transfer matrix method. This has been applied to the case of a serial array of M coupled identical Helmholtz resonators. The simplification method is reliant upon the use of an impedance contrast to create a small order term which can be used in the Taylor expansion of the impedance expressions. By utilising the leading order term from the Taylor series expansions, simple expressions were found composed of polynomials of the same order as M. It was also found that the resonant frequencies of the modelled systems can be obtained through the solution of the polynomials present within the numerator of the impedance approximations.

Finally, an ideal analytical model has been developed to model the acoustic attenuation achieved by periodic arrays of non-rigidly backed perforations acting as sound-soft scatterers. It has been shown that periodic arrays of sound soft scatterers produce a low frequency band gap from 0 Hz to a frequency determined by the geometry of the perforations and the unit cell length. Acoustic waves within the frequency range of the bandgap become evanescent, achieving large amounts of attenuation for finite systems, and no wave propagation for infinite systems. To confirm the existence of the low frequency band gap, an experimental setup to investigate the sound propagation in an open ended perforated pipe was designed. The experimental transmission loss highlights that periodically arranged holes in the rigid pipe create a low frequency band gap. The band gap produced experimentally matches the predictions obtained for the simplified numerical model in which the perforations were idealised with an acoustical soft backed elliptical geometry in the 3D finite element model.

Acknowledgements

I would sincerely like to thank my supervisor, Dr. Anton Krynkin, for all of his invaluable guidance, time and technical input throughout this research. Without his input, none of this research would be possible. I am especially grateful for his support in the final year of this project with the weekly early morning meetings, which were the only times I was available due to work commitments. My thanks also go to Professor Kirill Horoshenkov for the all of his useful guidance and suggestions which have been crucial in improving the outcomes of this research. I would also like to extend my gratitude to Gavin Sailor for undertaking the experimental aspect of this research. His input has been key in validating a key outcome of this thesis.

I would like to express my gratitude to Dr. Daniel Elford, Dr. Luke Chalmers and Dr. Richard Wilson at Sononbex Ltd who industrially sponsored this research. I am also grateful for all their useful discussions early on in this research. Special thanks must also be given to the EPSRC for the main funding of this research project.

Finally, I would like to thank all my family and friends who have supported me throughout this PhD, especially my wife, Jasmine, whose care and support has been fundamental in allowing me to complete this research.

Publications

Journal Publications

- A. Dell, A. Krynkin, K. V. Horoshenkov, and G. Sailor. Low frequency attenuation of acoustic waves in a perforated pipe. *The Journal of the Acoustical Society of America*, 153(3):1791–1801, Mar 2023.

- A. Dell, A. Krynkin, and K.V. Horoshenkov. The use of the transfer matrix method to predict the effective fluid properties of acoustical systems. *Applied Acoustics*, 182:108259, Nov 2021.

Journal Publications In Progress

- A. Dell, A. Krynkin. Approximation of Impedance of Identical Coupled Helmholtz Resonators.

Conference Proceedings

- A. Dell, A. Krynkin, K.V. Horoshenkov and G. Sailor. Low frequency attenuation of acoustic waves using sound-soft scatterers. *Inter-noise 2022*, Aug 2022.
- A. Dell, A. Krynkin, and K.V. Horoshenkov. Approximation of the effective fluid properties of a waveguide side-loaded by Helmholtz resonators. *e-Forum Acusticum 2020*, Dec 2020.
- A. Dell, A. Krynkin. Approximation of impedance in serial arrays of coupled Helmholtz resonators. *IOA Acoustics 2020*, Oct 2020.

Statement of Originality

I, the author, Alexander Dell confirm that this Thesis is my own work and that this work has not been previously presented for an award at this, or any other, university.

Contents

List of Figures

List of Tables

Chapter 1

Introduction

Noise is a pervasive issue in everyday life. Whether in an occupational setting with the use of tools and machinery, at home, in an office, or simply due to proximity to infrastructure such as roads, railways and airports; noise affects every facet of our day. It is well understood that chronic exposure to noise can produce both auditory and non-auditory health effects. Exposure to high noise levels can cause damage to hearing, even hearing loss in severe instances. It has also been shown that prolonged exposure to lower noise levels can lead to annoyance, sleep disruption and daytime sleepiness. All of which increase the occurrence of hypertension and cardiovascular disease [2]. Therefore, the subject of noise control spans a number of industrial sectors. From the design and manufacturing of cars and planes, the design of homes and offices, in the planning process for large infrastructure schemes such as wind farms and power stations, noise is a key consideration.

Generally, noise is a combination of direct sound from a source with the addition of any reflected sound from any nearby acoustically hard surfaces such as walls and buildings. Therefore, noise levels can either be reduced at the source or by altering the reflective properties of surfaces such that noise is either attenuated, absorbed or diffused. The most commonplace methodology for controlling noise is through the use of porous materials. These are typically used for the construction of enclosures and partition walls and can provide very good sound attenuation due to viscous and thermal losses within the pores of the material [3]. One limiting factor is that they become impractical at lower frequencies. This is due to the necessity for them to be of comparable size to the incident sound wavelength, as dictated by the mass density law [4]. This means that in the case of low frequencies, sound absorbers need to be excessively deep or dense to effectively dissipate the sound energy. Therefore, a structure which achieves low frequency sound absorption with a sample thickness much less than the wavelength being absorbed has numerous general and industrial applications. Herein, this type of system will be referred to as one port system, meaning that system is purely reflective with no transmission occurring.

Another source of noise is produced within ducting and ventilation systems. To control this noise, silencers are often employed as a lining to the ducts [4]. The attenuation of acoustic waves by silencers is typically achieved through the employment of rigidly backed cavities, connected to a main waveguide by a perforated panel. For silencers with partitioned cavities with a single perforation, i.e. a Helmholtz resonator, excellent attenuation can be achieved at the resonant frequency of the resonator. For silencers with empty cavities and panels composed of multiple identical perforations along the length of the silencer, a similar phenomenon occurs. If the perforated separating panel has a low porosity, a Helmholtz resonator type of attenuation occurs. As the porosity increases, the silencer behaves more like an expansion chamber [5]. In both cases, a limitation is the requirement for large cavity volumes, or narrow neck regions, to achieve low frequency attenuation. A large cavity volume is often impractical due to size constraints and having narrow regions often results in poor attenuation of acoustic waves due to large amounts of viscous and thermal losses overdamping the system. Therefore, a structure which achieves low frequency sound absorption/ attenuation with a sample thickness and geometry much less than the wavelength being altered, whilst still allowing airflow through the system, also has numerous general and industrial applications. Herein, this type of system will be referred to as a two port system, meaning that it is both reflective and transmissive and that airflow can pass through.

Acoustic Metamaterials

Acoustic metamaterials have come to the forefront in research in the past 20 years [6]. Starting out as an academic curiosity, they have quickly become a main focal point for research within the field of acoustics due to their far reaching industrial applications [7]. The term meta is a prefix used in the English language to indicate a concept that is an abstraction of another concept, an example being metadata – data about data. It then makes sense that metamaterials are artificial structures built up of small building blocks. The building blocks being meta-atoms, which when constructed together behave as one continuous material but with unconventional effective properties.

The concept of metamaterials shares its roots with composite materials; a material that is composed of other materials. For example, fibreglass is made up of glass fibres set in epoxy. The combination of materials allows for more desirable mechanical properties than the individual properties of the constituent materials that compose the composite. However, it is well understood that the mechanical properties of the composite fall within the bounds of its component materials [8]. Metamaterials are similar in the fact that they are a continuous material, like a composite, however they constitute of smaller elements which collectively produce effective material properties not present in the individual elements. Therefore the wave manipulation properties achieved by acoustic metamaterials supersede that of the properties of its constituent materials.

Acoustic metamaterials are composed of sub-wavelength locally resonant unit cells which can either be stand-alone, or periodic, and are typically an order of magnitude or smaller than the associated wavelength of the frequency they are designed to manipulate [9]. The key parameters acoustic metamaterials alter in an impinging sound wave are the mass density and bulk modulus [10]. All naturally occurring materials have both positive mass density and bulk modulus; acoustic metamaterials have the ability to artificially manipulate these properties to have negative effective quantities dependant on the frequency of the incident acoustic wave [11]. This allows for a multitude of possibilities such as acoustic lensing, cloaking, phase delay, active control and the absorption/ attenuation of low frequency sound with a sample thickness much less than the wavelength of sound being attenuated [1, 12]. A graphic displaying these possible uses can be found in Figure 1.1.

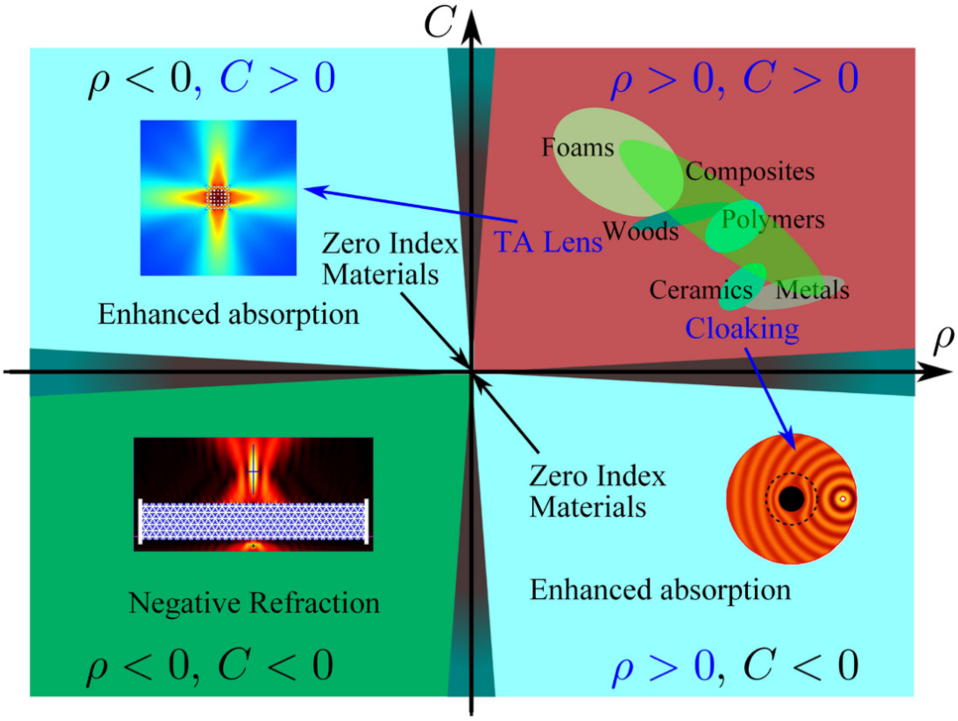

Figure 1.1: The material design space for acoustic metamaterials, where ρ is the effective dynamic density and C is the effective dynamic compressibility (inverse of bulk modulus), as presented in [1]. The top right quadrant depicts the design space for conventional acoustic materials, with the three remaining quadrants having one or both negative effective dynamic fluid properties. These properties can only be achieved dynamically. For instance, Helmholtz resonators driven at their resonance frequency achieve negative dynamic compressibility. The three devices shown employ the metamaterial effects of negative refraction, transformation acoustics, and cloaking.

Of particular interest for this thesis are acoustic metamaterials which can achieve broadband low frequency noise absorption and attenuation in one and two port systems, with a sample length much smaller than the wavelength being manipulated. This thesis will explore; the analytical models required to obtain expressions for the effective material properties of metamaterial structures; one and two port perfect absorbers; and acoustic metamaterial structures which achieve very low frequency attenuation of noise in waveguides through the exploitation of the negative dynamic fluid properties exhibited by acoustic metamaterials.

One Port Systems

For one port systems, perfect absorption has been shown to be possible through the coupling of a Helmholtz and membrane resonators by tuning the interplay of losses within the system such that the critical coupling condition is fulfilled [13]. This states that when the energy leakage of a resonant system is equal to the inherent losses within the system, all incident acoustic energy is absorbed [14]. It has also been shown that a unit cell composed of a smaller waveguide structure side-loaded by Helmholtz resonators can achieve perfect absorption omni-directionally [15]. This was achieved through the coupling of identical Helmholtz resonators such that the critical coupling condition was fulfilled by the accumulation of 'slow sound' [16, 17, 18], where each subsequent resonator in a series reduces the speed of sound such that very low frequency resonators absorb with much greater efficacy than if the speed of sound was unaltered.

Through the use of multiple resonances within a one port structure it is possible to obtain singular [19, 20] and broadband [21, 22] perfect absorption for sample thickness much less than the wavelength being absorbed. The tuning of one port systems composed of Helmholtz resonators can also be done through the use of porous media within the cavity, allowing for the losses within the system to be adjusted such that the critical coupling condition is fulfilled [14]. Alternatively, it has been shown that embedding Helmholtz resonators within a porous layer can also achieve perfect absorption [23, 24].

The mechanism for perfect absorption can also be visualised with the complex frequency plane analysis method [14, 25, 26]. This is a graphical procedure which can be used to display the eigenvalues or eigenvector components of systems in the complex frequency plane. This provides useful information for the optimisation of systems to achieve perfect absorption as it can be used to determine how the addition or reduction of losses in the system will change the absorption coefficient. Some examples on the use of the complex frequency plane to achieve perfect absorption for subwavelength sized, anechoic termination type systems include those composed of resonant building blocks [16, 15], membranes [27], porous membranes [13], decorated membranes [28], bubble metascreens [29] and aerogels [30].

Two Port Systems

To date, a number of methodologies have been employed to achieve perfect absorption in two port systems. For example, two port perfect absorption has been realised through a process of 'coherent perfect absorption', which is enabled by the control of input acoustic waves in both propagative directions [31]. Through the use of a subwavelength resonant metamaterial structure, the effective acoustic properties can be tuned such that perfect absorption can be achieved. This requires the manipulation of the relative phase between impinging acoustic waves and allows for the absorption coefficient to be tuned from zero to unity [32]. It has also been shown that low frequency perfect absorption can be achieved through the use of elastic membranes decorated with asymmetric rigid platelets which act as the oscillating mass [33].

There is also a significant body of work on the analysis of Bloch wave propagation through periodic arrays of Helmholtz resonators [34, 35, 36]. Based on the Bloch wave analysis of infinitely periodic systems of Helmholtz resonators, it has been shown that the bandgap dispersion effect on the acoustic wavenumber is also evident within finite systems [37, 38]. This work has lead to design of a system which achieve negative bulk modulus through the implementation of periodic arrays of HRs in the ultrasonic regime [39] and is also useful in when designing systems in the low frequency regime [40, 18].

The absorptive properties of two port structures can typically be simplified into two types of systems. Those that exhibit asymmetrical sound absorption properties, and those that are mirror symmetric and exhibit symmetrical sound absorption properties. There has been a large body of work on achieving perfect absorption with systems that exhibit asymmetrical absorptive properties [41].

As the maximum absorption coefficient attainable for one-sided absorption by a point symmetric scatterer is $\alpha = 0.5$ [31], multiple resonances are typically required to achieve perfect absorption. This can be achieved through the degenerate coupling of Helmholtz resonators in which a detuning parameter can be utilised such that strong coupling between the Helmholtz resonators is achieved and an impedance match condition is met for a single propagative direction [42]. When this directional impedance match condition is met, this same boundary acts as an acoustically soft boundary in the opposing direction, resulting in near-perfect reflection. As these types of systems are typically reciprocal in nature, the transmission coefficient does not vary with propagation direction [43]. Therefore, the duality of the impedance matching condition coinciding with a sound soft boundary in the opposing propagative direction is required to maintain an equal transmission coefficient for both propagative directions [44].

Through the use of multiple degeneratively coupled resonators, it has been shown that perfect and broadband absorption can be achieved over a large range of frequencies with rainbow trapping using both Helmholtz resonators [45] and quarter wavelength resonators [46]. It is also possible to use multiple pairs of detuned degeneratively coupled Helmholtz resonators at targeted frequencies to achieve asymmetric perfect absorption [42, 44, 47]. Other resonant structures such as microperforated panels [48] can be utilised to the same effect. Additionally, it has been shown that through the use of degeneratively coupled resonators and waveguides, mirror symmetric perfect absorption can be achieved in optics [49] and acoustics through the use of Helmholtz resonators [50] and with coupled membrane resonators [51].

Through the use of a metamaterial consisting of an array of open backed perforations along a waveguide, where no cavities are present, it has been theoretically and experimentally shown that negative bulk modulus can be obtained from zero to an upper bound [52]. This is due to the non-local resonant effect of the perforations allowing for the occurrence of a bandgap where zero transmission occurs and where the bandgap upper bound is determined by the system geometry. This has been corroborated in the non-linear regime through the employment of high amplitude excitation [53] and it has also been shown that through the coupling of the perforations within an array of elastic membranes, both negative bulk modulus and dynamic density can be achieved [54].

Thesis Layout

The aims of this thesis are to investigate and develop broadband low frequency acoustic metamaterials for noise absorption and attenuation in one and two port systems, with a sample length much smaller than the wavelength being manipulated; develop analytical models to obtain simple expressions for the effective material properties of metamaterial structures to help gain an insight into the underlying physics; and to develop an acoustic metamaterial structure for very low frequency attenuation of noise in waveguides through the exploitation of the negative dynamic fluid properties acoustic phenomenon exhibited by acoustic metamaterials.

This thesis is organised as follows: Chapter 1 is the introduction and provides context for the work present herein. Chapter 2 provides the necessary theory and mathematical framework that has been used throughout this thesis. Chapter 3 presents a general analytical model to obtain the effective fluid properties of complex symmetric acoustical systems. Chapter 4 explores the use of Helmholtz resonators with porous inclusions to achieve perfect absorption at a single frequency and over a broadband frequency range for one port systems. Chapter 5 explores the use of Helmholtz resonators with porous inclusions to achieve perfect absorption at a single frequency and over a broadband frequency range for two port systems. Chapter 6 presents a method of approximating systems of identical Helmholtz resonators through the impedance contrast between the resonator neck and cavity, with a discussion on the viability of coupled identical Helmholtz resonators for low frequency perfect absorption. Chapter 7 describes the novel phenomenon of open backed perforations along a waveguide acting as sound-soft scatterers, enabling very low frequency attenuation of acoustic waves. Experimental evidence of this phenomenon is presented. Chapter 8 is the conclusion.

Chapter 2

Theory

In his chapter, the underlying theory used throughout this thesis will be set out. This begins with an introduction to the fundamental equations used throughout, Helmholtz resonators and Phononic crystals. The effective fluid property models that account for viscous and thermal effects in varying acoustic media will then be detailed. These form the basis in which the analytical models developed within this thesis are built upon. The transfer matrix method will be shown. This provides the methodology for which all the analytical models have been developed with throughout this thesis. Finally, the numerical methods used for validation throughout this thesis will be described.

2.1 Basic Equations

Consider a one-dimensional harmonic plane wave with $\mathrm{e}^{\mathrm{i}\omega t}$ time dependence (Noting that this time dependence will be used throughout this thesis), where $\mathrm{i} = \sqrt{-1}$, which propagates in a duct of stationary ideal gas with a cross sectional area S_a. The macroscopic pressure gradient $-\partial p/\partial x$ is applied to a medium in the x direction, where p is the complex acoustic pressure amplitude at any point. The equation of motion is written as follows [55]:

$$-\frac{\partial p}{\partial x} = \mathrm{i}\omega\rho(\omega)v, \tag{2.1}$$

where $\rho(\omega)$ is the effective frequency dependent dynamic fluid density, ω is the angular frequency and v is the complex average macroscopic fluid velocity in the x direction. For a small perturbation in the medium, the following expressions can be written based on the continuity and thermodynamic state equations [55], respectively:

$$\rho_0 \frac{\partial v}{\partial x} + \mathrm{i}\omega \delta\rho = 0, \tag{2.2}$$

$$\frac{\delta\rho}{\rho_0} = C(\omega)p. \tag{2.3}$$

Here we adopt notations similar to those used in ref. [55] so that ρ_0 is the equilibrium density, $\delta\rho$ is the perturbation density and $C(\omega)$ is the effective complex compressibility of the fluid. Note that the effective bulk modulus $K(\omega)$ is simply the inverse of the complex compressibility, i.e. $1/C(\omega)$. The combination of equations (2.2) and (2.3) leads to:

$$-\frac{\partial v}{\partial x} = \mathrm{i}\omega C(\omega)p. \tag{2.4}$$

Equations (2.1) and (2.4) result in the following wave equation:

$$\frac{\partial^2 p}{\partial x^2} = -\omega^2 \rho(\omega)C(\omega). \tag{2.5}$$

Subsequently, the effective dynamic fluid density and complex compressibility can be used to obtain the characteristic impedance, $Z(\omega)$, and acoustic wavenumber, $k(\omega)$, respectively:

$$Z(\omega) = \frac{1}{S_a}\sqrt{\frac{\rho(\omega)}{C(\omega)}}, \tag{2.6}$$

$$k(\omega) = \omega\sqrt{\rho(\omega)C(\omega)}. \tag{2.7}$$

The speed of sound, $c(\omega)$, can then be found simply as:

$$c(\omega) = \left[\rho(\omega)C(\omega)\right]^{-1/2}. \tag{2.8}$$

These basis equations provide the foundation to obtain the effective fluid properties of an acoustical system.

2.2 Helmholtz Resonators

Helmholtz resonators (HRs) are a specific type of acoustic resonator which are particularly useful in the control of audible harmonic sound waves. One such use is the attenuation of tonal noise within ducts/ pipes, such as in a muffler for a car exhaust [56]. Additionally, as the resonance is not dependant on standing wave formation within the structure, HRs can resonate at frequencies that have much longer wavelengths than the physical dimensions of the HR itself. This is a large contributing factor as to why HRs have become particularly prevalent within the design of acoustic metamaterials, which by definition are sub-wavelength in size and dimensions.

Helmholtz resonators consist of two main features; a rigid walled cavity, and a neck that typically protrudes out from the cavity. Due to this configuration, HRs resonate at a specific frequency, similar to a mass-spring system. The air within the neck of the resonator acts as the oscillating mass and the adiabatic compression of the air within the cavity provides the spring constant. When an acoustic wave is incident on the Helmholtz resonator, it acts as a force, causing the mass of air in the neck to displace. As the mass moves down, it reduces the cavity volume, increasing the pressure inside the cavity. This occurs until the pressure is great enough to recoil the mass. Once the atmospheric pressure is greater than the cavity pressure, the mass is then forced back in to the cavity, repeating the process. Figure 2.1 shows this process.

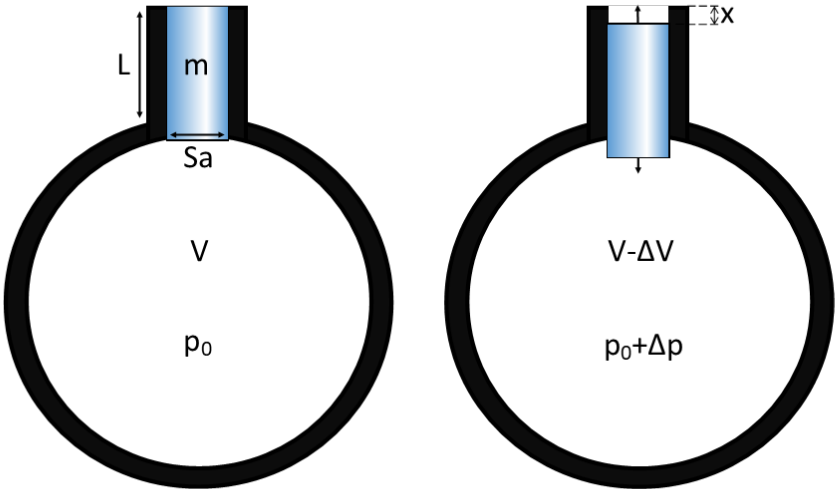

Figure 2.1: Schematic of a Helmholtz resonator at resonance

The mass of air within the neck is simply $m = \rho S_a L$, where ρ is the fluid density, S_a is the cross sectional area of the neck and L is the length of the neck. Using the ideal gas law, it is possible to derive the following expression which relates the pressure change, Δp, with the change in volume, ΔV:

$$\frac{\Delta p}{p_0} = -\gamma \frac{\Delta V}{V}, \tag{2.9}$$

where γ is the ratio of specific heats. Furthermore, it is evident that $\Delta V = S_a x$, where x is the distance travelled by the oscillating mass of air within the neck. This results in the following expression:

$$\frac{\Delta p}{p_0} = -\gamma \frac{S_a x}{V}, \tag{2.10}$$

with the resulting net force on the oscillating fluid mass being:

$$F = \Delta p S_a = -\gamma \frac{S_a^2 x}{V} p_0. \tag{2.11}$$

Using Newton's second law of motion, $F = m\ddot{x}$, gives us:

$$\ddot{x} = \frac{F}{m} = -\gamma \frac{S_a p_0}{\rho L V} x. \tag{2.12}$$

If the mass oscillates harmonically, then $\ddot{x} = -\omega^2 x$, meaning the frequency of oscillation is given by:

$$f_0 = \frac{1}{2\pi}\sqrt{\frac{\gamma S_a p_0}{\rho L V}} = \frac{c}{2\pi}\sqrt{\frac{S_a}{LV}}, \tag{2.13}$$

where the speed of sound is $c = \sqrt{\frac{\gamma p_0}{\rho}}$.

It must be stated that this model is simplified. Typically, the oscillating mass of air encompasses a volume greater than the length of the neck. This is due to pressure radiation at the discontinuities between the neck and the cavity/ surrounding medium [57]. As a result, length corrections must be added to the length of the neck. These vary with resonator geometry. Additionally, this model neglects the contribution of damping, which occurs in the neck and cavity due to the visco-thermal losses produced by the viscous and thermal boundary layers.

2.3 Phononic Crystals

Phononic crystals are periodic structures composed of two different elastic materials. The main quality of these structures is that mechanical waves are unable to propagate through the structure at designated frequencies [58, 59]. These frequency ranges are known as bandgaps and are determined by the geometry of the structure, e.g. lattice constant and unit cell structure [60]. To understand the mechanism behind this, it is important to recall some fundamentals from crystalline structures [61].

An ideal crystal is constructed by an infinite repetition of identical groups of atoms. These groups of atoms are known as the basis and the set of mathematical points in which the basis resides is known as the Bravais lattice. A 2D Bravais lattice consists of all points with position vectors, R, of the form $R = n_1 a_1 + n_2 a_2$. The vectors a_i, where $i = 1, 2$, are called primitive vectors and they generate the lattice. For any given Bravais lattice, the set of primitive vectors is not unique, there are in fact infinitely many choices. Figure 2.2 highlights a few examples.

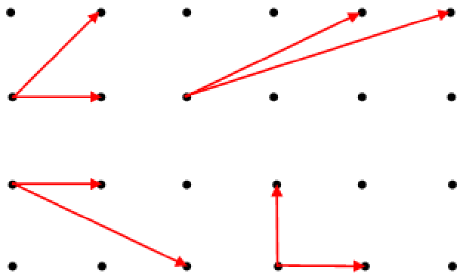

Figure 2.2: Examples of some possible primitive vectors on a 2D Bravais lattice.

A volume of space that, when translated through all the vectors within the Bravais lattice, fills all the space, without any overlapping or the creation of voids, is known as the primitive unit cell. There must be exactly one lattice point per unit cell. This is exemplified in figure 2.3.

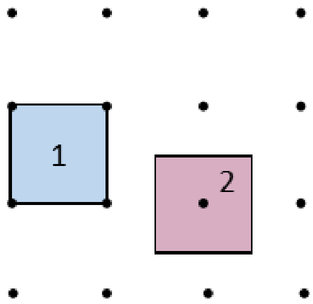

Figure 2.3: Two examples of primitive cells on a 2D Bravais lattice.

Cell one is simply a primitive unit cell whereas cell two is known as the Wigner-Seitz primitive cell. The Wigner-Seitz primitive cell of the reciprocal lattice is known as the first Brillouin zone. This is in the frequency domain. Figure 2.4 outlines the first three Brillouin zones for a square lattice and shows how the irreducible Brillouin zone can be constructed within the first zone [61].

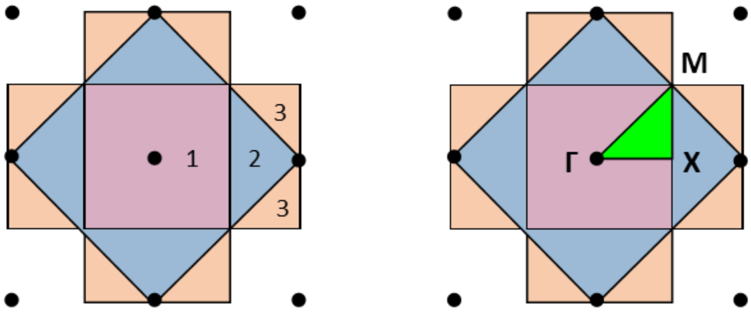

Figure 2.4: First three Brillouin zones of a square lattice (left) and the irreducible Brillouin zone of a square lattice (right).

The irreducible Brillouin zone is formed by reducing the first zone through all of its symmetries. All the information within the first Brillouin zone is also contained within the irreducible Brillouin zone. The importance of the Brillouin zone comes from Bloch waves and how they can be used to describe wave propagation in periodic medium. This states that as a plane wave propagates through a periodic structure, it only changes by a periodic modulation [62]. This is described with the following equation, where time dependence is omitted for simplicity, and q is the Bloch wavevector:

$$p(r+R) = p(r)\mathrm{e}^{iqR}. \tag{2.14}$$

Here, $p(r)$ is a periodic function of the same periodicity as the reciprocal lattice. Incidently, Bloch's theorem is equivalent to Floquet's theorem [63] when applied to a linear wave equation with periodically varying mechanical properties.

The most common method to describe band structures, formed by wave propagation through a periodic medium, is through the use of the dispersion relationship. This describes the relationship between the angular frequency, ω, and the Bloch wavevector, q. If the primitive lattice vector, R_i, denotes the periodicity of the medium, the envelope function f has the same periodicity, $f(x+R_1) = f(x)$. In the same way, such an envelope function can be found for q, which is also periodic, such that $f(q+G_i) = f(q)$, where G_i is the primitive lattice vectors of the reciprocal lattice. The direct and reciprocal lattice vectors obey an orthogonality condition such that $R_i G_i = 2\pi\delta_{ij}$, where δ_{ij} is the kronecker delta symbol. Due to the periodicity of the wavevector, it is only necessary to compute the values for q within the first primitive cell, i.e. the irreducible Brillouin zone.

For example, in a 1D system of periodicity, a, the primitive reciprocal lattice vector is $G_1 = \frac{2\pi}{a}$. The irreducible Brillouin zone then encompasses the region $[\frac{-\pi}{a}, \frac{\pi}{a}]$ [64]. All wavevectors are equivalent to those in this zone when translated by some multiple of G_1. A plot comparing the dispersion relationship of a one dimensional linear homogenous medium and a one dimensional periodic system can be seen in Figure 2.5.

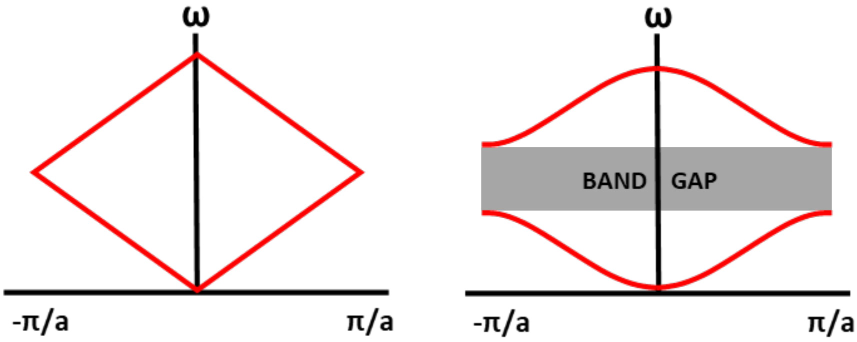

Figure 2.5: Dispersion relationship of a 1D linear homogenous system (left) and a 1D periodic system (right).

For the homogenous case, the dispersion relationship is simply a linear function, $\omega = ck$. For the periodic case, it can be defined as $\omega = c(\omega)k$. In both cases the bands fold back to fit the irreducible Brillouin zone. The frequency of the Bragg bandgap is determined by $f_r = c/2a$ and the width of the bandgap is a function of the filling fraction of the scatterers within the system.

In general, when a mechanical wave at a frequency within the bandgap frequency is incident, the wave is totally reflected. This is due to Bragg scattering of the wave at the interfaces between the different materials [65]. The interaction of the incident and reflected waves creates a splitting of the dispersion relationship. This is due to interference effects within the crystal such as the interaction of waves with the same wavevectors but propagating in opposite directions, forming standing waves.

These by definition have a vanishing group velocity, such that $v_g = \partial\omega/\partial k = 0$, implying there is a horizontal tangent to the dispersion curve at the Brillouin zone boundary, or in other words, the formation of a bandgap [64]. It must be noted that for the work presented herein, the target frequencies are such that they are unsuitable for the utilisation of Bragg bandgaps due to the separation distance required for unit cells. For example, to obtain a bandgap at 1000 Hz, the separation distance required between two unit cells is 17 cm. This is too large for the applications presented within this thesis when considering many unit cells are required to create a Bragg bandgap.

2.4 Effective Fluid Property Models

2.4.1 Viscous and Thermal Losses

Viscous and thermal (viscothermal) losses for the analytical acoustical models presented herein are accounted for by evaluating the complex frequency dependent density, ρ_{eff}, and bulk modulus, K_{eff}, for a plane wave propagating through a section of constant cross section [66].

For a circular duct of radius r these are expressed as:

$$\rho_{eff}(\omega) = \rho_0 \left[1 - \frac{2J_1(rG_r)}{rG_r J_0(rG_r)}\right], \tag{2.15}$$

$$K_{eff}(\omega) = K_0 \left[1 + (\gamma - 1)\frac{2J_1(rG_k)}{rG_k J_0(rG_k)}\right]. \tag{2.16}$$

Here $G_r = \sqrt{-\mathrm{i}\omega\rho_0/\eta}$ and $G_k = \sqrt{-\mathrm{i}\omega\rho_0 Pr/\eta}$, in which ρ_0 is the equilibrium density, $K_0 = \gamma P_0$ is the adiabatic bulk modulus, γ is the ratio of specific heats, P_0 is the equilibrium pressure, Pr is the Prandtl number and η is the dynamic viscosity. Additionally, J_0 and J_1 are Bessel functions of the first kind.

For a rectangular duct of width, a, and height, b:

$$\rho_{eff}(\omega) = \frac{\rho_0 a^2 b^2}{4G_\rho^2 \sum_{k=0}^{\infty}\sum_{m=0}^{\infty}\left[\alpha_k^2\beta_m^2\left(\alpha_k^2 + \beta_m^2 + G_\rho^2\right)\right]^{-1}}, \tag{2.17}$$

$$K_{eff}(\omega) = \frac{K_0}{\gamma - 4(\gamma-1)G_K^2/a^2b^2 \sum_{k=0}^{\infty}\sum_{m=0}^{\infty}\left[\alpha_k^2\beta_m^2\left(\alpha_k^2+\beta_m^2+G_K^2\right)\right]^{-1}}, \tag{2.18}$$

where $G_\rho = \sqrt{\mathrm{i}\omega\rho_0/\eta}$, $G_K = \sqrt{i\omega\rho_0 Pr/\eta}$, $\alpha_k = 2(k+1/2)\pi/a$ and $\beta_m = 2(m+1/2)\pi/b$, where k and m are integers in this instance. The infinite sums are computed numerically with a truncation number of 100 and an accuracy of 5 significant figures for a range of duct dimensions. Using these expressions it is then possible to calculate the characteristic impedance and acoustic wavenumber for a fluid layer.

The properties of air at normal conditions used throughout this thesis are presented in Table 2.1.

η	$1.983e-5$ [kg/ms]
γ	1.4
Pr	0.702
P_0	101320 [N/m^2]
μ	$15.68e-6$ [m$^2/s$]

Table 2.1: Properties of air at normal conditions.

2.4.2 Johnson-Champoux-Allard Model

This approach considers the layer of porous material in the rigid frame approximation as a layer of equivalent fluid. To calculate the effective parameters of the porous layer, five macroscopic parameters of the porous material are required; porosity, Ω, tortuosity, α_∞, static airflow resistivity, σ,viscous characteristic length, Λ and the thermal characteristic length Λ'.

For clarity; porosity is a measure of the amount of void (empty space) within a material in comparison to the total volume. Tortuosity is a measure of the sinuosity and interconnectivity between pores. The static airflow resistivity expresses the level of frictional resistance to an acoustic wave propagating through air that is at rest within the pores. The viscous characteristic length is a measure of how viscous effects influence wave propagation, and is related to the size of the inter-connection between two pores. Finally, the thermal characteristic length is a measure of how thermal effects influence wave propagation, and is related to the maximum sizes of the pores.

The equations for the effective frequency dependant density and bulk modulus, are found using the following expressions, respectively [3]:

$$\rho_{eff}(\omega) = \frac{\alpha_\infty \rho_0}{\Omega}\left(1 - \mathrm{i}\frac{\omega_c}{\omega}F(\omega)\right), \tag{2.19}$$

$$K_{eff}(\omega) = \frac{1}{\Omega}\left(\frac{\gamma P_0}{\gamma - (\gamma - 1)\big(1 - \mathrm{i}8\eta G(P_r\omega)/P_r\omega\Lambda'^2\rho_0\big)^{-1}}\right). \tag{2.20}$$

Where

$$\omega_c = \frac{\sigma\Omega}{\rho_0\alpha_\infty}. \tag{2.21}$$

The functions $F(\omega)$ and $G(P_r\omega)$ are corrections introduced by Johnson [67] and by Champoux and Allard [68], respectively. These are given by:

$$F(\omega) = \sqrt{1 + \mathrm{i}\frac{4\eta\rho_0\alpha_\infty^2}{\Omega^2\sigma^2\Lambda^2}\omega}, \tag{2.22}$$

and

$$G(P_r\omega) = \sqrt{1 + \mathrm{i}\frac{\rho_0\Lambda'^2 P_r\omega}{16\eta}}. \tag{2.23}$$

Throughout this thesis, any implementation of porous media is undertaken using the JCA method with the properties of melamine foam presented in Table 2.2.

Ω	0.99
α_∞	1.02
σ	11000 [Nsm^{-4}]
Λ	$160e-6$ [m]
Λ'	$220e-6$ [m]

Table 2.2: Macroscopic parameters of melamine foam.

2.5 Champoux and Stinson Rigid Frame Model

Consider a bulk sample of identical pores with total cross section S and total length L. Here L is sufficiently large to cover all variation of pore cross section, but small enough such that L is much smaller than the acoustic wavelength in the pore space. Within a single pore, there are M segments. Each segment, m, has a length $l^{(m)}$ and an area $S_a^{(m)}$. A schematic of a single tortuous pore can be seen in Figure 2.6.

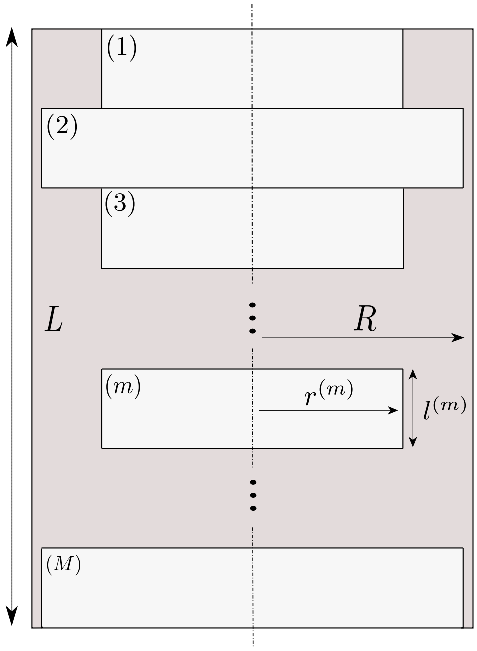

Figure 2.6: Schematic of a sample containing a single tortuous pore.

It has been shown from the linear superposition of terms within each segment that the effective dynamic density $\rho_{eff}(\omega)$ and complex compressiblity $C_{eff}(\omega)$ can be obtained as follows [55]:

$$\rho_{eff}(\omega) = \alpha_\infty \frac{\displaystyle\sum_{m=1}^{M} \rho(\omega)^{(m)} l^{(m)} / S_a^{(m)}}{\displaystyle\sum_{m=1}^{M} l^{(m)} / S_a^{(m)}}, \tag{2.24}$$

$$C_{eff}(\omega) = \frac{\displaystyle\sum_{m=1}^{M} C(\omega)^{(m)} S_a^{(m)} l^{(m)}}{\displaystyle\sum_{m=1}^{M} S_a^{(m)} l^{(m)}}. \tag{2.25}$$

Provided the geometry, dynamic density and complex compressibility are known for each pore section, it is possible to obtain the effective properties for the total system. Finally, the characterisitc impedance of the bulk material is given by

$$Z_{eff}(\omega) = \frac{1}{\Omega S} \left[\frac{\rho_{eff}(\omega)}{C_{eff}(\omega)} \right]^{1/2}, \tag{2.26}$$

where $\Omega = \displaystyle\sum_{m=1}^{M} S_a^{(m)} l^{(m)} / (SL)$ is the porosity of the sample.

2.6 The Transfer Matrix Method

2.6.1 Basic Formulation

The transfer matrix method (TMM) provides the relationship between the initial sound pressure, p, and volume flux, $V = vS_a$, where S_a is the cross sectional area, at the start and at the end of a medium in a duct [3]. To differentiate between the initial and end properties, the subscripts $x = 0$ and $x = -L$ are used, respectively. The transfer matrix, T, is derived under the assumption that only plane waves propagate through the medium in the $-\mathrm{i}kx$ direction, meaning it provides the solution for a 1D wave propagation problem. The general formulation of the transfer matrix is as follows;

$$\begin{bmatrix} p \\ V \end{bmatrix}_{x=0} = T \begin{bmatrix} p \\ V \end{bmatrix}_{x=-L} = \begin{bmatrix} T_{11} & T_{12} \\ T_{21} & T_{22} \end{bmatrix} \begin{bmatrix} p \\ V \end{bmatrix}_{x=-L} . \tag{2.27}$$

This is graphically depicted for a single fluid layer within Figure 2.7.

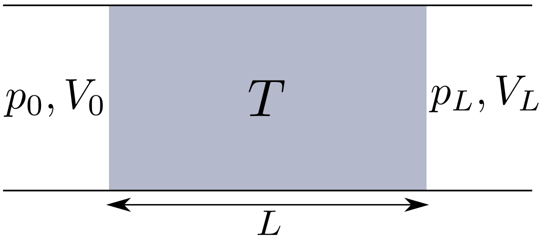

Figure 2.7: Graphical depiction of the TMM applied to a single fluid layer.

For a pressure wave incident on a fluid layer of thickness, L, and characteristic impedance, $Z = \rho c/S_a$, the pressure and acoustic particle velocity are written as follows;

$$p(x) = Ae^{-\mathrm{i}kx} + Be^{\mathrm{i}kx}, \tag{2.28}$$

$$V(x) = \frac{1}{Z}(Ae^{-\mathrm{i}kx} - Be^{\mathrm{i}kx}), \tag{2.29}$$

where A and B are the amplitudes of the incident and reflected waves, respectively. When $x = 0$, the pressure and particle velocity can be expressed as

$$p(0) = A + B, \tag{2.30}$$

$$V(0) = \frac{1}{Z}(A - B). \tag{2.31}$$

Correspondingly, when $x = -L$, the pressure and acoustic particle velocity are:

$$p(-L) = (A + B)cos(kL) - \mathrm{i}(A - B)sin(kL), \tag{2.32}$$

$$V(-L) = \frac{1}{Z}((A - B)cos(kL) - \mathrm{i}(A + B)sin(kL)). \tag{2.33}$$

Substitution of equations 2.30 and 2.31 into equations 2.32 and 2.33 yields the expressions

$$p(-L) = cos(kL)p(0) - \mathrm{i}Zsin(kL)V(0), \tag{2.34}$$

$$V(-L) = cos(kL)V(0) - \mathrm{i}\frac{sin(kL)}{Z}p(0). \tag{2.35}$$

When rearranged into matrix form and inverting, the transfer matrix for a fluid layer becomes:

$$\begin{bmatrix} p \\ V \end{bmatrix}_{x=0} = \begin{bmatrix} \cos(kL) & \mathrm{i}Z\sin(kL) \\ \frac{\mathrm{i}}{Z}\sin(kL) & \cos(kL) \end{bmatrix} \begin{bmatrix} p \\ V \end{bmatrix}_{x=-L} = \begin{bmatrix} T_{11} & T_{12} \\ T_{21} & T_{22} \end{bmatrix} \begin{bmatrix} p \\ V \end{bmatrix}_{x=-L}. \tag{2.36}$$

For a multilayered structure, as shown in Figure 2.8, the relationship between the input and output pressure and acoustic flux are obtained by the multiplication of the transfer matrices of each layer.

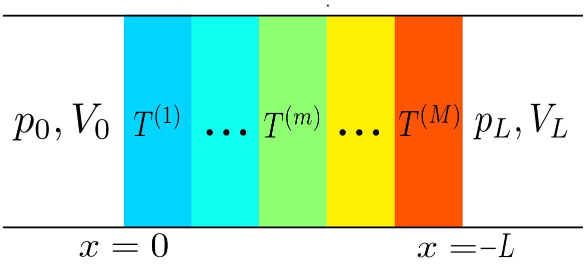

Figure 2.8: Graphical depiction of the TMM approach applied to a multilayered fluid.

This is expressed as

$$T = \prod_{m=1}^{M} T^{(m)}, \tag{2.37}$$

where M denotes the total amount of layers.

2.6.2 Reflection Properties of One-Port Systems

A one port system is an acoustical system that is purely reflective such that no transmission of acoustic waves occurs. To determine the reflection properties of a one-port system, it is required to obtain the surface impedance. Consider an effective fluid layer of the following form:

$$\begin{bmatrix} p \\ V \end{bmatrix}_{x=0} = \begin{bmatrix} cos(k_{eff}L) & iZ_{eff}sin(k_{eff}L) \\ \frac{i}{Z_{eff}}sin(k_{eff}L) & cos(k_{eff}L) \end{bmatrix} \begin{bmatrix} p \\ V \end{bmatrix}_{x=-L} = \begin{bmatrix} T_{11} & T_{12} \\ T_{21} & T_{22} \end{bmatrix} \begin{bmatrix} p \\ V \end{bmatrix}_{x=-L} . \tag{2.38}$$

If a system has one port then there is a velocity termination at the rigid boundary at the end of the system. This is facilitated by the multiplication of the final transfer matrix of the system by $[1, 0]^T$. The surface impedance of the system, Z_s, is then simply

$$Z_s = \frac{P_{x=0}}{V_{x=0}} = \frac{T_{11}}{T_{21}}. \tag{2.39}$$

For an effective fluid layer this results in

$$Z_s = iZ_{eff}\,\text{cot}(k_{eff}L). \tag{2.40}$$

The reflection coefficient,R, is then obtained as

$$R = \frac{Z_w - Z_s}{Z_w + Z_s}, \tag{2.41}$$

where Z_w is the waveguide characteristic impedance. The absorption coefficient is then simply

$$\alpha = 1 - |R|^2. \tag{2.42}$$

2.6.3 Transmission Properties of Two Port Systems

A two port system is an acoustical system which is both reflective and also transmissive. For a non-isotropic and asymmetric system, where the transmission and reflection of the incident plane wave are dependent on the direction of entry to the system, expressions can be obtained for the transmission, reflection and absorption coefficients [69]. When the incident wave propagates in the $-\mathrm{i}kx$ direction, these are:

$$R^- = \frac{T_{11} + T_{12}/Z_0 - Z_0T_{21} - T_{22}}{T_{11} + T_{12}/Z_0 + Z_0T_{21} + T_{22}}. \tag{2.43}$$

$$T^- = \frac{2\mathrm{e}^{-\mathrm{i}kL}}{T_{11} + T_{12}/Z_0 + Z_0T_{21} + T_{22}}, \tag{2.44}$$

$$\alpha^- = 1 - |R^-|^2 - |T^-|^2, \tag{2.45}$$

where the superscript $-$ indicates these expressions are calculated with respect to an incoming wave of $-\mathrm{i}kx$ direction. Similarly, when the incident wave propagates in the $+\mathrm{i}kx$ direction, these are:

$$R^+ = \frac{-T_{11} + T_{12}/Z_0 - Z_0 T_{21} + T_{22}}{T_{11} + T_{12}/Z_0 + Z_0 T_{21} + T_{22}}. \tag{2.46}$$

$$T^+ = \frac{2\mathrm{e}^{\mathrm{i}kL}(T_{11}T_{22} - T_{12}T_{21})}{T_{11} + T_{12}/Z_0 + Z_0 T_{21} + T_{22}}, \tag{2.47}$$

$$\alpha^+ = 1 - |R^+|^2 - |T^+|^2. \tag{2.48}$$

Here, Z_0 is the characteristic impedance of the surrounding medium. Furthermore, if a system is isotropic and homogeneous, then the layer is reciprocal [43]. As such, the determinant of the transfer matrix is equal to unity. i.e.:

$$T_{11}T_{22} - T_{21}T_{12} = 1. \tag{2.49}$$

Additionally, if the system is symmetric, i.e. the reflection coefficient is independent of the direction of wave propagation, then the following condition holds true:

$$T_{11} = T_{22}. \tag{2.50}$$

From these conditions, it is evident that if the system becomes isotropic and symmetric, then equations (2.44)-(2.46) reduce to $T^+ = T^-$ and $R^+ = R^-$. i.e. The acoustic transmission and reflective properties of the system are independent on the direction of incidence. This leads to the following transmission and reflection coefficients:

$$T = \frac{2\mathrm{e}^{-\mathrm{i}kL}}{T_{11} + T_{12}/Z_0 + Z_0 T_{21} + T_{22}}, \tag{2.51}$$

$$R = \frac{T_{11} + T_{12}/Z - Z_0 T_{21} - T_{22}}{T_{11} + T_{12}/Z_0 + Z_0 T_{21} + T_{22}}. \tag{2.52}$$

2.6.4 Effective Fluid Properties of a Symmetric System

Consider the transfer matrix that is the result of a series of matrix multiplications to model a symmetric system. The result is a 2x2 matrix which can be thought of as a single effective fluid layer of finite length, L. From this, the four transfer matrix elements can be directly related to the effective fluid properties [69]. Specifically, the effective wavenumber can be found as

$$k_{eff}(\omega) = \frac{1}{L}\,\mathrm{arcsin}\left(\sqrt{-T_{12}T_{21}}\right), \tag{2.53}$$

and the characteristic impedance as

$$Z_{eff}(\omega) = \sqrt{\frac{T_{12}}{T_{21}}}. \tag{2.54}$$

From these two equations, the effective speed of sound is then

$$c_{eff}(\omega) = \omega / k_{eff}(\omega), \tag{2.55}$$

the effective dynamic density is

$$\rho_{eff}(\omega) = \frac{Z_{eff}(\omega) S_{eff}}{c(\omega)}, \tag{2.56}$$

and the effective complex compressibility is

$$C_{eff}(\omega) = (c(\omega)^2 \rho_{eff}(\omega))^{-1}, \tag{2.57}$$

where S_{eff} is the cross sectional area of the effective fluid layer. This method of retrieving the effective fluid properties is coined the 'TMM Multiplication' method within this thesis.

2.6.5 Modelling Helmholtz Resonators

To calculate the impedance of a single Helmholtz resonator, the transfer matrix method is used. The full matrix, T, is derived from the following expression [70]:

$$T = M_n M_{\Delta l} M_c. \tag{2.58}$$

The transfer matrix for the HR neck and cavity take the following forms, respectively.

$$M_n = \begin{bmatrix} cos(k_n L_n) & iZ_n sin(k_n L_n) \\ \frac{i}{Z_n} sin(k_n L_n) & cos(k_n L_n) \end{bmatrix}, \tag{2.59}$$

$$M_c = \begin{bmatrix} cos(k_c L_c) & iZ_c sin(k_c L_c) \\ \frac{i}{Z_c} sin(k_c L_c) & cos(k_c L_c) \end{bmatrix}. \tag{2.60}$$

The transfer matrix that accounts for the end corrections of the HR neck is written as:

$$M_{\Delta l} = \begin{bmatrix} 1 & \mathrm{i} \rho_0 \omega \Delta l / S_n \\ 0 & 1 \end{bmatrix}. \tag{2.61}$$

Where Δl is arrived at from the addition of two correction lengths, $\Delta l = \Delta l_1 + \Delta l_2$. Δl_1 is due to pressure radiation at the discontinuity from the neck to the cavity of the HR [71] and Δl_2 comes from the pressure radiation at the discontinuity from the neck to the surrounding medium [72].

$$\Delta l_1 = 0.82\left[1 - 1.35\frac{r_n}{r_c} + 0.31\left(\frac{r_n}{r_c}\right)^3\right] r_n. \tag{2.62}$$

$$\Delta l_2 = 0.82\Big[1 - 0.235\frac{r_n}{r_w} - 1.32\Big(\frac{r_n}{r_w}\Big)^2 + 1.54\Big(\frac{r_n}{r_w}\Big)^3 - 0.86\Big(\frac{r_n}{r_w}\Big)^4\Big] r_n, \tag{2.63}$$

or

$$\Delta l_2 = 0.6 r_n. \tag{2.64}$$

The first expression of Δl_2 is accurate for a waveguide side-loaded with a HR, whilst the second expression is accurate for a waveguide with a HR placed at a dead-end.

To determine the surface impedance for a resonator placed at the end of a waveguide, you multiply the final T matrix by $[1, 0]^T$, this accounts for the velocity termination. From this, the impedance can simply be found as follows:

$$Z_{HR} = \frac{P_{x=0}}{v_{x=o}} = \frac{T_{11}}{T_{21}}. \tag{2.65}$$

This yields the expression:

$$Z_{HR} = -i\frac{cos(k_n l_n)cos(k_c l_c) - Z_n k_n \Delta l cos(k_n l_n)sin(k_c l_c)/Z_c - Z_n sin(k_n l_n)sin(k_c l_c)/Z_c}{sin(k_n l_n)cos(k_c l_c)/Z_n - k_n \Delta l sin(k_n l_n)sin(k_c l_c)/Z_c + cos(k_n l_n)sin(k_c l_c)/Z_c}. \tag{2.66}$$

The transfer matrix for a Helmholtz resonator with a porous inclusion within the cavity is expressed as

$$T = M_n M_{\Delta l} M_c M_p, \tag{2.67}$$

where M_p is the transfer matrix for an effective fluid layer of porous material defined using equations (2.19) and (2.20). The impedance can be obtained using the same methodology for a Helmholtz resonator with no porous inclusion.

2.7 Numerical Methods

All numerical modelling presented in this Thesis was undertaken using COMSOL Multiphysics, which is a commercially available Finite Element Method (FEM) software package which can be used to solve the acoustic wave propagation through fluids with complex geometry using a number of acoustic equations and boundary conditions to accurately model systems.

The finite element method is an analytical technique for solving partial differential equations over a 2D or 3D domain. To determine a solution to a particular problem, the geometry of a system is discretised into a finite number of smaller sub-divisions called elements. Each element is interconnected at singular points, which are called nodes. The collection of elements and nodes for a given system is called the mesh. The solution to the governing equations is solved at each node of an element. From the solution at each node, a global solution can be determined based upon the nodal contributions of each element, with a continuous solution interpolated using these contributions [73].

All modelling herein was undertaken using the frequency domain within the pressure acoustics module of COMSOL multiphysics. Therefore, the governing equation of motion is the Helmholtz equation. This is a time independent form of the wave equation for a harmonic pressure wave excitation, $p = p_0$e^{iwt}:

$$\nabla(-\frac{1}{\rho_c}\nabla p_0) - \frac{k_{eq}^2 p_0}{\rho_c} = 0, \tag{2.68}$$

where the equivalent wavenumber $k_{eq} = \omega/c_c$, in which the complex speed of sound is c_c and the complex dynamic density is ρ_c.

Acoustically rigid surfaces are modelled as sound-hard boundaries using the Neumann boundary condition. Through this, the normal component of the fluid acceleration is zero at the boundaries. The expression for this is

$$\vec{n}(-\frac{1}{\rho_0}\nabla p_0) = 0, \tag{2.69}$$

where $\vec{n}$ is the normal vector at the boundaries. Viscothermal losses are modelled using the narrow-regions acoustic domain selection within COMSOL. This solves the Helmholtz equation within the narrow regions with the following corrections for the complex speed of sound and complex dynamic density [74]:

$$c_c = c\sqrt{\frac{\Psi_v}{\gamma - (\gamma - 1)\Psi_h}}, \tag{2.70}$$

$$\rho_c = \frac{\rho_0}{\Psi_V}. \tag{2.71}$$

Here Ψ_v and Ψ_h are viscous and thermal field functions, respectively. The viscous wavenumber, $k_v^2 = -i\omega\rho_0/\mu$, and the thermal wavenumber, $k_h^2 = -i\omega\rho_0 C_p/\kappa$, are inputted into the viscous and thermal field functions. κ is the thermal conductivity, μ is the kinematic viscosity and C_p is the specific heat capacity at constant pressure. Depending on the geometry of the modelled system, i.e. if it is a circular or rectangular duct, the viscous and thermal field functions are tailored to accurately account for the viscous and thermal effects, as in Section 2.4.1.

The poro-acoustic losses are computed in a smaller manor such that the complex speed of sound is $c_c = \sqrt{K_e/\rho_e}$ and the complex dynamic density is $\rho_c = \rho_r$. Here the complex effective bulk modulus, K_e and density ρ_e are computed using the JCA expressions displayed in Section 2.4.2.

In order to eliminate unwanted acoustic reflections, perfectly matched layers (PML) have been used. These act as artificial porous media that are extremely effective at absorbing acoustic waves and as such can be used to emulate anechoic terminations [75]. By placing a PML at the end of an numerically modelled acoustic waveguide, it allows for the retrieval of the acoustic properties of the system by eliminating any unwanted reflections which would affect pressure results.

2.7.1 Mesh Convergence

The size of each element within a mesh is often a crucial factor upon the accuracy of FEM computations. For the modelling of acoustic systems, it is recommended to have the maximum of an element size at least five times smaller than the smallest acoustic wavelength modelled [76]. The mesh density should also be suitable such that any small geometrical properties of the modelled systems are accurately approximated by the mesh.

For example, a mesh convergence study has been undertaken on a single cylindrical Helmholtz resonator side-loading a square waveguide. This was conducted for the frequency range $[10, 1500]$ Hz. The geometry of the system is presented in Table 2.3.

r_n	l_n	r_c	l_c	A_w
3.5	5	25	40	50

Table 2.3: Geometric properties of waveguide side-loaded by a Helmholtz resonator for the mesh convergence study. All units are [mm].

Due to the geometry presented here being representative of the geometry presented throughout this Thesis, it was deemed appropriate to conduct a mesh convergence analysis of this geometry. Because of the narrow region with the neck and cavity of the Helmholtz resonator, the mesh was sufficiently dense within this region such that all geometrical details were captured. Therefore, the mesh convergence analysis was undertaken on the main waveguide on which the Helmholtz resonator was side-loading. This was done by parametrically varying the maximum mesh size through the ranges λ, $\lambda/5$, $\lambda/10$, and $\lambda/20$ at 1500 Hz and comparing plots of the transmission, reflection and absorption coefficients to assess convergence. In all instances the minimum mesh size was $\lambda/20$ within the main waveguide. These results were plotted against those obtained with the TMM to determine the agreement with the analytical methodology. Plots comparing the obtained transmission, relfection and absorption coefficients from varying waveguide maximum mesh element sizes can be seen in Figure 2.9.

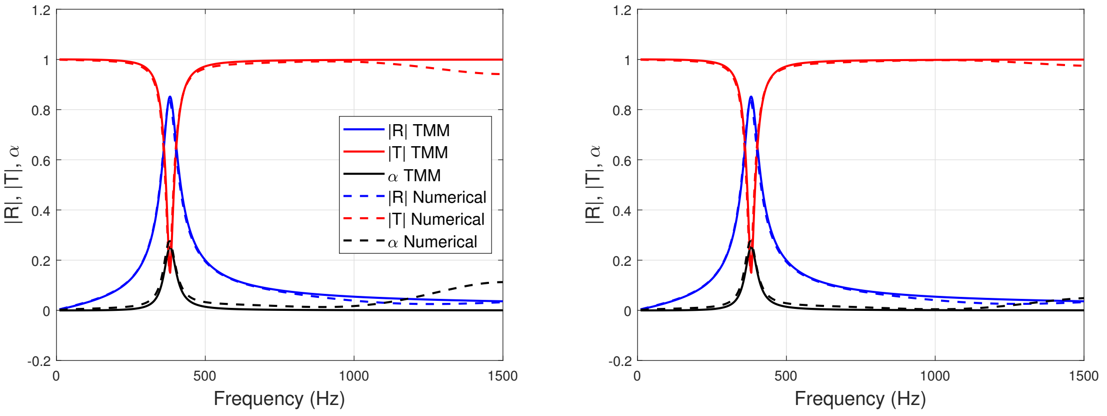

(a) λ (b) $\lambda/5$

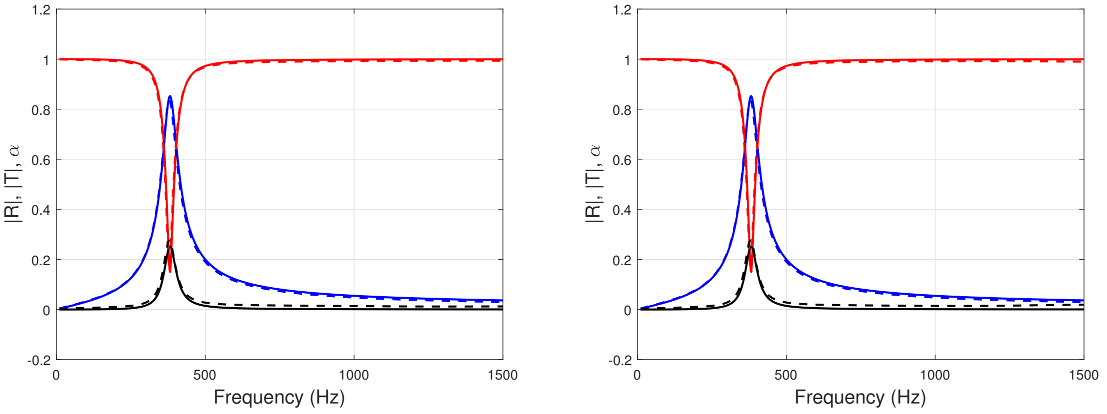

(c) $\lambda/10$ (d) $\lambda/20$

Figure 2.9: The transmission ($|T|$), reflection ($|R|$) and absorption (α) coefficients computed using the TMM method (TMM) and numerically (Numerical) for a waveguide side-loaded by a single Helmholtz resonator for four values of maximum element size λ, $\lambda/5$, $\lambda/10$, and $\lambda/20$ at 1500 Hz.

From this figure it can be seen that excellent agreement between all the mesh sizes in comparison to the TMM when modelling the response of the Helmholtz resonator. This is due to the high mesh density required to accurately approximate the resonator geometry and the fact that the resonator response is within the low frequency range, where there are more elements per wavelength. However, above 1000 Hz it can be seen that there is some inaccuracies within the results for the maximum mesh sizes of λ and $\lambda/5$, when in comparison to the TMM and the two finer meshes. Therefore, for all modelling herein it can be determined that it is necessary to have at least 10 elements per wavelength and to ensure the mesh is fine enough to accurately approximate the modelled geometry.

2.7.2 Two Microphone Method

The methodology to establish the acoustic properties of the one port numerical models is the based upon the two-microphone method, as described in [77, 78]. This is an experimental methodology which allows for the retrieval of the acoustic reflection coefficient of one port systems placed at the end of an impedance tube. This experimental methodology can be adapted to obtain the acoustic properties of one port systems modelled numerically. By modelling an ideal plane wave source at one endpoint of a waveguide and the sample with rigid backing at the other, it is possible to determine the reflection coefficient by extracting the complex valued total acoustic pressure at the two pressure points positioned at x_1 and x_2, as highlighted in Figure 2.10.

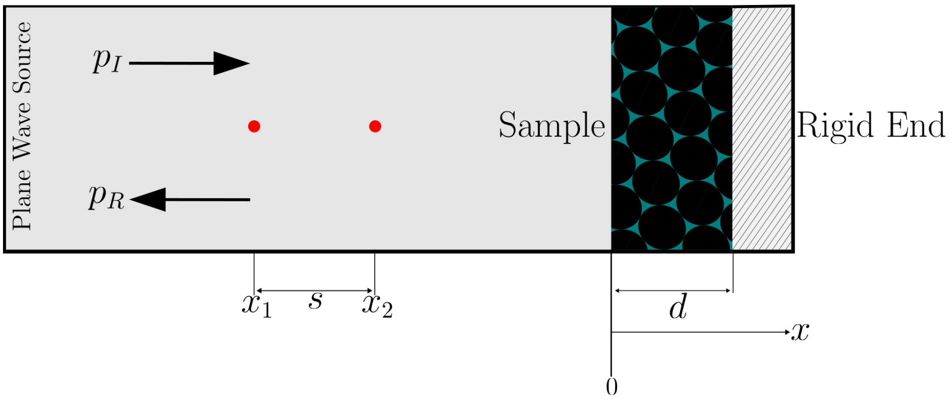

Figure 2.10: Schematic drawing of a numerical model utilising the two-microphone method to determine the reflection coefficient. The red points represent the pressure points at which the total acoustic pressure is retrieved.

The complex valued total acoustic pressure at the points x_1 and x_2, respectively, are expressed as

$$\begin{aligned} p_1 &= p_I(x_1) + p_R(x_1) = \hat{p_I}\mathrm{e}^{-i\mathrm{i}kx_1} + \hat{p_R}\mathrm{e}^{i\mathrm{i}kx_1}, \\ p_2 &= p_I(x_2) + p_R(x_2) = \hat{p_I}\mathrm{e}^{i\mathrm{i}kx_2} + \hat{p_R}\mathrm{e}^{-i\mathrm{i}kx_2}, \end{aligned} \tag{2.72}$$

where $\hat{p_I}$ and $\hat{p_R}$ are the amplitudes of the incident and reflected waves, respectively. The transfer functions for the incident and reflected waves can therefore be expressed as

$$\begin{aligned} H_I &= \frac{p_I(x_2)}{p_I(x_1)} = \frac{\hat{p_I}\mathrm{e}^{-\mathrm{i}kx_2}}{\hat{p_I}\mathrm{e}^{-\mathrm{i}kx_1}} = \mathrm{e}^{iks}, \\ H_R &= \frac{p_R(x_2)}{p_R(x_1)} = \frac{\hat{p_R}\mathrm{e}^{\mathrm{i}kx_2}}{\hat{p_R}\mathrm{e}^{\mathrm{i}kx_1}} = \mathrm{e}^{-iks}, \end{aligned} \tag{2.73}$$

where $s = x_2 - x_1$ is the separation distance of the points. The transfer function between the two pressure point positions can be expressed as

$$H_{12} = \frac{p_2}{p_1} = \frac{\hat{p_I}\mathrm{e}^{-\mathrm{i}kx_2} + \hat{p_R}\mathrm{e}^{\mathrm{i}kx_2}}{\hat{p_I}\mathrm{e}^{-\mathrm{i}kx_1} + \hat{p_R}\mathrm{e}^{\mathrm{i}kx_1}}. \tag{2.74}$$

Finally, using these expressions, the reflection coefficient at the sample surface, $x = 0$, can be obtained as

$$R = \frac{H_{12} - H_I}{H_R - H_{12}}\mathrm{e}^{\mathrm{i}k2x_1}. \tag{2.75}$$

From this the acoustic surface impedance and absorption coefficient can also be obtained.

2.7.3 Four Microphone Method

The methodology to establish the acoustic properties of the two port numerical models is the based upon the four-microphone method, as described in [79, 80]. This is an experimental method which allows for a transfer matrix to be constructed for a system, meaning the acoustic properties of a two port system can be obtained. A key assumption is the test sample does not exhibit symmetric absorption, i.e. $T_{11} \neq T_{22}$.

In the experimental setup a loudspeaker is installed at one endpoint of the impedance tube and generates a wide-band white noise signal. The test sample is placed in the centre of the impedance tube with a pair of microphones placed either side. The endpoint opposite the loudspeaker can be equipped with either an anechoic or reflecting termination, allowing for two tests with different boundary conditions. This is an essential factor in determining the asymmetrical absorptive properties of systems.

This experimental methodology can be adapted to obtain the acoustic properties of two port systems modelled numerically. By modelling an ideal plane wave source at one endpoint and either a sound-hard boundary or a PML at the other endpoint, it is possible to simulate the same setup. By retrieving the total acoustic pressure at four points, two either side of the modelled system, the following calculations can be used to determine the acoustic properties from the numerical model. A graphical example of this setup is displayed in Figure 2.11.

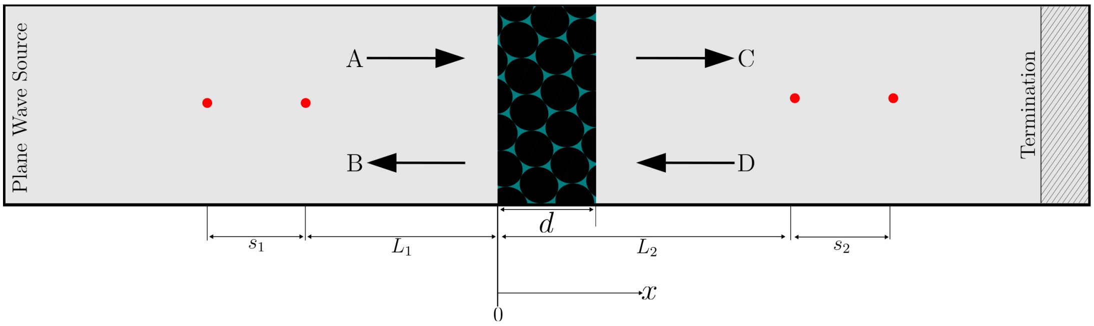

Figure 2.11: Schematic drawing of a numerical model utilising for the four-microphone method to retrieve the asymmetric reflection coefficient. The red points represent the pressure points at which the total acoustic pressure is retrieved.

Here the acoustic wavenumber is simply defined as the real value $k = 2\pi f/c$, and the four amplitude coefficients A, B, C and D can be calculated once the complex acoustic transfer functions, $H_{i,ref}$, between the ith pressure point and reference pressure point are obtained:

$$\begin{aligned}
A &= \frac{\mathrm{i}\big(H_{1,ref}\mathrm{e}^{-\mathrm{i}kL_1} - H_{2,ref}\mathrm{e}^{-\mathrm{i}k(L_1+s_1)}\big)}{2\sin(ks_1)},\\
B &= \frac{\mathrm{i}\big(H_{2,ref}\mathrm{e}^{\mathrm{i}k(L_1+s_1)} - H_{1,ref}\mathrm{e}^{\mathrm{i}kL_1}\big)}{2\sin(ks_1)},\\
C &= \frac{\mathrm{i}\big(H_{3,ref}\mathrm{e}^{\mathrm{i}k(L_2+s_2)} - H_{4,ref}\mathrm{e}^{\mathrm{i}kL_2}\big)}{2\sin(ks_2)},\\
D &= \frac{\mathrm{i}\big(H_{4,ref}\mathrm{e}^{-\mathrm{i}kL_2} - H_{3,ref}\mathrm{e}^{-\mathrm{i}k(L_2+s_2)}\big)}{2\sin(ks_2)},
\end{aligned} \tag{2.76}$$

where any of the four pressure point locations can be used as the reference. For either boundary condition, it is possible to determine the acoustic pressure and particle velocity for $x = 0$ and $x = d$. These are determined as:

$$\begin{aligned}
p_0 &= A + B,\\
v_0 &= \frac{(A - B)}{\rho c}\\
p_d &= C\mathrm{e}^{-\mathrm{i}kd} + D\mathrm{e}^{\mathrm{i}kd}\\
v_d &= \frac{(C\mathrm{e}^{-\mathrm{i}kd} - D\mathrm{e}^{\mathrm{i}kd})}{\rho c}.
\end{aligned} \tag{2.77}$$

The total transfer matrix, T, for the system can be determined from the calculated acoustic pressures and particle velocities for the two boundary conditions; where

a is the anechoic termination and b is the sound-hard backing:

$$T = \begin{bmatrix} T_{11} & T_{12} \\ T_{21} & T_{22} \end{bmatrix} = \\ \begin{bmatrix} (p_{0a}v_{db} - p_{0b}v_{da})/(p_{da}v_{db} - p_{db}v_{da}) & (p_{0b}v_{0a} - p_{0a}v_{db})/(p_{da}v_{db} - p_{db}v_{da}) \\ (p_{0a}v_{db} - p_{0b}v_{da})/(p_{da}v_{db} - p_{db}v_{da}) & (p_{da}v_{0b} - p_{db}v_{0a})/(p_{da}v_{db} - p_{db}v_{da}) \end{bmatrix} . \tag{2.78}$$

From this it is now possible to establish the acoustic properties of the system using the methodology set it in Section 2.6.3.

Chapter 3

The use of the Transfer Matrix Method to predict the effective fluid properties of acoustical systems

The transfer matrix method (TMM) is a simple and powerful method to model acoustical systems. Using this method it is possible to analyse the sound absorption/transmission properties of one and two port systems [56], assess effects due to periodicity [34, 40] and derive effective property expressions for porous layers [69]. Additionally, it has proven to be a popular technique in order to model multilayered porous materials [3], parallel assemblies of porous materials [81] and sound absorbing acoustic metamaterials consisting of waveguide structures side-loaded by Helmholtz resonators [13, 45].

In the acoustics of porous materials, sound propagation in rigid tortuous pores is modelled with the linear superposition of the macroscopic pressure gradient and the averaged velocity within pore segments of constant cross-section. This approach of discretising pores into segments was used in the Champoux and Stinson model [55] to determine the effective density and compressibility and thus enables the building of simple acoustical models.

In this chapter, a general methodology is proposed to obtain simple analytical expressions for the effective material properties for symmetric systems that can be modelled with the TMM, denoted as 'TMM Summation'. The proposed method utilises the linear superposition of terms derived from the transfer matrix components of a system to obtain the total effective properties of the system. This method differs from the traditional transfer matrix method as it is not reliant upon the matrix multiplication of each segment's transfer matrices. As such, simple analytical expressions for complex systems can be derived using this method, allowing for an insight into the underlying physics of these systems.

The proposed methodology is validated for two scenarios. Firstly, the effective properties are obtained for a single rigid tortuous pore consisting of cylindrical sections of varying cross sectional area. The obtained effective properties are simplified to succinct analytical expressions which match the well established Champoux and Stinson model [55]. These expressions are validated against the traditional TMM. Secondly, simple general expressions for the effective dynamic density and complex compressibility are obtained for a waveguide side-loaded by an arbitrary number of Helmholtz resonators. These expressions are validated against results obtained using the traditional TMM and numerically for a symmetric system.

3.1 The TMM Summation Method

The transfer matrix method provides a system of two equations which relates the acoustic pressure, p, and the volume flux, V, at $x = 0$ and $x = -L$, where L is the length of the system. For a two-port system these are:

$$p_0 = T_{11} p_L + T_{12} V_L, \tag{3.1}$$

and

$$V_0 = T_{21} p_L + T_{22} V_L. \tag{3.2}$$

The subscripts 0 and L denote the respective variable value at $x = 0$ and $x = -L$ of the system. Consider a system discretised into M segments, each with a cross section $S_a^{(m)}$ and length $l^{(m)}$, where (m) denotes the m^{th} segment. By applying the velocity-pressure relationship $V_L = p_L / Z_L$, where Z_L is the characteristic impedance at the local coordinate $x = -l^{(m)}$ of a segment, equations (3.1) and (3.2) can be modified to model the change in pressure and particle velocity within the

m^{th} segment. These expressions are:

$$p_0^{(m)} = \left(T_{11}^{(m)} + \frac{T_{12}^{(m)}}{Z_L^{(m)}} \right) p_L^{(m)}, \tag{3.3}$$

and

$$v_0^{(m)} = \frac{1}{S_a} \left(T_{21}^{(m)} + \frac{T_{22}^{(m)}}{Z_L^{(m)}} \right) p_L^{(m)}. \tag{3.4}$$

For further clarification, Figure 3.1 shows the m^{th} segment of an arbitrary symmetric system.

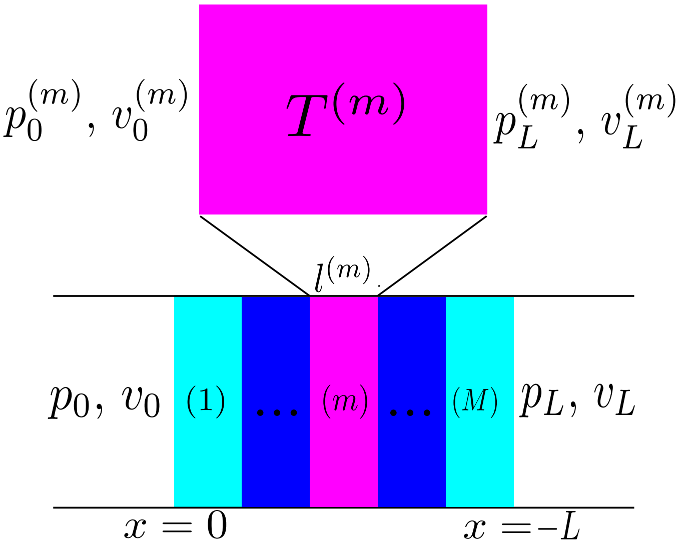

Figure 3.1: Graphical depiction of the application of the modified transfer matrix equations to the m^{th} segment of an arbitrary symmetric system.

Continuing this notion of a discretised system and utilising the equation of motion (2.1), the equation of motion for the m^{th} segment of a system can be described as:

$$-\left(\frac{\partial p}{\partial x} \right)^{(m)} = \mathrm{i}\omega\rho(\omega)^{(m)} v^{(m)}. \tag{3.5}$$

Here, the pressure gradient of the fluid within the m^{th} segment, $(\partial p / \partial x)^{(m)}$, can be expressed as $(p_L^{(m)} - p_0^{(m)})/l^{(m)}$, assuming $l^{(m)}$ is sufficiently small with respect to the wavelength. The average fluid velocity across the m^{th} segment, $v^{(m)}$, is taken to be $v_L^{(m)}$ to capture velocity variation along the segment. Assuming that the tortuosity of the m^{th} segment is equal to unity due to the constant cross section, by inputting these substitutions from equations (3.3) and (3.4) and some algebraic manipulation, the effective dynamic density of the fluid within the m^{th} segment of a system can be obtained as:

$$\rho_{eff}^{(m)}(\omega) = \frac{\left((T_{11}^{(m)} - 1)Z_L^{(m)} + T_{12}^{(m)}\right) S_a^{(m)}}{\mathrm{i}\omega l^{(m)}}. \tag{3.6}$$

To determine the effective density of the total system, the effective densities for all segments are superimposed. Each term is multiplied by the acoustic inertance weighting factor, $\left(l^{(m)}/S_a^{(m)}\right) / \sum\limits_{m=1}^{M} \left(l^{(m)}/S_a^{(m)}\right)$, to account for density terms from narrow cross sections being dominant in the total effective dynamic density. The tortuosity of the total system, α_∞, is then included as a factor on the superimposed expression. This is defined as [82]:

$$\alpha_\infty = \frac{\sum\limits_{m=1}^{M} S_a^{(m)} l^{(m)}}{\left(\sum\limits_{m=1}^{M} l^{(m)}\right)^2} \sum_{m=1}^{M} \frac{l^{(m)}}{S_a^{(m)}}. \tag{3.7}$$

Therefore, the total effective density of the fluid within the symmetric system is calculated using the following expression:

$$\rho_{eff}(\omega) = \frac{\alpha_\infty \sum\limits_{m=1}^{M} \rho_{eff}^{(m)}(\omega) l^{(m)}/S_a^{(m)}}{\sum\limits_{m=1}^{M} l^{(m)}/S_a^{(m)}} = \frac{\alpha_\infty \sum\limits_{m=1}^{M} \left((T_{11}^{(m)} - 1)Z_L^{(m)} + T_{12}^{(m)}\right)}{\mathrm{i}\omega \sum\limits_{m=1}^{M} l^{(m)}/S_a^{(m)}}. \tag{3.8}$$

Using the same logic and applying this to equation (2.4), the rate of change in the acoustic velocity for the fluid in the m^{th} segment can be described as:

$$-\left(\frac{\partial v}{\partial x}\right)^{(m)} = \mathrm{i}\omega C(\omega)^{(m)} p^{(m)}. \tag{3.9}$$

Here, the velocity gradient of the fluid within the m^{th} segment $(\partial v/\partial x)^{(m)}$ can be expressed as $(v_L^{(m)} - v_0^{(m)})/l^{(m)}$, where $v_L^{(m)} = p_L^{(m)}/(Z_L^{(m)} S_a)$, assuming $l^{(m)}$ is sufficiently small with respect to the wavelength. The acoustic pressure $p^{(m)}$ is taken to be $p_L^{(m)}$ to capture pressure variation along the segment. Again, by inputting these substitutions from equations (3.3) and (3.4), the following expression can then be obtained for the effective complex compressibility of the fluid in the m^{th} segment of a system:

$$C_{eff}^{(m)}(\omega) = \frac{T_{21}^{(m)} Z_L^{(m)} + T_{22}^{(m)} - 1}{\mathrm{i}\omega l^{(m)} Z_L^{(m)} S_a^{(m)}}. \tag{3.10}$$

By multiplying the effective complex compressibility of the fluid within each segment by the volumetric weighting factor, $S_a^{(m)}l^{(m)}/\sum_{m=1}^{M} S_a^{(m)}l^{(m)}$, to account for compressibility terms from large cross sections being dominant in the total effective complex compressibility, and superimposing all terms, the total effective complex compressibility of the fluid within the system system can be expressed as:

$$C_{eff}(\omega) = \frac{\sum_{m=1}^{M} C_{eff}^{(m)}(\omega) S_a^{(m)} l^{(m)}}{\sum_{m=1}^{M} S_a^{(m)} l^{(m)}} = \frac{\sum_{m=1}^{M} \left(T_{21}^{(m)} Z_L^{(m)} + T_{22}^{(m)} - 1\right)\left(Z_L^{(m)}\right)^{-1}}{\mathrm{i}\omega \sum_{m=1}^{M} S_a^{(m)} l^{(m)}}. \tag{3.11}$$

A simple approach is now available to obtain analytical expressions for systems modelled by the TMM. The above expressions can be used to assess how the complex compressibility, dynamic density, speed of sound, effective wavenumber and characteristic impedance varies within a complex system.

3.2 Effective material properties of a rigid frame porous material

A simple theoretical model that describes the sound propagation through pores of known cross-sectional area and shape is proposed by Champoux and Stinson in [55]. This same rigid pore system is modelled using the proposed TMM Summation method and results are compared with those from the TMM multiplication method.

3.2.1 Application of the TMM summation method

Consider a single pore composed of M distinct cylindrical segments which are constant in cross section. Each segment, m, has a length $l^{(m)}$ and a radius $r^{(m)}$. For convenience a graphical depiction of this system can be seen in Figure 3.2.

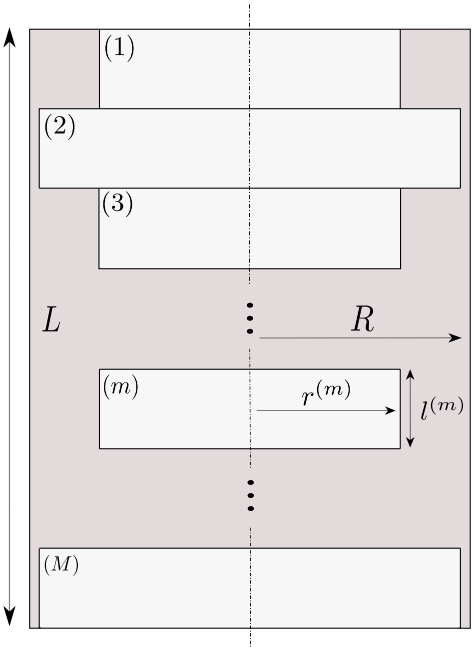

Figure 3.2: Schematic of a sample containing a single tortuous pore.

The total transfer matrix of the system, T, is:

$$T = M_\Omega \cdot M^{(1)} \cdot M^{(2)} \ldots M^{(M-1)} \cdot M^{(M)} \cdot M_\Omega^{-1}, \tag{3.12}$$

where $M^{(m)}$ is the transfer matrix for the m^{th} segment fluid layer. Here, the acoustic wavenumber, $k^{(m)}$, and characteristic impedance, $Z^{(m)}$, are obtained with equations (2.15) and (2.16) to account for the viscothermal losses of each segment. M_Ω accounts for the porosity of the system and is defined as:

$$M_\Omega = \begin{bmatrix} 1 & 0 \\ 0 & \frac{1}{\Omega} \end{bmatrix}. \tag{3.13}$$

From this total matrix, the effective fluid properties can be obtained by with the TMM multiplication method using equations (2.53) and (2.54).

For the TMM summation method, the effective density and compressibility of the system can be obtained by utilising equations (3.8) and (3.11) upon each matrix in the system. This results in the following expressions:

$$\rho_{eff}(\omega) = \frac{\alpha_\infty \sum_{m=1}^{M} \left(\cos\left(k^{(m)} l^{(m)}\right) + \mathrm{i}\sin\left(k^{(m)} l^{(m)}\right) - 1\right) Z^{(m)}}{\mathrm{i}\omega \sum_{m=1}^{M} \left(l^{(m)} / S_a^{(m)}\right)} \tag{3.14}$$

and

$$C_{eff}(\omega) = \frac{\sum\limits_{m=1}^{M} \left(\cos\left(k^{(m)}l^{(m)}\right) + \mathrm{i}\sin\left(k^{(m)}l^{(m)}\right) - 1\right)\left(Z^{(m)}\right)^{-1}}{\mathrm{i}\omega \sum\limits_{m=1}^{M} \left(S_a^{(m)}l^{(m)}\right)}. \tag{3.15}$$

By taking the low frequency limit, $k^{(m)}l^{(m)} \ll 1$, the series expansion of the common expression present in equations (3.14) and (3.15) can be calculated. The result of this is:

$$\cos\left(k^{(m)}l^{(m)}\right) + \mathrm{i}\sin\left(k^{(m)}l^{(m)}\right) - 1 = \mathrm{i}k^{(m)}l^{(m)} + \mathcal{O}\left\{\left(k^{(m)}l^{(m)}\right)^2\right\}. \tag{3.16}$$

Therefore, utilising the leading order term from the series expansion, the total dynamic density and complex compressibility of the fluid within the tortuous pore can be defined as:

$$\rho_{eff}(\omega) = \alpha_\infty \frac{\sum\limits_{m=1}^{M} \rho(\omega)^{(m)} l^{(m)} / S_a^{(m)}}{\sum\limits_{m=1}^{M} l^{(m)} / S_a^{(m)}} \tag{3.17}$$

and

$$C_{eff}(\omega) = \frac{\sum\limits_{m=1}^{M} C(\omega)^{(m)} S_a^{(m)} l^{(m)}}{\sum\limits_{m=1}^{M} S_a^{(m)} l^{(m)}}, \tag{3.18}$$

where $\rho(\omega)^{(m)}$ and $C(\omega)^{(m)}$ are the dynamic density and complex compressibility of the fluid in the m^{th} segments calculated with equations (2.15) and (2.16). It can be seen that these expressions match the Champoux and Stinson model.

3.2.2 Results

In this section, a single pore of four distinct segments of varying cross section is modelled using the proposed TMM summation method and then validated against the traditional TMM multiplication method. The geometric parameters for the pore can be seen in Table 3.1.

$r^{(1)}$	$r^{(2)}$	$r^{(3)}$	$r^{(4)}$	$l^{(1)}$	$l^{(2)}$	$l^{(3)}$	$l^{(4)}$	L
2	0.75	3	1.5	1	2.5	2	1	6.5

Table 3.1: Geometric properties of rigid framed pore structure. All units are [mm].

The resulting tortuousity of the system is $\alpha_\infty = 3.26$ and the sample cross sectional area can be selected as an arbitrary value as the above methods obtain the effective properties for the fluid within the pore. The plots of the real and imaginary components of effective material properties, normalised acoustic impedance, wavenumber and speed of sound can be seen in Figure 3.3.

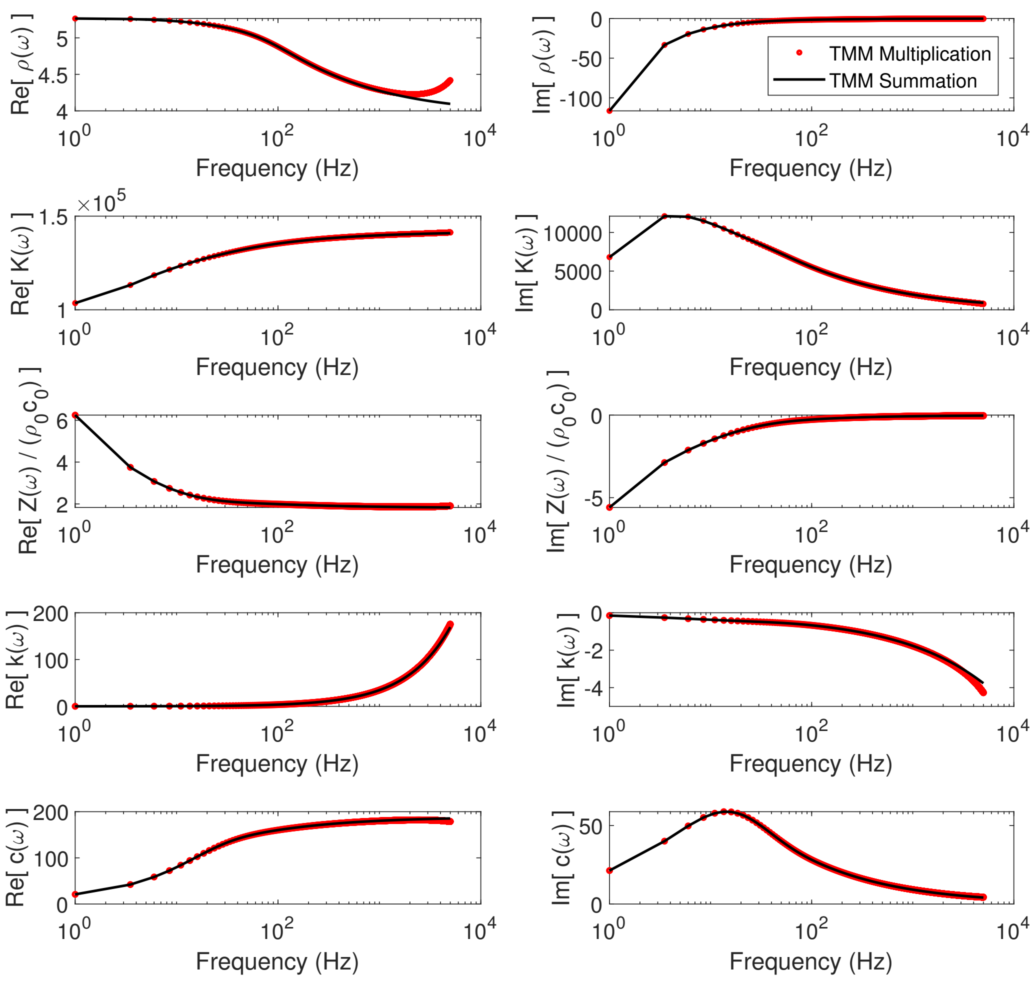

Figure 3.3: The effective density $\rho(\omega)$ [kg/m^3], bulk modulus $K(\omega)$ [Pa], normalised acoustic impedance $Z(\omega)$, wavenumber $k(\omega)$ [1/m] and speed of sound $c(\omega)$ [m/s] computed using the proposed effective property model (TMM summation) and the traditional TMM method (TMM Multiplication).

From Figure 3.3 it is evident that there is excellent agreement between the TMM summation and TMM multiplication models in the low frequency regime, with a mean absolute percentage error (MAPE) of 0.6% for the effective density and MAPE of 0.032% for the effective bulk modulus, within the first 1000Hz. Past this it can be seen that the the two methods begin to deviate from one another, as evidenced in the dynamic density and wavenumber of this system. As equations (3.17) and (3.18) are experimentally validated by Champoux and Stinson [55], with a similar pore geometry for up to 5kHz, it is thought this deviation is associated with a limitation in the retrieval of the effective properties using the TMM multiplication method. As this sysytem is not locally resonant, there is no dependance on the system being symmetrical for the effective property models to be valid. Finally, if one wanted to increase the scale of the system by an order of magnitude whilst retaining the same tortuousity, radiation effects would then have to be accounted for [83], which is not viable with this TMM Summation method.

3.3 Effective material properties of a waveguide side-loaded by Helmholtz resonators

In this section, the effective fluid properties are obtained for a waveguide side-loaded by M Helmholtz resonators. This is done using the TMM summation method. The obtained effective fluid properties are compared with those obtained using the TMM multiplication method presented in Section 2.6.4.

3.3.1 Application of the TMM summation method

Consider a waveguide section of constant cross-section, S_a, and length, L, side-loaded by M Helmholtz resonators periodically spaced by $l = L/(M-1)$, as shown in Figure 3.4. It is worth noting that the Helmholtz resonator geometries must be selected such that the system is symmetric about $x = -L/2$.

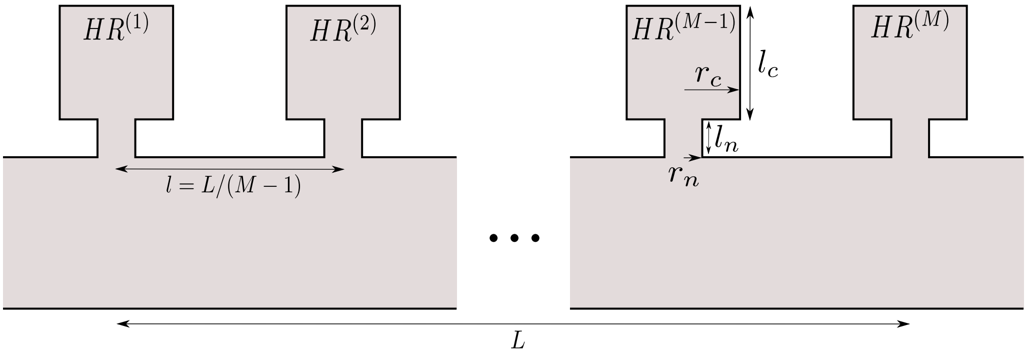

Figure 3.4: Schematic for a system of M equispaced cylindrical HRs side-loading a square waveguide.

The transfer matrix for the whole system is expressed as:

$$T = M_{HR}^{(1)} \cdot M_{WG} \cdot M_{HR2}^{(2)} \ldots M_{WG} \cdot M_{HR}^{(M-1)} \cdot M_{WG} \cdot M_{HR}^{(M)}, \tag{3.19}$$

where the waveguide transfer matrix, M_{WG}, is the transfer matrix of a fluid layer of length l. Within this matrix, $Z = \rho c/S_a$, is the characteristic impedance for plane wave propagation within the fluid of the waveguide, and k is the wavenumber of the fluid within the waveguide. These quantites are determined with the use of equations (2.17) and (2.18). The resonators are introduced as point scatterers within the transfer matrix, which is facilitated for the m^{th} resonator by the following matrix:

$$M_{HR}^{(m)} = \begin{bmatrix} 1 & 0 \\ \frac{1}{Z_{HR}^{(m)}} & 1 \end{bmatrix}. \tag{3.20}$$

To calculate the effective material properties using the traditional method of matrix multiplication, it is a simple manner of utilising the equations set out in Section 2.6.4 upon the final transfer matrix, T, of the system.

Through the application of equation (3.8) upon the transfer matrices in equation (3.19), the total effective dynamic density of the fluid within the system can be explicitly written as:

$$\rho_{eff}(\omega) = \frac{ZS_a}{\mathrm{i}\omega L} \sum_{m=1}^{M-1} \left(\cos(kl) + \mathrm{i}\sin(kl) - 1\right). \tag{3.21}$$

Through the application of equation (3.11) upon the transfer matrices in equation (3.19), the total effective compressibility of the fluid within the system can be explicitly expressed as:

$$C_{eff}(\omega) = \frac{1}{\mathrm{i}\omega L S_a}\left\{\frac{1}{Z}\sum_{m=1}^{M-1}\left(\cos\left(kl\right)+\mathrm{i}\sin\left(kl\right)-1\right)+\sum_{m=1}^{M}\frac{1}{Z_{HR}^{(m)}}\right\}. \tag{3.22}$$

By taking the low frequency limit, $kl \ll 1$, the total dynamic density and complex compressibility of the fluid within the system can be defined as:

$$\rho_{eff}(\omega) = \rho(\omega), \tag{3.23}$$

$$C_{eff}(\omega) = C(\omega) + \frac{1}{\mathrm{i}\omega L S_a}\sum_{m=1}^{M}\frac{1}{Z_{HR}^{(m)}}, \tag{3.24}$$

where $\rho(\omega)$ and $C(\omega)$ are the dynamic density and complex compressibility of the waveguide.

3.3.2 Results

To assess the validity of equations (3.23) and (3.24), a system of two cylindrical Helmholtz resonators side-loading a square waveguide is modelled. This system contains two distinct resonances resulting from variation in geometry between the Helmholtz resonators. Namely, a difference in the cross sectional area of the necks. A limiting factor in using an effective fluid layer transfer matrix to compute the reflection coefficient is due to the assumption that the system is a symmetric absorber, i.e. $T_{11} = T_{22}$. When this is not the case, such as in a degenerate coupling of Helmholtz resonators [31], the use of effective properties as presented within this paper is unfit for purpose in obtaining the reflection and absorption coefficients. This does not apply to the transmission coefficient due to the reciprocal nature of this type of system, i.e. $T_{11}T_{22} - T_{12}T_{21} = 1$.

As such, the following symmetric examples have been selected with M identical Helmholtz resonators, where $M = 3, 5, 10$ and 20. The separation between each subsequent HR is 12 mm and therefore $L = (M-1)\times 12$ mm, the width, a, and height, b, of the waveguide are $a = b = 50$ mm. The geometry of the modelled Helmholtz resonators can be seen in Table 3.2 with these quantities graphically represented in Figure 3.4.

r_n	r_c	l_n	l_c
2	10	10	60

Table 3.2: Geometric properties of the modelled Helmholtz resonator. All units are $[mm]$.

The plots of the effective dynamic density, effective bulk modulus, normalised acoustic impedance, acoustic wavenumber and the speed of sound computed using the effective property model and the TMM multiplication method for $M = 5$ can be seen in Figure 3.5.

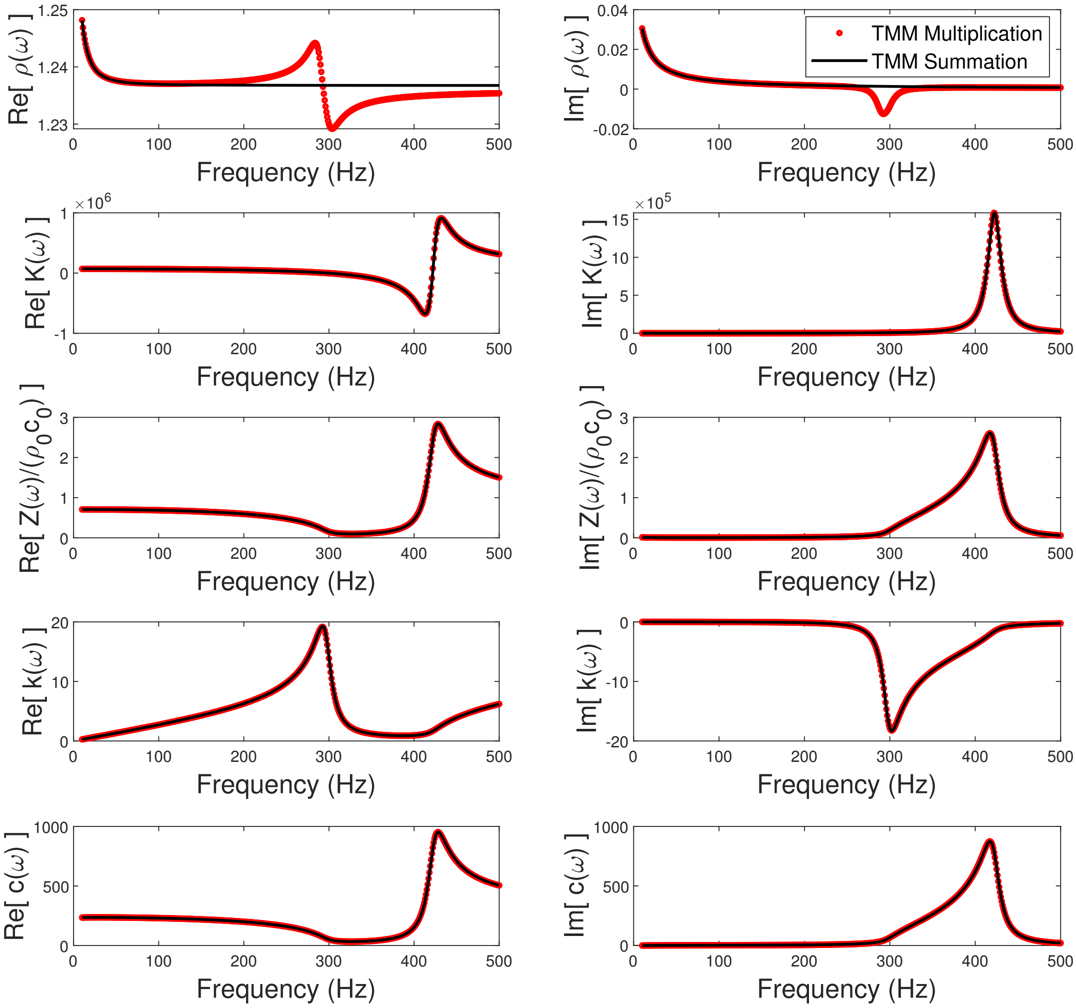

Figure 3.5: The effective dynamic density $\rho(\omega)$ $[kg/m^3]$, effective bulk modulus $K(\omega)$ $[Pa]$, normalised impedance $Z(\omega)$, acoustic wavenumber $k(\omega)$ $[1/m]$ and speed of sound $c(\omega)$ $[m/s]$ computed using the effective property model (TMM summation) and the traditional TMM method (TMM Multiplication) .

From Figure 3.5 it is evident that there is good agreement in all terms, although fluctuations within the effective density are evident in the TMM multiplication model which have not been captured with the TMM summation model. The physical nature of these fluctuations is uncertain and could either be a result of the resonances of the Helmholtz resonators or numerical errors in the retrieval of the effective wavenumber and impedance with the TMM multiplication method. Nonetheless, it can be seen that these fluctuations play no significant role in subsequent terms derived from the dynamic density and as such, regardless of the physical meaning of these fluctuations, they can be deemed negligible. Therefore, the TMM summation model can be deemed a valid approach to derive analytical approximations for symmetric systems composed of Helmholtz resonators. To corroborate this claim, it has been shown that through the use of the modal expansion method [15], an analytical approximation for the effective dynamic density of a waveguide side-loaded by Helmholtz resonators matches that of equation (3.23) obtained using the TMM summation method.

The transmission, reflection and absorption coefficients of the system for $M = 3, 5, 10$ and 20 have been computed using the TMM method, numerically and with the TMM summation method. The equations used to obtain the transmission and reflection coefficients were (2.51) and (2.52). These equations were applied to the total transfer matrix of the system for the TMM method and to the transfer matrix of an effective fluid layer for the TMM summation method. The numerical calculations were done using COMSOL 6.0 using the Acoustics Pressure Module. The model was 3D with the viscothermal losses being accounted for in every region of the structure.

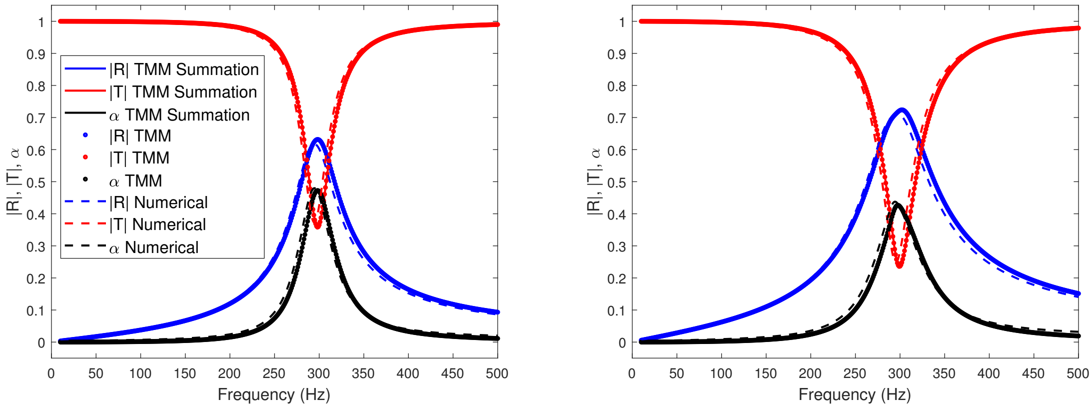

(a) M=3 (b) M=5

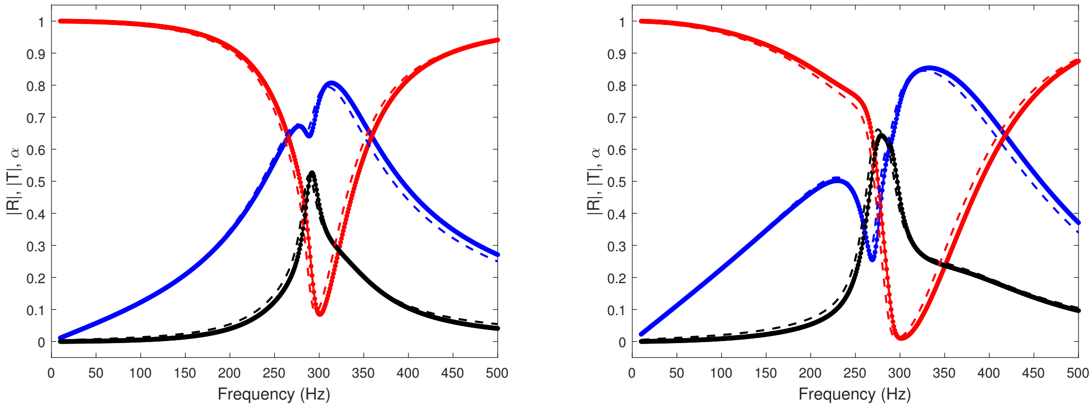

(c) M=10 (d) M=20

Figure 3.6: The transmission ($|T|$), reflection ($|R|$) and absorption (α) coefficients computed using the effective property model (TMM summation) in comparison to the coefficients obtained with the traditional TMM method (TMM) and numerically (Numerical).

From Figure 3.6 it can be seen that with increasing amounts of identical Helmholtz resonators, the system exhibits greater absorptive and reflective properties such that the transmission coefficient is minimised. For $M = 20$, this accumulation of resonances has reduced the transmission coefficient to 0 at approximately 300 Hz. Furthermore, it is evident that there is excellent agreement between the three methods when computing the transmission properties, which is due to the reciprocity of the modelled systems. Due to the symmetry of the modelled systems, it can be seen that the reflection and absorption coefficients obtained with the TMM summation method are also in excellent agreement with the TMM and numerical methods. This holds true for all modelled values of M, indicating that the TMM summation method provides valid analytical approximation to complex symmetric acoustical systems where high levels of transmission loss can be obtained, as long as $L \ll \lambda$. Therefore, the TMM Summation method can be used to provide a simple expressions for the effective fluid properties of complex symmetric systems where high levels of transmission loss can be obtained. This is beneficial when in contrast to the TMM Multiplication method as any expressions resulting from large chains of matrix multiplications are unwieldy for practical use.

The following example, as presented in [84], has been selected as to minimise asymmetry in the reflection coefficient to show that whilst not rigorous mathematically, the effective property approach can still be used to approximate weakly asymmetric systems. This is possible due to very weak coupling between the Helmholtz resonators by ensuring there is a suitable gap between the resonant frequencies of the resonators. The length of the system is $L = 34mm$, the width, a, and height, b, of the waveguide are $a = b = 50mm$. The geometry of the modelled Helmholtz resonators can be seen in Table 3.3.

HR	r_n	r_c	l_n	l_c
1	3	15	10	40
2	1.5	15	10	40

Table 3.3: Geometric properties of the modelled Helmholtz resonators. All units are $[mm]$.

The transmission, reflection and absorption coefficients of the system for the $-\mathrm{i}kx$ and $+\mathrm{i}kx$ have been computed using the TMM method and numerically. The transmission, reflection and absorption coefficients assuming a symmetric system have been computed using TMM summation method. These plots can be found in Figure 3.7.

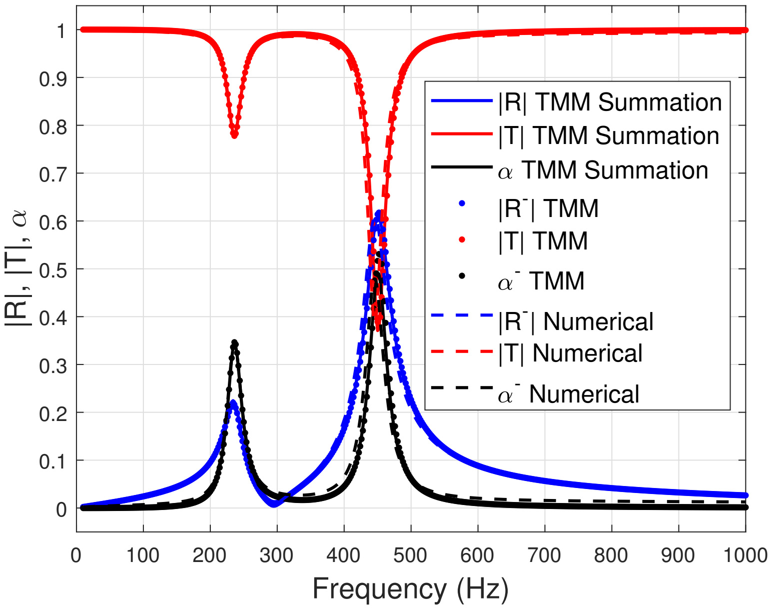

(a) $-\mathrm{i}kx$ direction

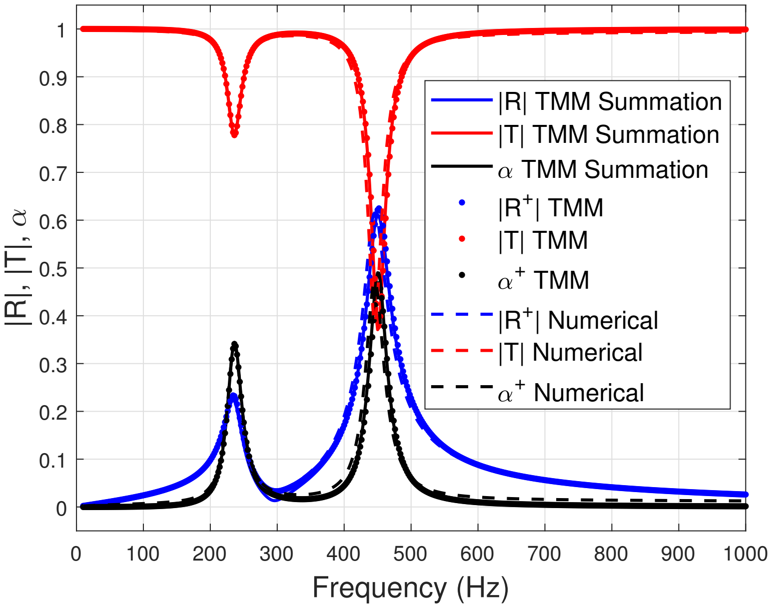

(b) $+\mathrm{i}kx$ direction

Figure 3.7: The symmetric transmission ($|T|$), reflection ($|R|$) and absorption (α) coefficients computed using the effective property model (TMM summation) in comparison to the asymmetric coefficients obtained with the traditional TMM method (TMM) and numerically (Numerical).

From Figure 3.7, it is evident that there is good agreement between the three methods when computing the transmission properties of the selected system. Due to the near-symmetry in the system, it can be seen that the reflection and absorption coefficients obtained with the TMM summation method remains consistent with the coefficients obtained using the TMM and numerical methods. From the results it can be concluded that the TMM summation method provides valid analytical approximations to the traditional TMM method, so long as the modelled system does not exhibit asymmetric reflection properties.

It must be noted that this model only remains valid in the low frequency regime, below the first Bragg frequency and the first cross sectional mode of the waveguide. This is due to the model's inability to account for effects associated with periodicity and the assumption of plane wave propagation within the formulation of the model. The failure to capture effects due to periodicity can be seen upon examination of equation (3.24) where the summation term associated with each resonator is scaled by the total length of the system, not the separation of each resonator.

To highlight the inability to capture asymmetric reflection phenomenon using the two effective property models presented here, a set of degenerate Helmholtz resonators have been modelled using the TMM, TMM summation and TMM multiplication methods. The geometry of the Helmholtz resonators can be found in Table 3.4. The waveguide dimensions and system length are unchanged.

HR	r_n	r_c	l_n	l_c
1	4	15	10	40
2	4	15	10	42

Table 3.4: Geometric properties of the modelled degenerate Helmholtz resonators. All units are [mm].

The plots of the absorption coefficient for the two directions of incidence, α^+ and α^-, obtained with the TMM method, absorption coefficients obtained using the TMM summation method and TMM multiplication method are presented in Figure 3.8.

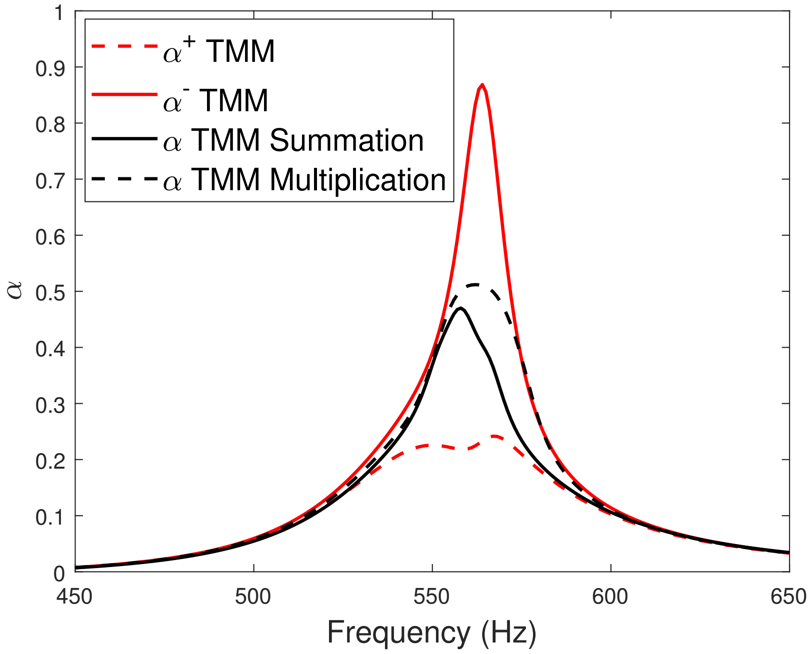

Figure 3.8: Plots of the absorption coefficient for the two directions of incidence α^+ and α^-, obtained with the TMM method, against the absorption coefficient obtained using the TMM summation and multiplication methods.

From Figure 3.8 it can be seen that when using the TMM method, the effects of strong evanescent coupling can be captured. This is evident with the large disparity between the amplitude of absorption between the two directions of incidence. Adversely, when looking at the plots produced by the two effective property methods, there is little correlation to the absorption for either direction of incidence. Additionally, there is poor agreement between the two effective property models too. As such, the two effective property models are only valid for systems of Helmholtz resonators in which there is weak evanescent coupling. If evanescent coupling were to be captured, the effective fluid properties would have to be modified for each direction of incidence.

3.4 Chapter Conclusion

A general effective property model has been proposed to obtain explicit analytical expressions for complex systems. By discretising a system into segments, it is possible to utilise the transfer matrix method to predict the acoustic properties in these segments. Through the application of linear superposition, these individual segment effective properties can be summated to achieve the total effective properties of the system. Analytical expressions were derived for two use in order to validate the model.

Firstly, the proposed approach was applied to derive the effective properties for the fluid in a singular pore consisting of M unique cylindrical cross sections. This is consistent with well established Champoux-Stinson model for rigid pored structures. These expressions were then used to describe the dynamic behaviour of the fluid in a pore of four segments with varying radii and lengths. The results of this methods were also compared with those obtained with a conventional TMM formulation. It was found upon examination of all effective properties that there is excellent agreement between the two models in the low-frequency regime. There is no dependency on symmetry for this type of system due to the lack of local resonances.

Subsequently, using the same methodology, the effective properties for a symmetric waveguide side-loaded by M Helmholtz resonators were derived. To validate the expressions, the effective fluid properties of a waveguide side-loaded by $M = 3, 5, 10$ and 20 identical HRs obtained with the TMM summation method were compared with those obtained via the TMM multiplication method. It was found that there is excellent agreement in all terms except the effective dynamic density. It is thought these fluctuations are the result of numerical error and possess no physical meaning. Nonetheless, the influence these fluctuations play on subsequent terms is negligible. Additionally, the transmission properties obtained through the effective property model were compared with those obtained through the traditional TMM and a numerical FEM model. It was found that there was excellent agreement between the methods. It was shown that the effective property models presented within this chapter fail to capture effects resulting from evanescent coupling between Helmholtz resonators such that asymmetric absorption properties occur.

Chapter 4

Perfect Absorption with Helmholtz Resonators: One Port

Perfect absorption has been shown to be possible in a one port system through the coupling of a Helmholtz and membrane resonator by tuning the interplay of losses [13]. It has also been shown that a unit cell composed of a smaller waveguide structure side-loaded by Helmholtz resonators can achieve perfect absorption omnidirectionally [15]. This was achieved through the coupling of identical Helmholtz resonators such that the critical coupling condition was fulfilled by the accumulation of 'slow sound' [17, 18]. Through the use of multiple resonances within a one port structure it is possible to obtain broadband perfect absorption by tuning each resonance to be at a unique frequency [21]. The tuning of one port systems composed of Helmholtz resonators can also be done through the use of porous media within the cavity, allowing for the losses within the system to be adjusted such that the critical coupling condition is fulfilled [14].

In this chapter, one port systems composed of a waveguide side-loaded by a Helmholtz resonators are modelled. Analysis is undertaken on how the inclusion of a porous layer within the cavity of the Helmholtz resonator can be used to achieve perfect absorption at a single frequency and also over a broadband frequency range by also utilising the evanescent coupling between Helmholtz resonators.

One port perfect absorbers that operate for a single frequency and over a broadband frequency range are modelled as Helmholtz resonators with porous inclusions. In both cases comparisons are made to the same system without the porous inclusion, to observe the absorptive performance gain. Commentary on the strengths and limitations of the modelling methodologies is presented throughout this chapter. The one port systems developed within this chapter comprise of a single unit cell which form the basis of an acoustic metamaterial that can achieve perfect absorption of acoustic waves at frequencies which have a wavelength much larger than the sample length of the modelled metamaterial. The modelling is undertaken using the TMM, the TMM Summation low frequency approximation and numerically.

4.1 Theory

Consider a one port system composed of two rectangular waveguide sections of differing dimensions, the larger of which with a cross sectional areas S_t and the smaller one with a cross sectional area of $S_w = A_w^2$. A plane wave propagates within the larger waveguide and is incident upon the smaller waveguide section which is side-loaded by a single Helmholtz resonator. As it is a one port system, it is a purely reflective problem, as highlighted in Figure 4.1.

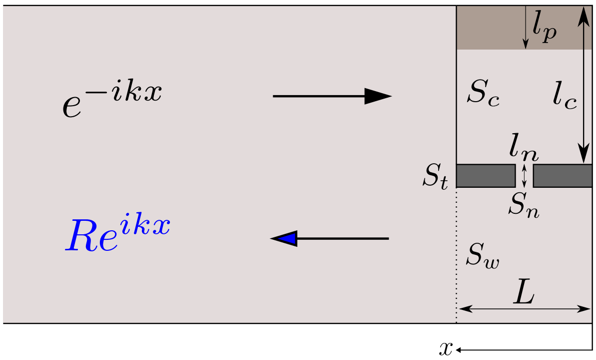

Figure 4.1: Schematic of a one port perfect absorber composed of a single Helmholtz resonator.

The Helmholtz resonator has a cylindrical neck of length l_n with a cross sectional area of $S_n = \pi r_n^2$ and a rectangular cavity of length lc with a cross sectional area of $S_c = Ac^2$. At the base of the cavity is a porous inclusion of length l_p which covers the same cross sectional area as the cavity. The total length of the system is L. The broadband perfect absorber consists of three side-loaded Helmholtz resonators, the schematic of which can be seen in Figure 4.2.

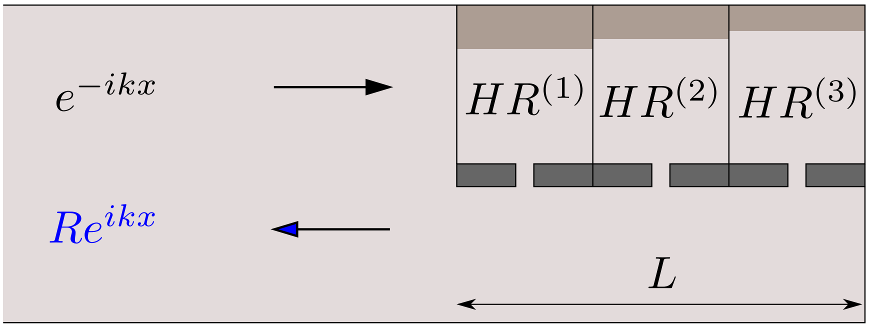

Figure 4.2: Schematic of a one port broadband perfect absorber composed of three Helmholtz resonators.

The generalised transfer matrix for a one port perfect absorber can be expressed as

$$T = M_{\Delta l} \prod_{m=1}^{M} M_{WG} \cdot M_{HR}^{(m)} \cdot M_{WG} \tag{4.1}$$

Where M_{WG} is the transfer matrix for fluid layer of length $A_c/2$ and cross sectional area S_w, $M_{HR}^{(m)}$ is the transfer matrix which introduces the m^{th} Helmholtz resonator as a point scatterer, where M is the total number of resonators in the system, and $M_{\Delta l}$ is the transfer matrix to account for the pressure radiation due to the discontinuity between the two differing waveguide cross sections. This is given by [15]

$$M_{\Delta l} = \begin{bmatrix} 1 & \mathrm{i}\omega\rho_0 \Delta l / S_w \\ 0 & 1 \end{bmatrix}, \tag{4.2}$$

and the length correction Δl is given by [85]

$$\Delta l = A_w \Omega \sum_{n=1}^{\infty} \frac{\sin^2(n\pi\Omega)}{(n\pi\Omega)^3}, \tag{4.3}$$

Where the porosity is $\Omega = S_w/S_t$. The impedance for a Helmholtz resonator with a porous inclusion within the cavity can be obtained with equation (2.67). It must be noted that within this chapter, the addition of a porous inclusion will not increase the depth of the cavity when in comparison to the non-porous alternative, i.e. $l_c^{(m)} + l_p^{(m)}$ is constant. When calculating the porosity of the sample designed for broadband absorption S_t is calculated with the largest Helmholtz resonator geometry, i.e. using $\mathbf{max}(l_c^{(m)} + l_n^{(m)})$. Within each dimension of the system an additional length of 2 mm has been added to provide boundaries with a finite thickness. These have been excluded from the analytical expressions for brevity and any difference in results would be immaterial from the ideal geometry presented here. The characteristic surface impedance is then simply calculated from the final transfer matrix as $Z_{TMM} = T_{11}/T_{21}$, allowing for the reflection and absorption coefficients to be determined.

Using the TMM Summation low frequency approximation methodology, it is possible to express the effective dynamic density of the generalised one port broadband perfect absorber as

$$\rho_{eff}(\omega) = \frac{\rho_w(\omega)}{\Omega}, \tag{4.4}$$

and the effective dynamic compressibility as

$$C_{eff}(\omega) = \Omega\left(C_w(\omega) + \frac{1}{\mathrm{i}\omega L S_w}\sum_{m=1}^{M}\frac{1}{Z_{HR}^{(m)}}\right). \tag{4.5}$$

Where $\rho_w(\omega)$ and $C_w(\omega)$ are the effective dynamic density and compressibility of the side-loaded waveguide, respectively. Similarly, the effective dynamic bulk modulus can be expressed as

$$K_{eff}(\omega) = \frac{1}{\Omega}\left(C_w(\omega) + \frac{1}{\mathrm{i}\omega L S_w}\sum_{m=1}^{M}\frac{1}{Z_{HR}^{(m)}}\right)^{-1}. \tag{4.6}$$

The effective impedance of the system can then be obtained as

$$Z_{eff}(\omega) = \frac{1}{S_t}\left(\frac{\rho_{eff}(\omega)}{C_{eff}(\omega)}\right)^{1/2} \tag{4.7}$$

and the effective acoustic wavenumber as

$$k_{eff}(\omega) = \left(\rho_{eff}(\omega)C_{eff}(\omega)\right)^{1/2}. \tag{4.8}$$

From these expressions an effective fluid layer transfer matrix can be obtained, from which the surface impedance, defined as Z_{Sum}, reflection and absorption coefficients can be obtained by constructing an effective fluid layer transfer matrix system, as detailed in Section 2.6.2.

4.2 Results

4.2.1 Perfect absorption with a single Helmholtz resonator

Within this section, results are presented highlighting how the inclusion of porous material within the cavity of a Helmholtz resonator can be used to achieve perfect absorption. This is initially done for a single resonator with which three sets of results are presented. The three scenarios are when there is; no porous inclusion resulting in an underdamped system; an optimised length of porous material to achieve perfect absorption; and a length greater than this optimised length resulting in an overdamped system. In order to achieve perfect absorption, the optimisation methodology was the method of Least Squares using the in-built MATLAB 2021b function 'lsqnonlin' with a cost function of $CF = 1 - \alpha$ at a frequency of 300 Hz and two optimisation parameters, r_n and l_n [86]. The geometry for the single Helmholtz resonator is presented in Table 4.1. The three values of l_p which are modelled are 0, 25 and 45 mm, where 25 mm is the optimised value of l_p.

r_n	l_n	A_c	l_c	A_w
2.8	4.4	40	50	40

Table 4.1: Geometric properties of the single Helmholtz resonator. All units are [mm].

Plots of the absorption coefficient obtained using the TMM, the low frequency approximation and numerically for $l_p = 0$ can be seen in Figure 4.3. From this figure it is evident that for this configuration there is excellent agreement between the three methodologies. Here the absorption peak occurs at approximately 310 Hz where $\alpha \approx 0.65$.

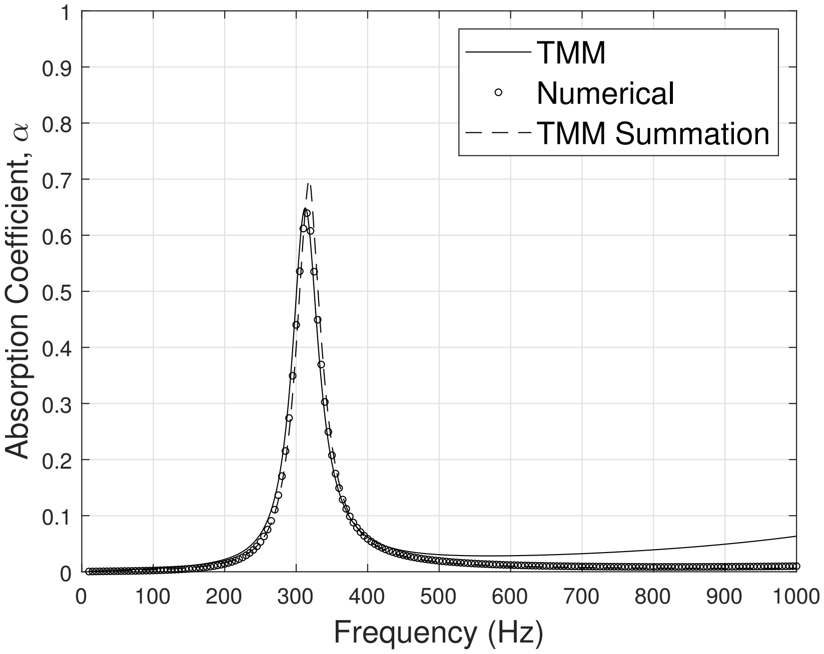

Figure 4.3: Plots of the absorption coefficients obtained using the low frequency approximation, the TMM and numerically for the single Helmholtz resonator system when l_p=0 mm.

It is evident for a system of this configuration composed of a single Helmholtz resonator that the lack of length correction for the side-loaded waveguide within the low frequency approximation results in a negligible discrepancy of approximately 5 Hz with the TMM and numerically. As such, it is acceptable to use the low frequency effective property models to help gain an understanding on the underlying physical phenomenon that is occurring at the resonant frequency of the Helmholtz resonator. Plots of the normalised dynamic bulk modulus and density obtained using the low frequency approximation can be seen in Figures 4.4a and 4.4b. From this figure it can be seen that resonance is instigated by the real component of the bulk modulus becoming negative. Plots of the normalised surface impedance obtained using the low frequency approximation (Z_{Sum}) and the TMM (Z_{TMM}) can be seen in Figures 4.4c and 4.4d.

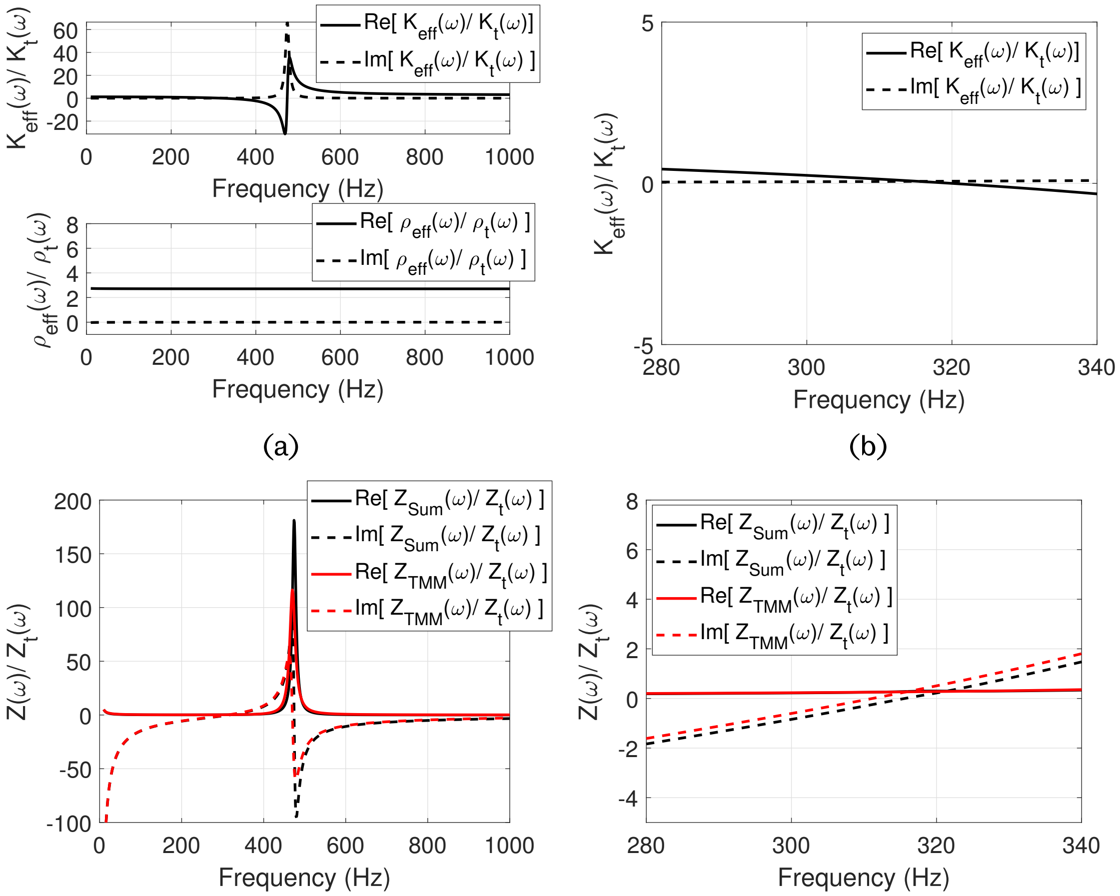

(a) (b)

(c) (d)

Figure 4.4: All effective property plots for a single Helmholtz resonator where $l_p = 0$. (a) Plots of the normalised dynamic bulk modulus and density obtained using the low frequency approximation expressions; (b) enhanced plot of the normalised dynamic bulk modulus obtained using the low frequency approximation expression; (c) plots of the normalised surface impedance obtained using the low frequency approximation and the TMM; (d) enhanced plot of the normalised surface impedance at resonance obtained using the low frequency approximation and the TMM.

From Figure 4.4c it can be seen that there is good agreement between the two analytical methodologies and that, upon comparison with the plot of the dynamic bulk modulus in Figure 4.4b, the imaginary component of the bulk modulus dictates the response of the real component of the surface impedance and subsequently the real component of the bulk modulus dictates the response of the imaginary component of the surface impedance, but with an opposite sign. Upon examination of Figure 4.4d, resonance occurs when the imaginary component of the normalised surface impedance is 0, which is a product of the bulk modulus crossing the x-axis.

At this resonant frequency, the amplitude of the absorption coefficient is determined by the value of the real component of the normalised surface impedance, where a value of 1 indicates an impedance match with the surrounding media such that no reflection occurs, resulting in perfect absorption.

Plots of the absorption coefficient obtained using the TMM, the low frequency approximation and numerically for optimised value of $l_p = 25$ mm can be seen in Figure 4.5. From this it is evident that for this configuration there is again excellent agreement between the three methodologies. Here the absorption peak occurs at 290 Hz where $\alpha = 1$ at a sample thickness of $\lambda/28$. It can therefore be determined that the introduction of the optimised length of porous material has resulted in an increase of the absorption coefficient to unity and also a reduction in the frequency at which resonance occurs by approximately 25 Hz.

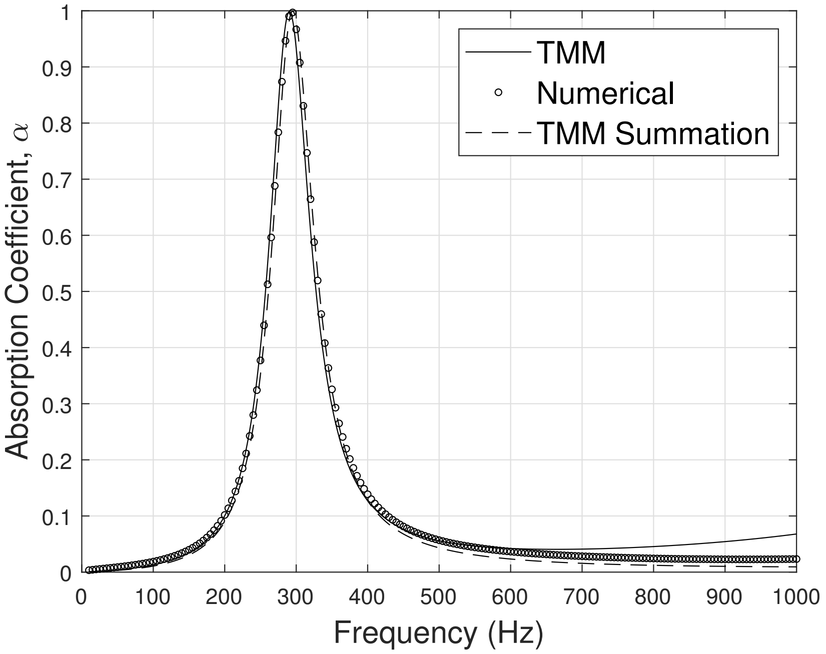

Figure 4.5: Plots of the absorption coefficients obtained using the low frequency approximation, the TMM and numerically for the single Helmholtz resonator system when l_p=25 mm.

Plots of the normalised dynamic bulk modulus and density obtained using the low frequency approximation can be seen in Figure 4.6a and an enhanced image of the dynamic bulk modulus at the resonant frequency in Figure 4.6b. Plots of the normalised surface impedance obtained using the low frequency approximation and the TMM can be seen in Figure 4.6c and an enhanced image at the resonant frequency in Figure 4.6d.

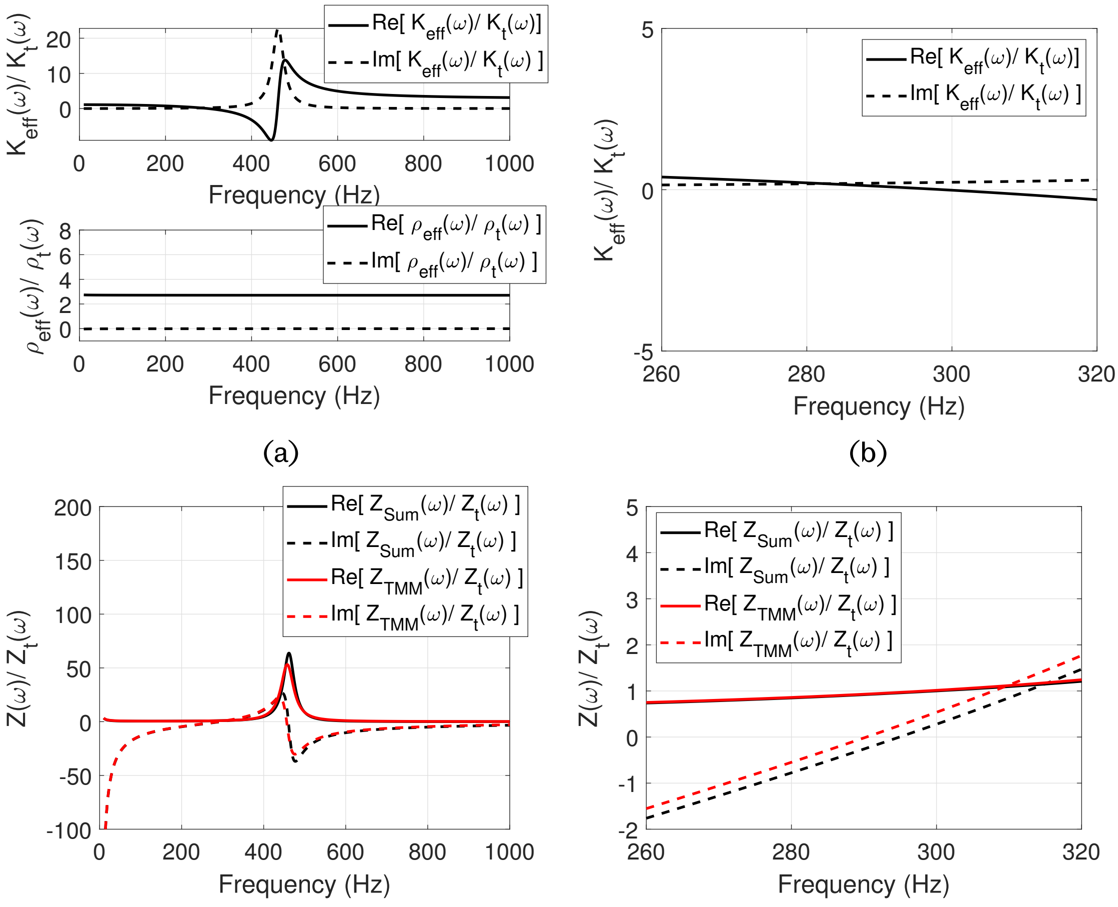

(a) (b)

(c) (d)

Figure 4.6: All effective property plots for a single Helmholtz resonator where $l_p = 25$. (a) Plots of the normalised dynamic bulk modulus and density obtained using the low frequency approximation expressions; (b) enhanced plot of the normalised dynamic bulk modulus obtained using the low frequency approximation expression; (c) plots of the normalised surface impedance obtained using the low frequency approximation and the TMM; (d) enhanced plot of the normalised surface impedance at resonance obtained using the low frequency approximation and the TMM.

Upon examination of Figures 4.6a and 4.6c in comparison with Figures 4.4a and 4.4c, it can be seen that the introduction of porous inclusion has damped the response of the dynamic bulk modulus and thus the surface impedance of the single resonator system. In Figure 4.6d it can be seen that when the imaginary component crosses the x-axis at resonance, the real value of the normalised surface impedance is 1, i.e. $Z(\omega) = Z_t(\omega)$ as Im[$Z(\omega)$]$= 0$. This also coincides with the frequency at which Re[$K_eff(\omega)$]$= 0$ in Figure 4.6b. This indicates that the introduction of the porous layer has critically coupled by the single resonator system with the surrounding medium, allowing for perfect absorption.

A numerically produced graphic showing the distribution of the acoustic pressure at resonance when perfect absorption is attained can be seen in Figure 4.7.

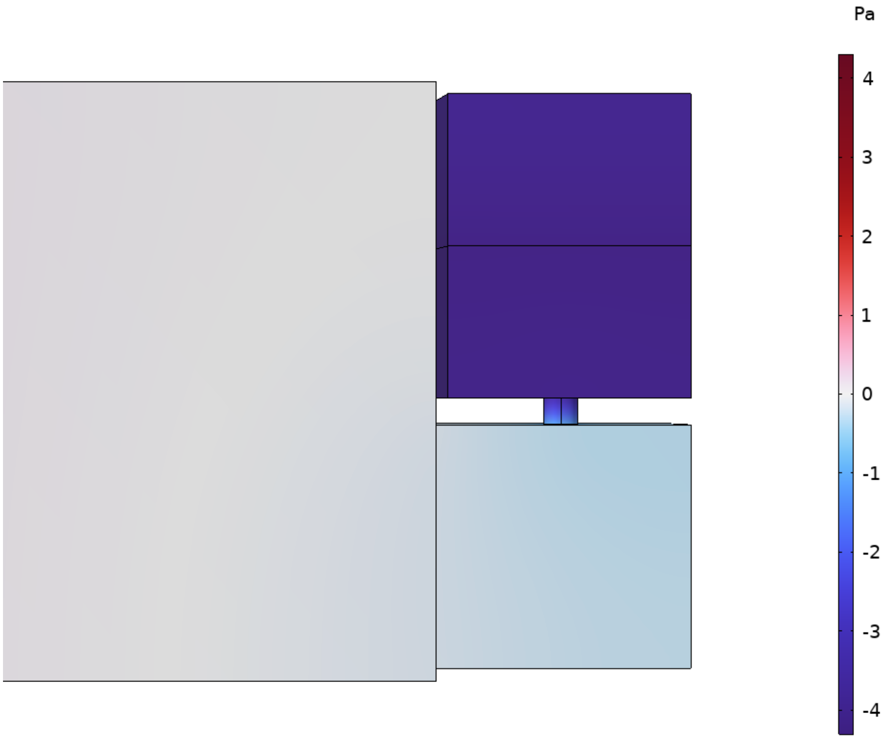

Figure 4.7: Numerically produced graphic showing the distribution of the acoustic pressure at resonance with perfect absorption

From this it can be seen that the incoming acoustic energy is contained predominantly within the cavity of the Helmholtz resonator which is indicated by the large pressure amplitude within the cavity. Within the neck there is a large pressure gradient present due to the oscillating mass of air. In the side-loaded waveguide section there is still some energy present, which could indicate the coupling between this smaller waveguide and the Helmholtz resonator. As a complete system the Helmholtz resonator and side-loaded waveguide have reduced any reflections of acoustic energy to a minimum and contained it within the metamaterial unit cell.

Plots of the absorption coefficient obtained using the TMM, the low frequency approximation and numerically for over-damped value of $l_p = 45$ mm can be seen in Figure 4.8. From this figure it is evident that for this configuration there is again excellent agreement between the three methodologies. Here, the absorption peak occurs at 280 Hz where $\alpha \approx$ 0.9. Increasing the length of porous material has resulted in a further reduction in the frequency at which resonance occurs by 10 Hz. It is also evident that with an increase in porous layer length and thus the inherent losses within the system, the more broadband the absorption becomes. This can be seen when comparing the widths of the absorption peaks in Figures 4.3, 4.5 and 4.8. This is due to the increase in porous material resulting in more leakage at resonance.

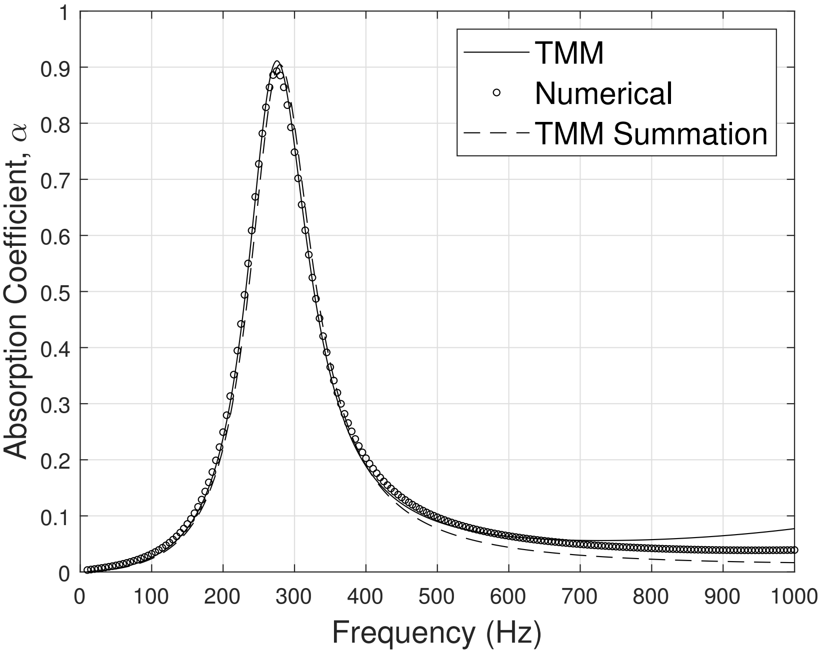

Figure 4.8: Plots of the absorption coefficients obtained using the low frequency approximation, the TMM and numerically for the single Helmholtz resonator system when l_p=25 mm.

Plots of the normalised dynamic bulk modulus and density obtained using the low frequency approximation can be seen in Figures 4.9a and 4.9b. Plots of the normalised surface impedance obtained using the low frequency approximation and the TMM can be seen in Figure 4.9c and an enhanced image at the resonant frequency in Figure 4.9d.

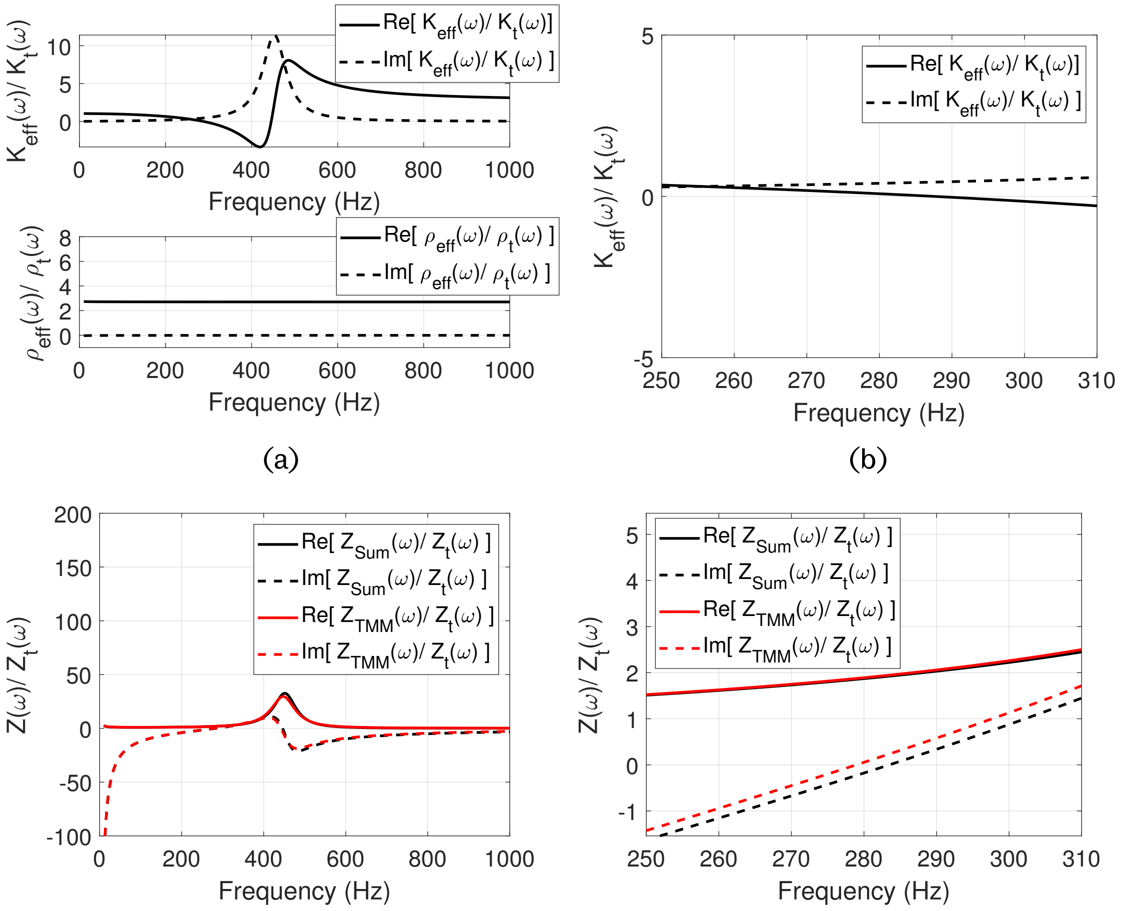

(a) (b)

(c) (d)

Figure 4.9: All effective property plots for a single Helmholtz resonator where $l_p = 45$. (a) Plots of the normalised dynamic bulk modulus and density obtained using the low frequency approximation expressions; (b) enhanced plot of the normalised dynamic bulk modulus obtained using the low frequency approximation expression; (c) plots of the normalised surface impedance obtained using the low frequency approximation and the TMM; (d) enhanced plot of the normalised surface impedance at resonance obtained using the low frequency approximation and the TMM.

Upon examination of Figures 4.9a and 4.9c in comparison with Figures 4.4a and 4.4c, it can be seen that increasing the length of the porous inclusion has further damped the response of the dynamic bulk modulus and thus the surface impedance of the single resonator system. In Figure 4.9d it can be seen that when the imaginary component crosses the x-axis at resonance, the real value of the normalised surface impedance is 2. This indicates that the system is now over-damped such that any additional losses within the system will reduce the absorption coefficient as it increases the disparity between the surface impedance of the single resonator system and the surrounding medium.

To help visualise the effect of the porous inclusion, a heatmap plot is presented in Figure 4.10 of the absorption coefficient as a function of porous inclusion length and frequency for the single Helmholtz resonator one port system. From this figure, it can be seen that there is an optimum range for the length of the porous inclusion in which perfect absorption is achieved, which for this particular system is approximately in the range $l_p = 20$ mm and $l_p = 30$ mm. Additionally, the decrease in the resonant frequency with an increase in porous inclusion length is evident, where resonance occurs at 310 Hz when $l_p = 0$ and at 285 Hz when $l_p = 45$ mm.

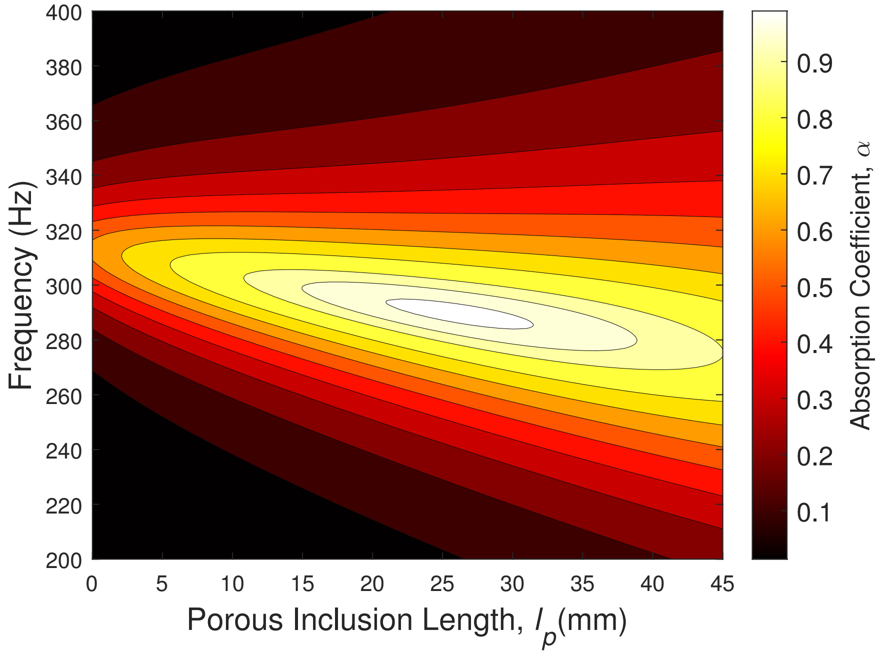

Figure 4.10: Heatmap plot of the absorption coefficient as a function of porous inclusion length, l_p [mm], and frequency [Hz].

The mechanism for perfect absorption can also be visualised with the complex frequency plane analysis method [14, 25, 26]. This is a graphical procedure which can be used to display the eigenvalues or eigenvector components of systems in the complex frequency plane. This provides useful information for the optimisation of systems to achieve perfect absorption as it can be used to determine how the addition or reduction of losses in the system will change the absorption coefficient. Some examples on the use of the complex frequency plane to achieve perfect absorption for subwavelength sized, anechoic termination type systems include those composed of resonant building blocks [16, 15], membranes [27], porous membranes [13], decorated membranes [28], bubble metascreens [29] and aerogels [30].

By inputting a complex frequency values in to the TMM model for the single resonator systems when $l_p = 0$ mm (for the lossy and lossless case), $l_p = 25$ mm and $l_p = 45$ mm, and retrieving the reflection coefficient, it is possible to create the following complex frequency plane contour plots seen in Figure 4.11.

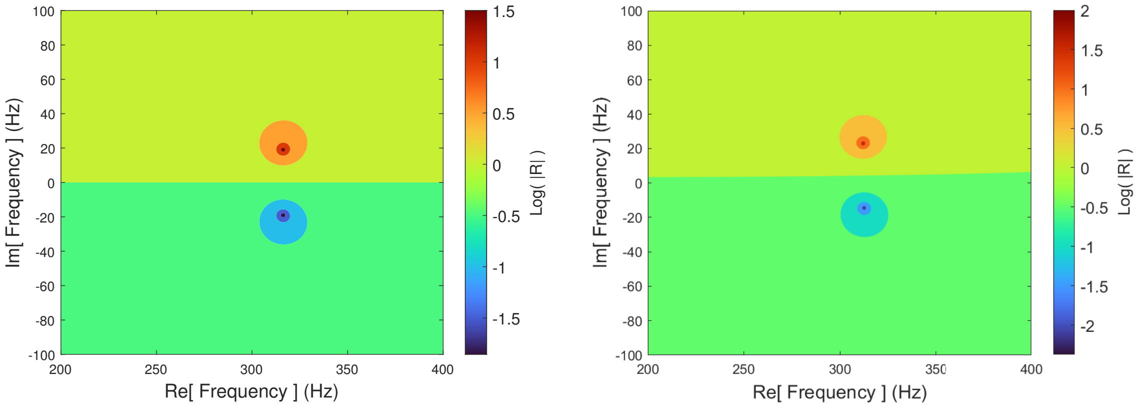

(a) l_p= 0 mm (Lossless)

(b) l_p= 0 mm

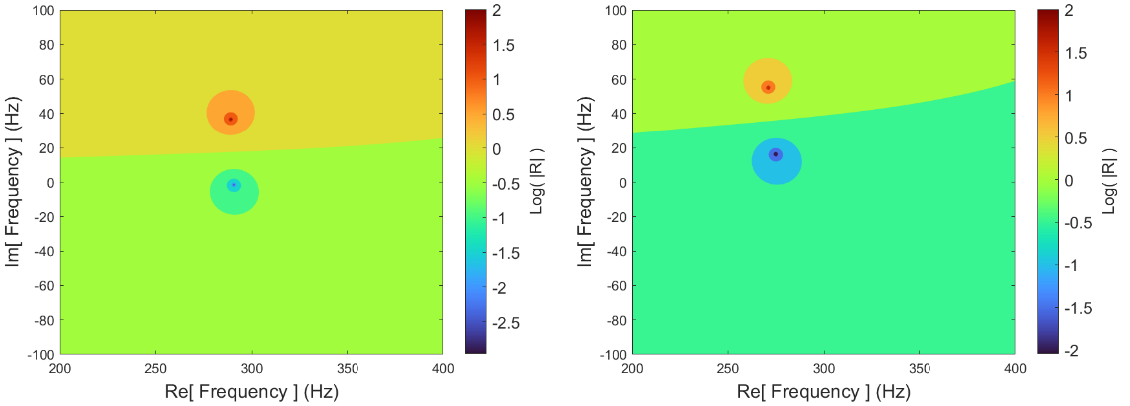

(c) l_p= 25 mm

(d) l_p= 45 mm

Figure 4.11: Complex frequency plane contour plots of the single resonator system when l_p =0 mm, l_p =25 mm and l_p =45 mm

On these plots the minimum and maximum of log$(|R|)$ are defined as the 'zero' and 'pole', respectively. The real component of the zero is the resonant frequency and the imaginary component of the zero can be used as an indication on the amount of energy leakage within the system with respect to the energy losses of the system. For the lossless case in Figure 4.11a when $l_p = 0$ mm, it is evident that the pole and zero are symmetric about the real frequency axis. When the imaginary component of the zero is negative, energy leakage from the system is greater than the energy losses of the system. This can also be seen in Figure 4.11b for when $l_p = 0$ mm in the lossy case. In comparison of these two figures it can be seen that the introduction of losses has increased the complex value of both the pole and the zero, with the zero getting closer to the real frequency axis, indicating that the losses have been increased with respect to the energy leakage of the system.

As the zero has a negative complex value, there is the option to introduce a porous inclusion within the cavity of the Helmholtz resonator to increase the inherent losses within the system until the losses in the system are equal to the energy leakage of the system, which is fulfilled when the zero lies on the real frequency axis, with no imaginary component. This is the critical coupling condition and is how perfect absorption can be achieved. The fulfilment of the critical coupling condition is evident in Figure 4.11c when $l_p = 25$ mm. Here the zero is situated on the real frequency axis, therefore perfect absorption is realised, and indicates the energy leakage of the system is now equal to the energy losses of the system.

When the length of the porous inclusion is increased such that the inherent losses of the system are now greater than the energy leakage of that system, the zero's imaginary component becomes positive. This is evident in Figure 4.11d and results in a reduction in absorption coefficient from unity. Additionally, when comparing all four plots in Figure 4.11, it can be seen that as the losses of the system are increased by increasing the length of the porous inclusion, the zero and pole are downshifted with respect to the real component of the frequency, indicating a reduction in the resonant frequency with an increase in the losses of a system. It can also be seen that in each case, the separation distance between the pole and zero remains approximately constant, indicating the introduction of losses is not changing the width of the absorption peak.

If your modelled system is such that the energy losses within the system are already greater than the energy leakage of the resonator, then the introduction of damping/ porous material will hinder the absorptive performance of the system. This is because the zero of the unaltered system will already have a positive imaginary component and therefore the introduction of any additional losses will shift the zero further away from the real frequency axis and thus the critical coupling condition.

4.2.2 Broadband perfect absorption with Helmholtz resonators

Within this section, results are presented for the broadband perfect absorber which builds upon the phenomenon described for a single resonator perfect absorber. Here, the one port system consists of three Helmholtz resonators of differing resonant frequencies. Results are presented highlighting the difference between the inclusion porous material of an optimised length within the cavity of each resonator and without a porous inclusion within each resonator cavity. To achieve an optimised geometry, the Least Squares method of optimisation was again used by utilising the in-built MATLAB function 'lsqnonlin'. This time the cost function was defined as

$$CF = (f_1 - f_0) - \int_{f_0}^{f_1} \alpha \; df, \tag{4.9}$$

where f_1 and f_0 are the upper and lower bounds of the desired frequency range, respectively. For the bounds $[200, 600]$ Hz, an optimised geometry was obtained and can be seen in Table 4.2. An additional wall thickness of 2 mm is incorporated within the geometry such that the design can be replicated experimentally if desired. The total length of the system is $L = 12.6$ cm.

HR	r_n	l_n	A_c	l_c	l_p
1	8.6	2.0	40	50	42.6
2	5.0	2.7	40	50	45.0
3	2.5	2.7	40	50	39.2

Table 4.2: Geometric properties of the broadband perfect absorber Helmholtz resonator system. All units are [mm].

Plots of the absorption coefficient obtained using the TMM, the low frequency approximation and numerically can be seen in Figure 4.12.

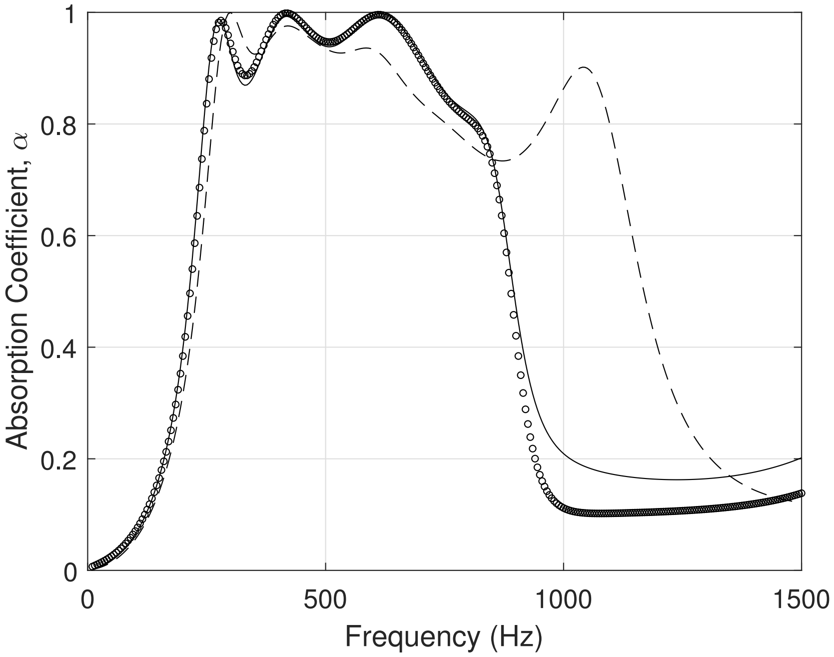

(a) With porous inclusions

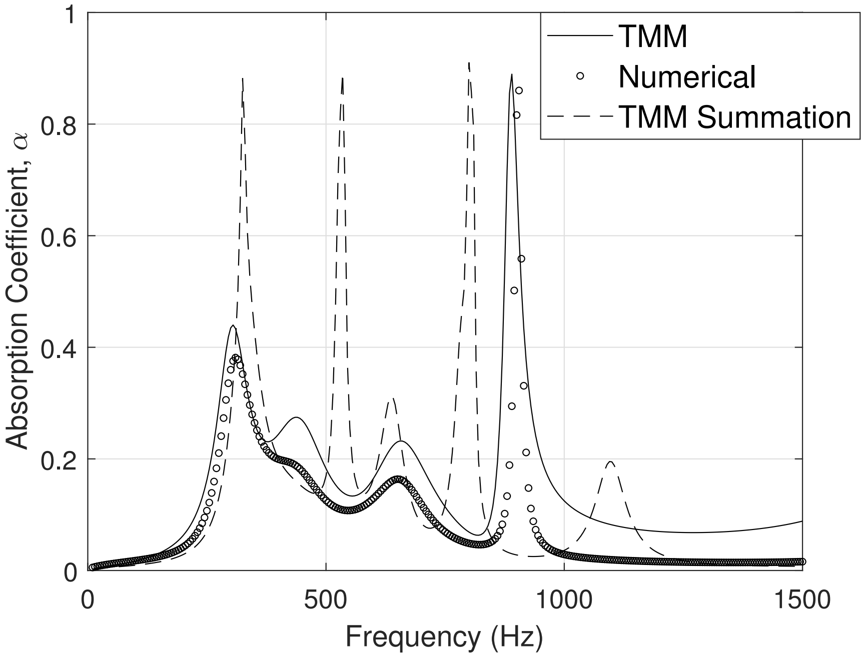

(b) Without porous inclusions

Figure 4.12: Plots of the absorption coefficient for an optimised one port perfect absorber consisting of three Helmholtz resonators, with and without porous inlcusions.

From Figure 4.12 it can be seen that there is excellent agreement between the TMM and numerical results at the three peaks associated with the Helmholtz resonators. These are the first three peaks occurring at approximately 275 Hz, 425 Hz and 625 Hz. At each of these frequencies near unity absorption is achieved by using the porous layer to optimise the energy leakage and losses such that critical coupling is achieved, resulting in a thickness of $\lambda/10$ at the lowest frequency absorption peak. Upon comparison with the low frequency approximation model, there is a reasonable agreement at the first two resonances, but above this there is a disparity when in comparison to results produced with the TMM and numerically. Additionally, there is a disagreement in the absorption coefficient obtained using the TMM and numerically at approximately 800 Hz. Absorption at this frequency is facilitated by the quarter wavelength resonance produced by the waveguide which the Helmholtz resonators side-load. This discrepancy is most prevalent in Figure 4.12b where no porous inclusion is present.

To help visualise this described phenomenon when perfect absorption is achieved, numerically produced graphics showing the distribution of the acoustic pressure at each resonance for the broadband perfect absorber are presented in Figure 4.13. Each graphic corresponds to a different resonance frequency; Figure 4.13a depicts the total pressure distribution at the lowest resonant frequency of 275 Hz, the resonant frequency of $HR^{(3)}$; 4.13b depicts the total pressure distribution at 425 Hz, the resonant frequency of $HR^{(2)}$; 4.13c depicts the total pressure distribution at 625 Hz, the resonant frequency of $HR^{(1)}$; 4.13d depicts the total pressure distribution at 800 Hz, the quarter wavelength resonant frequency of the side-loaded waveguide itself.

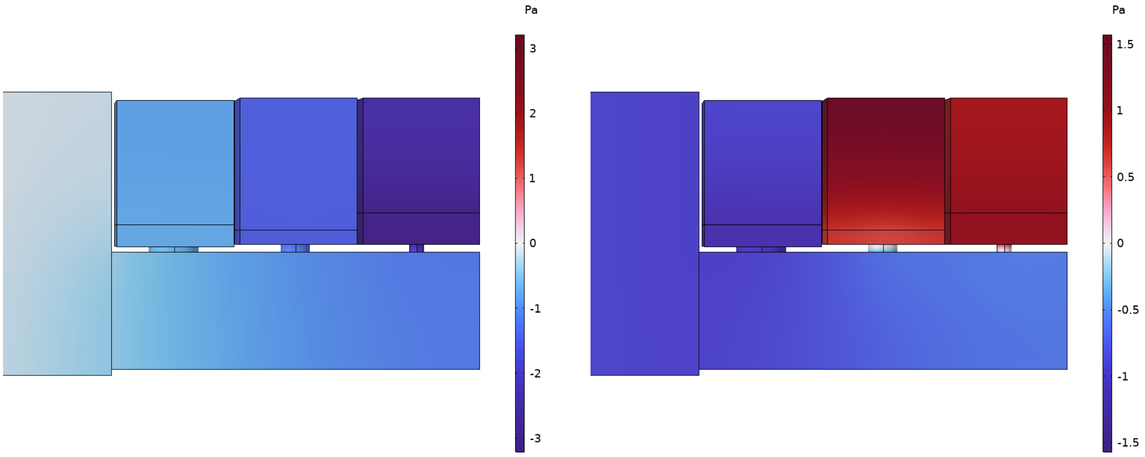

(a) 275 Hz (b) 425 Hz

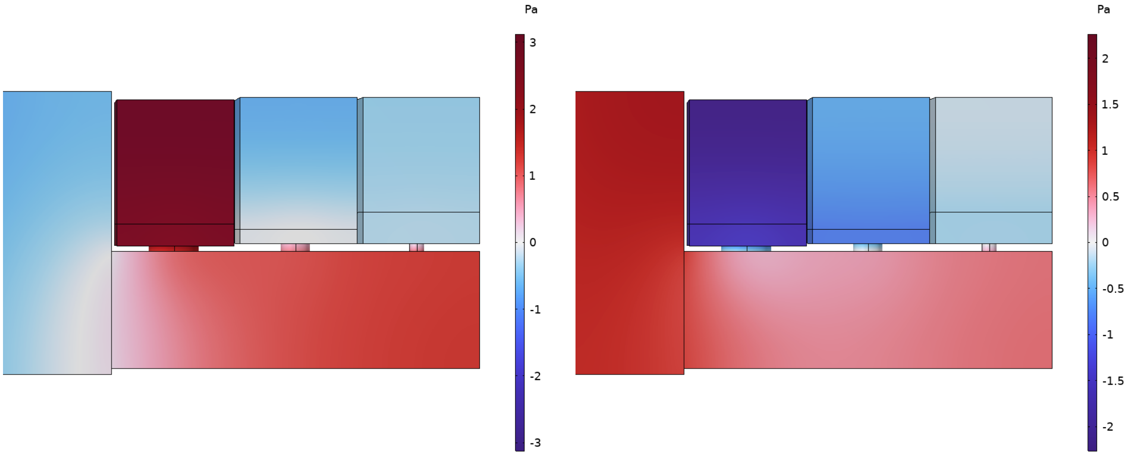

(c) 625 Hz (d) 800 Hz

Figure 4.13: Numerically produced graphic showing the acoustic pressure distribution at each resonant frequency of the broadband perfect absorber.

Additionally, plots of the absorption coefficients for each resonant element of the perfect absorber can be seen in Figure 4.14. These plots were obtained using the TMM and in each case the side-loaded waveguide length remained constant. Therefore, in addition to the total absorption coefficient of the system, there is also the absorptive response of each individual resonator when coupled with the waveguide, as well as the waveguide un-sideloaded.

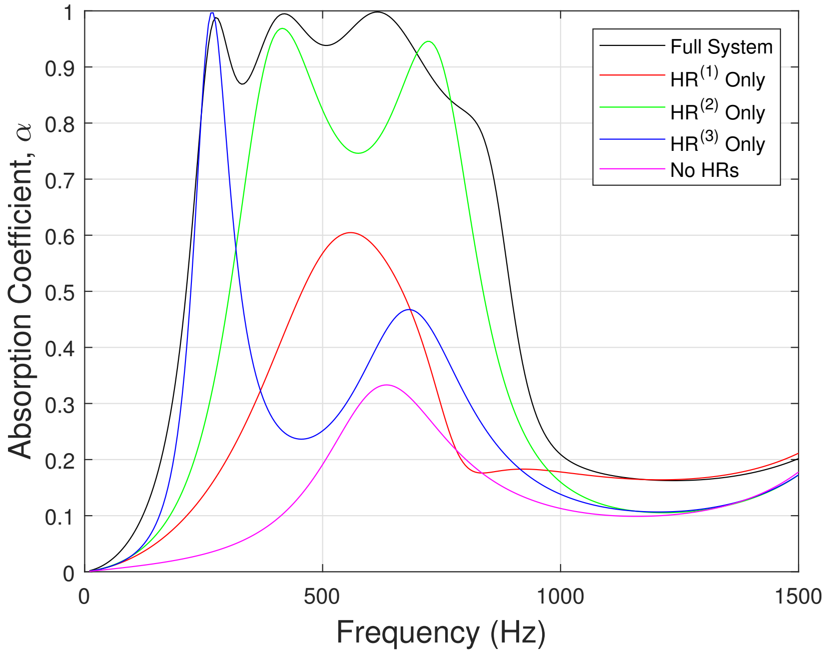

Figure 4.14: Plots of the absorption coefficient for each resonant element of the perfect absorber. Calculated with the TMM.

Upon examination of Figure 4.13a in combination with Figure 4.14 it is evident that $HR^{(3)}$ is loosely coupled to the rest of the system with nearly all of the absorptive performance at this frequency coming from this resonator alone. Some coupling is evident in Figure 4.14 as the absorption peak created by the quarter wavelength resonance has been slightly shifted to a higher frequency with an increase in absorption coefficient. In Figure 4.13b it can be seen that both $HR^{(2)}$ and $HR^{(3)}$ contributing to absorption at 425 Hz, with the rest of the system being out of phase. In Figure 4.14 it can be seen that there is very strong coupling between $HR^{(2)}$, indicated by the shift in frequency and also large increase in absorption coefficient of the quarter wavelength resonance. At 625 Hz it appears $HR(1)$ is strongly coupled with the waveguide, with little interaction with $HR(2)$ and $HR(3)$. This can be seen in Figure 4.13c by the strong in phase response of the resonator and waveguide and in Figure 4.14 by the singular pronounced absorption peak, indicating the resonant frequency of $HR^{(1)}$ is very close to that of the waveguide. This peak is very broadband with a reduced amplitude, which is typical for resonators with a large cross sectional area of neck in relation to the cavity [87]. When looking at the total absorptive performance of the system in Figure 4.14, it is evident the quarter wavelength absorption peak has been shifted to approximately 800 Hz by the Helmholtz resonators. The pressure distribution at this frequency can be seen in Figure 4.13d. Here it can be seen that there is a relationship between the width of the resonator neck and how strongly coupled with the waveguide the resonator is, with the wider neck resulting in stronger coupling. This could be due to the acoustic inertance for a Helmholtz resonator with a wider neck being lower than that of a resonator with a narrow neck, allowing for stronger coupling.

When comparing the low frequency approximation plots produced using the TMM Summation method with those of the other two methodologies in Figure 4.12, it can be seen that whilst resonance broadly occurs at the same frequency, absorption is much greater in amplitude. There is also an additional absorption peak at 600 Hz. To further investigate the discrepancy between the low frequency approximation and the numerical and semi-numerical TMM approaches seen in Figures 4.15a and 4.15b, plots are produced of the same system, but with the sequential order at which the Helmholtz resonators are situated along the waveguide varied. This is to determine the effect of evanescent coupling, which is not captured using the low frequency approximation model. These plots are presented within Figure 4.15 for all six permutations of Helmholtz resonator order, with and without a porous inclusions.

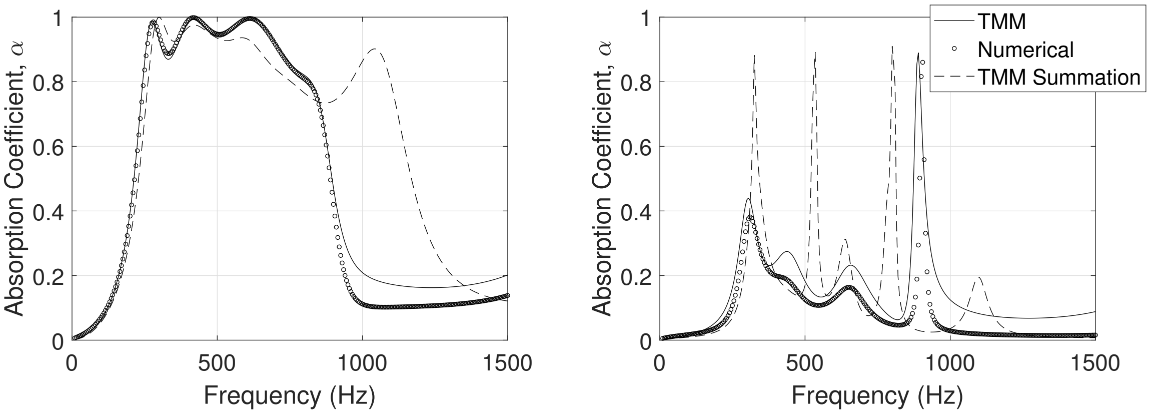

(a) HR1 → HR2 → HR3 with Porous Inclusion

(b) HR1 → HR2 → HR3 without Porous Inclusion

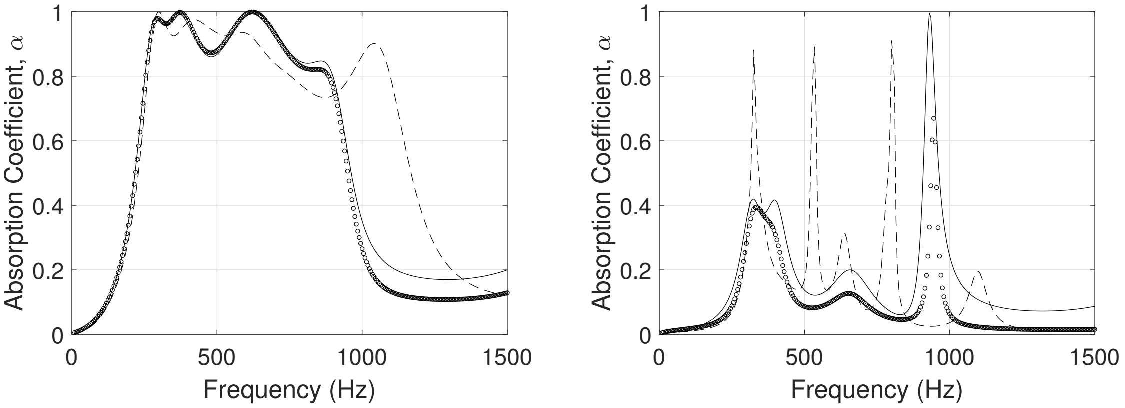

(c) HR1 → HR3 → HR2 with Porous Inclusion

(d) HR1 → HR3 → HR2 without Porous Inclusion

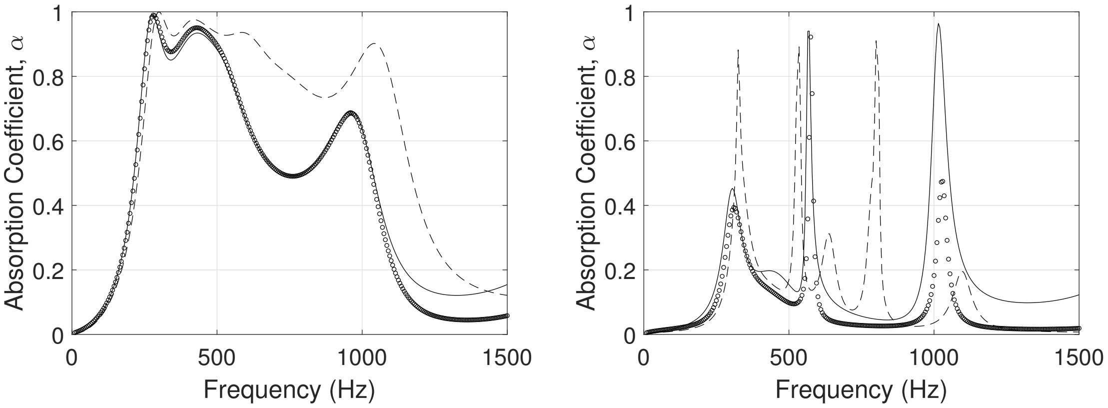

(e) HR2 → HR1 → HR3 with Porous Inclusion

(f) HR2 → HR1 → HR3 without Porous Inclusion

From this figure it is evident for each permutation of Helmholtz resonator order, different absorption coefficients are obtained. This highlights the influence the

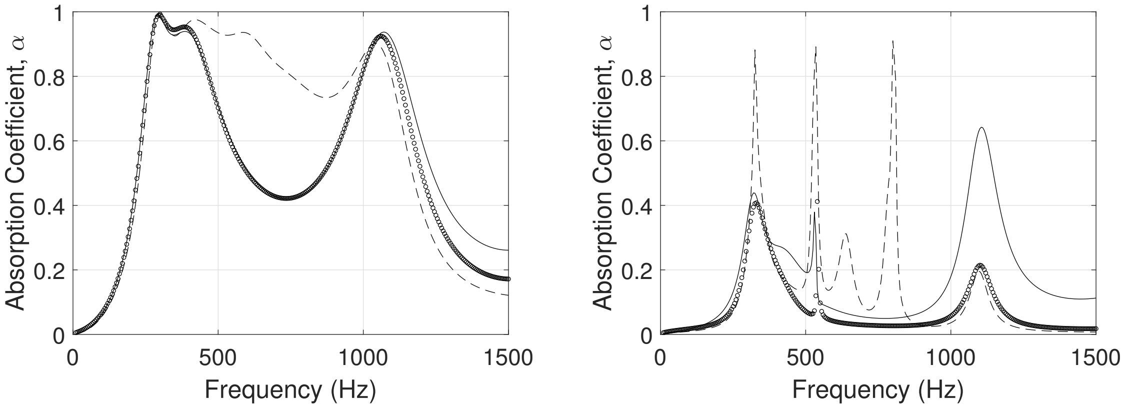

(g) HR2 → HR3 → HR1 with Porous Inclusion

(h) HR2 → HR3 → HR1 without Porous Inclusion

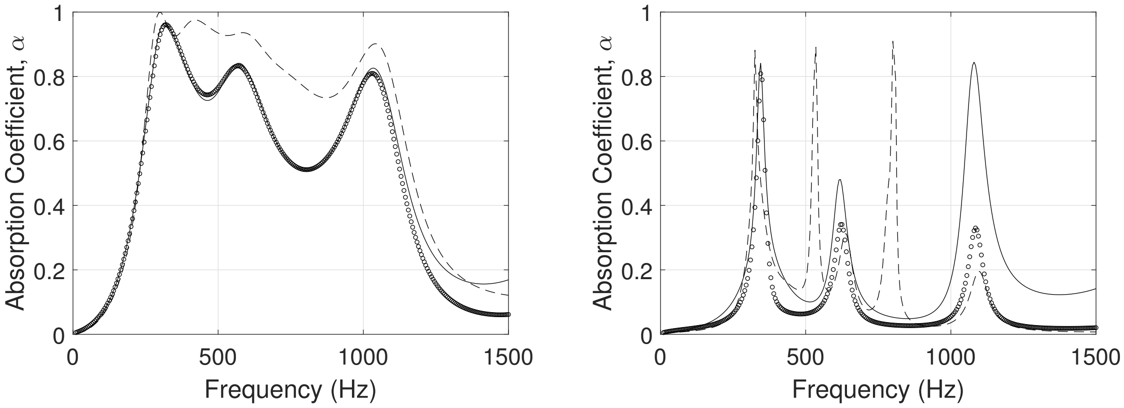

(i) HR3 → HR1 → HR2 with Porous Inclusion

(j) HR3 → HR1 → HR2 without Porous Inclusion

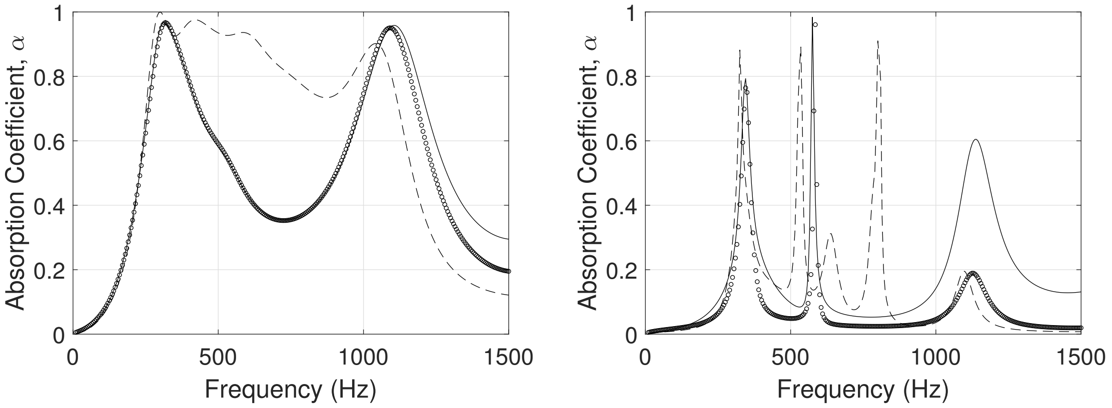

(k) HR3 → HR2 → HR1 with Porous Inclusion

(l) HR3 → HR2 → HR1 without Porous Inclusion

Figure 4.15: Plots of the absorption coefficient for all six permutations of resonator order using the optimised Helmholtz resonator geometry, with and without the optimised porous inclusion. Produced using the TMM, Numerically and with the low frequency approximation using the TMM Summation method.

evanescent coupling that occurs between the resonators and the waveguide has on the total response of the system. This phenomenon is present for each permutation with and without the porous inclusions. When assessing the influence of the order of resonators on the individual resonant frequencies, it can be seen that the initial resonator in the series plays an important part. When HR1 is the first in the series, as in Figures 4.15a, 4.15b, 4.15c and 4.15d, the responses of each resonator occur at the same frequencies, albeit with varying degrees of absorption. This is also evident when HR2 is the first in the series, as in Figures 4.15e, 4.15f, 4.15g and 4.15h; and additionally when HR3 is the first in the series, as in Figures 4.15i, 4.15j, 4.15k and 4.15l. Interestingly, the absorptive performance and the resonant frequency of HR3 remains consistent throughout all the permutations, indicating the resonator was much more loosely coupled with the rest of the system than the other resonators. This could be a resultant of the high acoustic inertance due to the narrow neck region and low resonant frequency.

Within each plot of Figure 4.15, plots of the absorption coefficient determined using the low frequency approximation of the TMM Summation method are presented. These plots are identical for each permutation for both cases of with and without the porous inclusions. This is due to the low frequency approximation linearly summing the Helmholtz resonator impedances over the length of the system, which fails to account for prior Helmholtz resonances altering the effective fluid properties of the waveguide such that the response of subsequent resonators is altered. It can be seen that whilst the absorption coefficients of the two cases of with and without porous inclusions bares a resemblance to the plots produced using the TMM and numerically, there is disagreement in all of the plots. Highlighting the limitation of the low frequency approximation for multi resonator system in which evanescent coupling is prevalent.

4.2.3 Semi-Numerical TMM Approach

Upon further examination of Figure 4.15, it is evident that there is a disagreement between three methodologies when determining absorption resulting from the quarter wavelength resonance when there is no porous inclusion present. When comparing the TMM and numerical plots of the absorption coefficient, it can be seen that the resonant frequencies are consistent, but the extent of absorption is over-estimated with the TMM when no porous inclusions are present. This is a consequence of the Helmholtz resonators influencing the end correction, which is not captured in equation 4.3 [17]. Instead of a singular real valued length, the end correction becomes complex and frequency dependant, explaining the disparity between the absorption peaks between the two methodologies due to the numerical modelling capturing this phenomenon.

However, it can also be seen that there is good agreement between the TMM and numerical plots when the porous inclusions are present. This indicates the addition of the porous material has damped the response of the individual resonators such that they have a reduced impact on the response of the side-loaded waveguide.

Finally, using the low frequency approximation model it can be seen that there is an over-estimation of the frequency at which the absorption peak occurs by approximately 200 Hz in Figure 4.15a. This is due to the lack of end correction being present within the approximation expressions, which add an effective length to the system, lowering the resonant frequency.

Here a semi-numerical approach is presented to obtain the radiation impedance for the side-loaded waveguide at the discontinuity between the the two waveguide sections. The frequency dependant length correction can be determined semi-numerically by first determining the numerically calculated impedance, $\mathcal{Z}$, with the following expression

$$\mathcal{Z} = \left(\frac{1+\mathcal{R}}{1-\mathcal{R}}\right) Z_0, \tag{4.10}$$

where $\mathcal{R}$ is the numerically determined reflection coefficient. By using the analytical surface impedance determined using the TMM, the following relation can be used to calculate the radiation impedance

$$\mathcal{Z} - Z_{TMM} = \frac{\mathrm{i}\omega\rho_0\Delta l}{S_w}. \tag{4.11}$$

Plots of the absorption coefficient obtained using numerically, semi-numerically and with the low frequency approximation for all permutations can seen in Figure 4.16

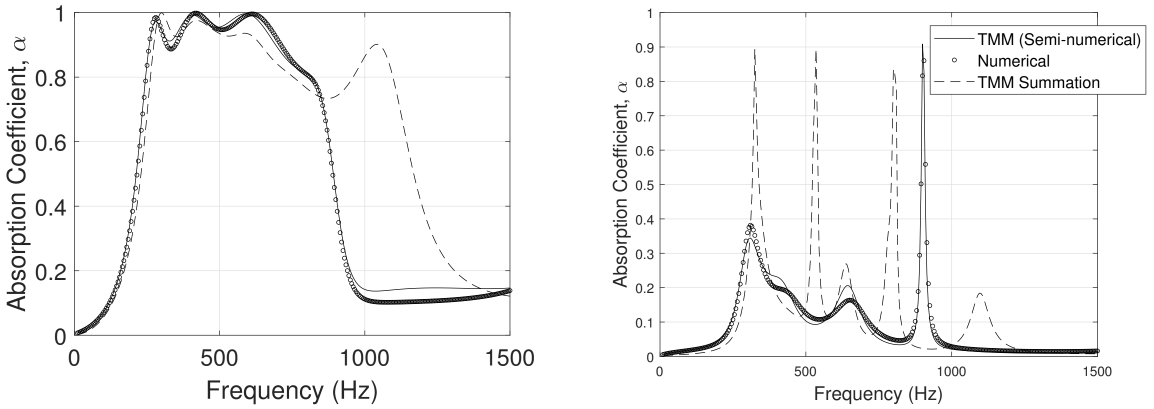

(a) HR1 → HR2 → HR3 with Porous Inclusion

(b) HR1 → HR2 → HR3 without Porous Inclusion

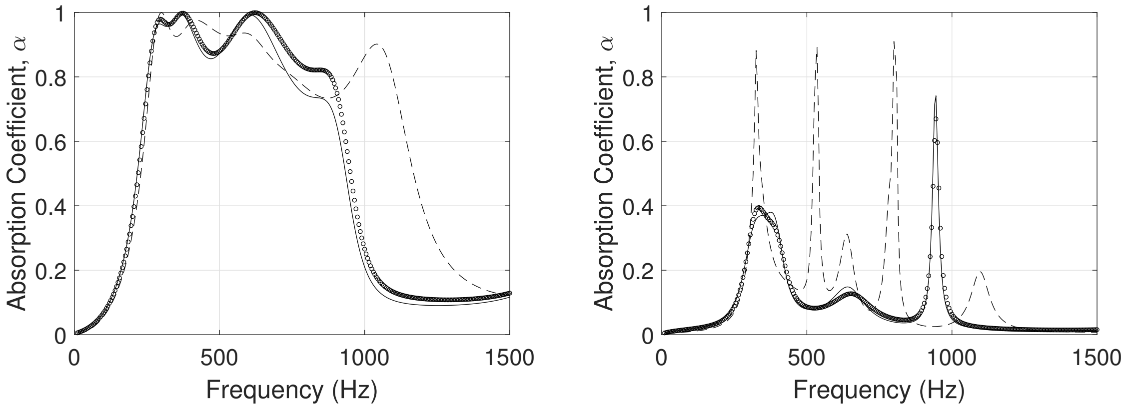

(c) HR1 → HR3 → HR2 with Porous Inclusion

(d) HR1 → HR3 → HR2 without Porous Inclusion

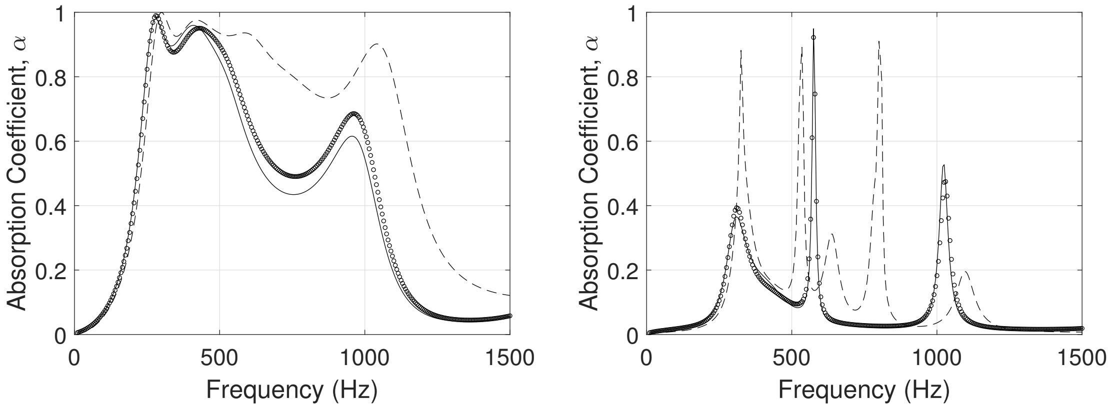

(e) HR2 → HR1 → HR3 with Porous Inclusion

(f) HR2 → HR1 → HR3 without Porous Inclusion

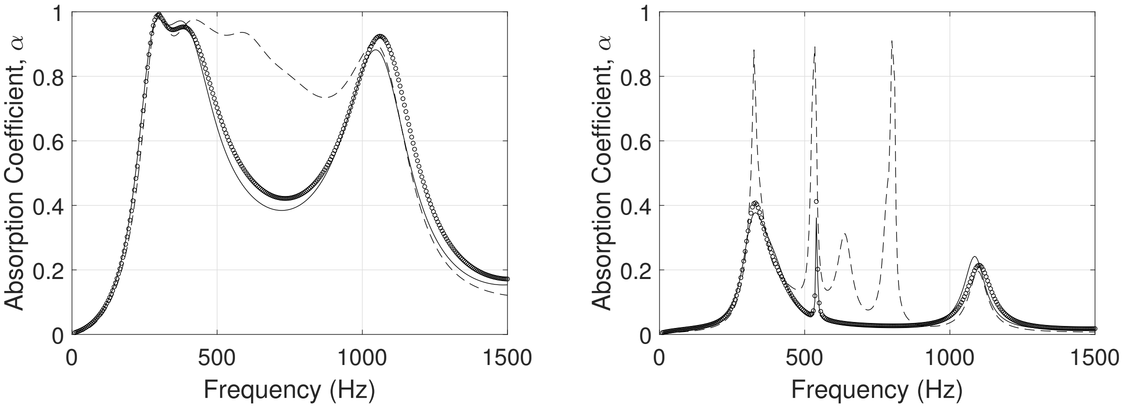

(g) HR2 → HR3 → HR1 with Porous Inclusion

(h) HR2 → HR3 → HR1 without Porous Inclusion

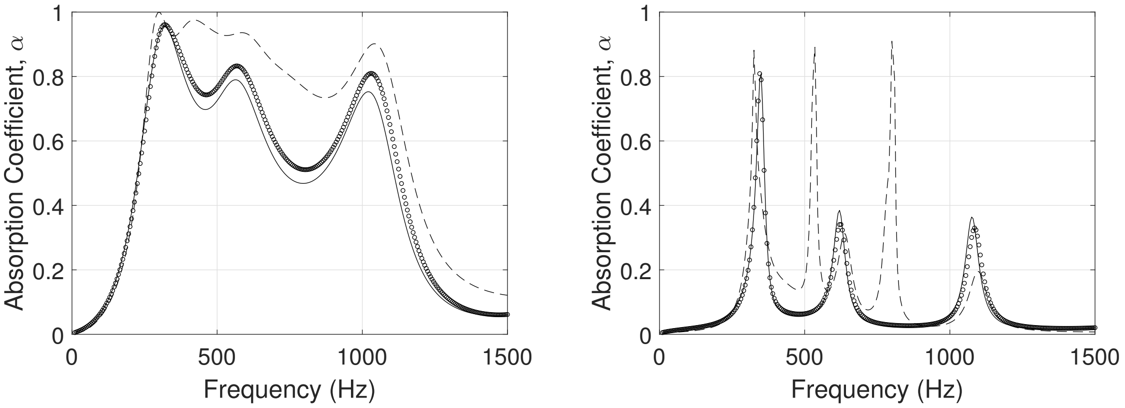

(i) HR3 → HR1 → HR2 with Porous Inclusion

(j) HR3 → HR1 → HR2 without Porous Inclusion

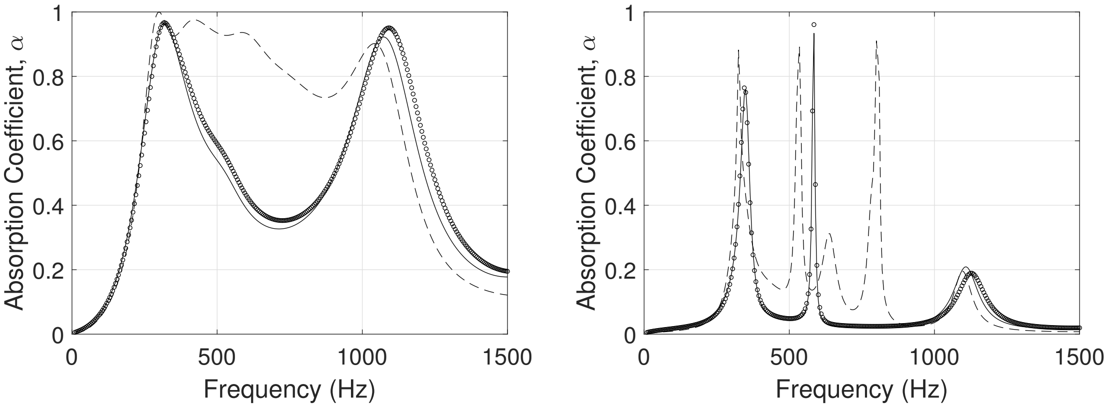

(k) HR3 → HR2 → HR1 with Porous Inclusion

(l) HR3 → HR2 → HR1 without Porous Inclusion

Figure 4.16: Plots of the absorption coefficient for all six permutations of resonator order using the optimised Helmholtz resonator geometry, with and without the optimised porous inclusion. Produced using the Semi-numerical TMM, Numerically and with the low frequency approximation using the TMM Summation method.

When comparing the plots in Figure 4.16 with those in Figure 4.15, it can be seen that the semi-numerical approach has rectified the discrepancies seen between the analytical and numerical predictions of the absorption coefficient from the quarter wavelength response of the side-loaded waveguide when no porous inclusions are present. This further highlights the influence Helmholtz resonators play on the radiation impedance term and why it can be necessary to use the semi-numerical methodology to account for this; exposing the limitations of using length corrections which are simply functions of the waveguide geometry and porosity.

However, whilst there is still good agreement between the semi-numerical and numerical plots within Figure 4.16 when the porous inclusions are present, the agreement has not been improved when in comparison to the full analytical plots in Figure 4.15. This indicates that since the porous inclusions have reduced the influence of the Helmholtz resonators upon the quarter wavelength response, it is unnecessary to compute the compute the radiation impedance semi-numerically. It can therefore be concluded that the semi-numerical approach is not necessary for a system of this configuration if there is a significant amount of damping facilitated by porous inclusions.

4.3 Chapter Conclusion

Within this chapter, the mechanism to achieve perfect absorption for a one port system has been explored with the development of single frequency and broadband perfect absorbing acoustic metamaterial unit cells. This was achieved at a single frequency using a single Helmholtz resonator, and over a broadband frequency range with a system of three Helmholtz resonators. The main premise that has been explored is on the use of porous inclusions to help optimise the acoustic properties of the Helmholtz resonators such that the system becomes critical coupled with the outer waveguide at each resonant frequency.

It has been shown that with the assistance of a numerical optimisation algorithm, perfect absorption at a specified frequency can be achieved with a single HR system with the use of a porous inclusion. This was achieved at a frequency of 290 Hz with a sample thickness of $\lambda/28$. Then, either reducing or increasing the length of the optimised porous inclusion length will either underdamp or overdamp the system, respectively. The physical meaning of achieving critical coupling has been highlighted by showing how the normalised surface impedance is equal to one when perfect absorption is achieved, i.e. the real component of the surface impedance of the metamaterial system is equal to the real component of the fluid within the main waveguide. In the analysis of the single Helmholtz resonator system, it has also been shown that there is excellent agreement between the TMM, numerical and low frequency approximation.

An alternative visual representation of the critical coupling condition was presented via plots of the reflection coefficient within the complex frequency domain obtained with the TMM. Using this methodology allows the poles and zeros of a system to be identified, with the location of the zeros in the complex frequency plane a useful metric in determining how the use of a porous inclusion will influence the energy leakage and intrinsic losses within the system. If the system is underdamped, the zero will be in the negative complex plane. By the introduction of a porous inclusion with an optimised length, the complex value of the zero was increased to zero, fulfilling the critical coupling condition. Further increase of the porous inclusion length increased the complex value of the zero, breaking the critical coupling of the system.

Using this same methodology with a numerical optimisation algorithm designed to operate over a specified frequency range, it was possible to produce a broadband perfect absorbing metamaterial unit cell consisting of three Helmholtz resonators. Here broadband perfect absorption was obtained with a sample thickness of $\lambda/10$ for the lowest frequency perfectly absorbed. Using graphics produced numerically of the absolute acoustic pressure at the four resonant frequencies of the system, insight into how each resonator was coupled within the system was gained. This highlighted that there is significant evanescent coupling between the Helmholtz resonators and the waveguide. To further explore this coupling, absorption coefficient plots for all six permutations of resonators was produced. This highlighted how the order of resonator placement in regards to their resonant frequency was important, with going to highest to lowest frequency yielding the best absorptive results.

Finally, a discrepancy between the quarter wavelength absorptive response produced from all three methodologies was observed. The low frequency approximation produced poor agreement due to the lack of length correction for the pressure radiation at the discontinuity at the interface of the two waveguides. The TMM produced accurate results with a porous layer present, but over estimated the absorptive performance of the quarter wavelength response when no porous inclusions were present, with respect to the numerical results. This indicated that the inclusion of the porous layer damped the resonators such that they had little influence on the quarter wavelength response, but when no porous media was present, they had a large influence. The account for the influence of the Helmholtz resonators on the length correction, a semi-numerical approach was presented in which the pressure radiation impedance was obtained. This resulted in excellent agreement for the systems with no porous inclusions, but no further improvement was obtained for the systems with porous inclusions.

Chapter 5

Perfect Absorption with Helmholtz Resonators: Two Port

As discussed for one port systems in Chapter 4, perfect absorption can be achieved through the utilisation of Helmholtz resonators such that the critical coupling condition is fulfilled through an impedance match with the surrounding medium. Within this chapter, the use of Helmholtz resonators with porous inclusions within the cavity will be explored for achieving perfect absorption in two port systems at both a single frequency, and also over a broadband frequency range.

To date, a number of methodologies have been employed to achieve perfect absorption in two port systems. For example, two port perfect absorption has been realised through a process of 'coherent perfect absorption', which is enabled by the control of input acoustic waves in both propagative directions [31]. Through the use of a subwavelength resonant metamaterial structure, the effective acoustic properties can be tuned such that perfect absorption can be achieved. This requires the manipulation of the relative phase between impinging acoustic waves and allows for the absorption coefficient to be tuned from zero to unity [32].

The absorptive properties of two port structures can typically be simplified into two types of systems. Those that exhibit asymmetrical sound absorption properties, and those that are mirror symmetric and exhibit symmetrical sound absorption properties. There has been a large body of work on achieving perfect absorption with systems that exhibit asymmetrical absorptive properties.

As the maximum absorption coefficient attainable for one-sided absorption by a point symmetric scatterer is $\alpha = 0.5$ [31], multiple resonances are typically required to achieve perfect absorption. This can be achieved through the degenerate coupling of Helmholtz resonators in which a detuning parameter can be utilised such that strong coupling between the Helmholtz resonators is achieved and an impedance match condition is met for a single propagative direction [42]. When this directional impedance match condition is met, this same boundary acts as an acoustically soft boundary in the opposing direction, resulting in near-perfect reflection. As these types of systems are typically reciprocal in nature, the transmission coefficient does not vary with propagation direction. Therefore, the duality of the impedance matching condition coinciding with a sound soft boundary in the opposing propagative direction is required to maintain an equal transmission coefficient for both propagative directions [44].

Through the use of multiple degeneratively coupled Helmholtz resonators, it has been shown that perfect and broadband absorption can be achieved over a range of frequencies with rainbow trapping [45], or at targeted frequencies with multiple pairs of detuned Helmholtz resonators [42, 44, 47]. Other resonant structures such as micro-perforated panels can be utilised to the same effect [48].

Finally, it has been shown that through the use of degeneratively coupled resonators, mirror symmetric perfect absorption can be achieved in optics [49] and acoustics through the use of Helmholtz resonators [50] and with coupled membrane resonators [51].

Within this chapter, the use of degeneratively coupled Helmholtz resonators for asymmetric absorption will be explored. The detuning parameter in this instance will be a porous inclusion within the cavities of the resonators. The mechanisms behind achieving perfect absorption will be displayed and a perfect absorber at a single frequency and also over a broadband frequency range will be modelled. All analytical models will be validated with 3D FEM models.

5.1 Theory

Consider a two port system composed of one large waveguide section with a cross sectional areas S_t, in which a system of M Helmholtz resonators are placed which are of differing lengths such that the cross sectional area of the waveguide varies with each subsequent Helmholtz resonator. The resonator specific cross sectional area is denoted as $S^{(m)}$ for the m^{th} resonator. This change in cross section for subsequent Helmholtz resonators is to aid in the critical coupling of each resonator, as presented for a rainbow trapping absorber in [45]. A plane wave propagates within the large waveguide and is incident upon the system of Helmholtz resonators. A graphic depicting the system for $M = 2$ is presented in Figure 5.1.

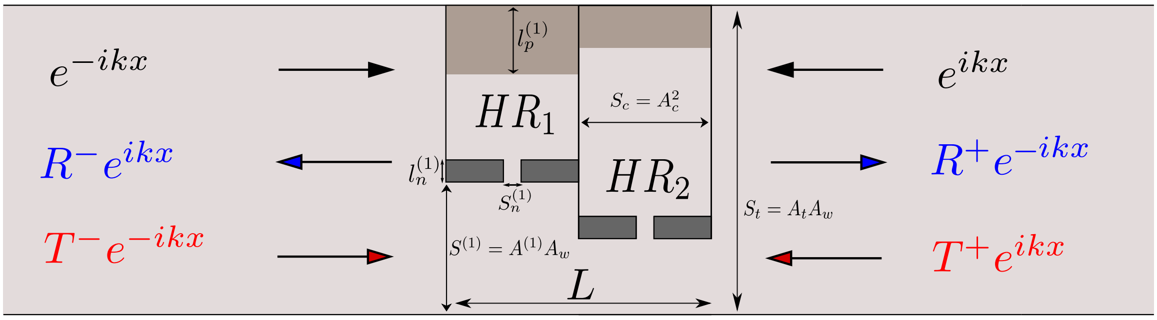

Figure 5.1: A graphic depicting a system for $M = 2$ Helmholtz resonators in a two port system.

The m^{th} Helmholtz resonators has a cylindrical neck of length $l_n^{(m)}$ with a cross sectional area of $S_n^{(m)} = \pi(r_n^{(m)})^2$ and a rectangular cavity of length $lc^{(m)}$ with a cross sectional area of $S_c = Ac^2$, which is kept constant for all values of m. At the base of the cavity is a porous inclusion of length $l_p^{(m)}$ which covers the same cross sectional area as the cavity. The total length of the system is L. The broadband perfect absorber consists of $M = 4$ Helmholtz resonators, the schematic of which can be seen in Figure 5.2.

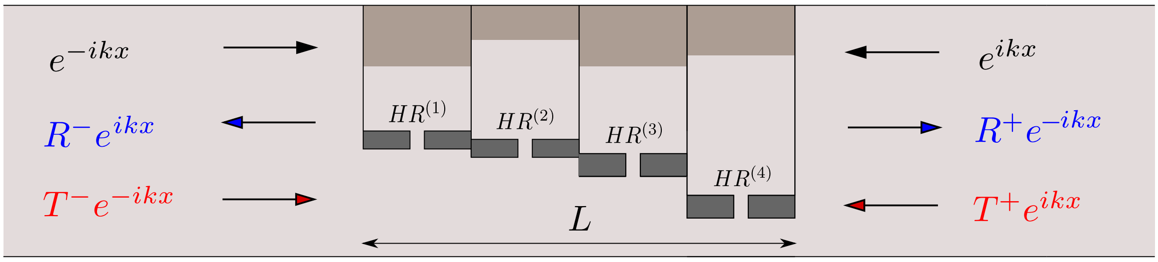

Figure 5.2: A graphic depicting a system for $M = 4$ Helmholtz resonators in a two port system.

The generalised transfer matrix for a two port perfect absorber can be expressed as

$$T = M_{\Delta l}^{(0)} \prod_{m=1}^{M} M_{WG}^{(m)} \cdot M_{HR}^{(m)} \cdot M_{WG}^{(m)} \cdot M_{\Delta l}^{(m)} \tag{5.1}$$

Where $M_{WG}^{(m)}$ is the transfer matrix for fluid layer of length $A_c/2$ and cross sectional area $S^{(m)} = A_w A^{(m)}$, $M_{HR}^{(m)}$ is the transfer matrix which introduces the m^{th} Helmholtz resonator as a point scatterer, where M is the total number of resonators in the system, and $M_{\Delta l}^{(m)}$ is the transfer matrix to account for the pressure radiation due to the discontinuity between varying cross sectional areas. This is given by [45, 85]

$$\begin{aligned} M_{\Delta l}^{(m)} &= \begin{bmatrix} 1 & \mathrm{i}\omega\rho_0 \Delta l / S^{(m+1)} \\ 0 & 1 \end{bmatrix} \quad \text{for} \quad m = \{0 \dots M-1\}, \\ M_{\Delta l}^{(M)} &= \begin{bmatrix} 1 & \mathrm{i}\omega\rho_0 \Delta l / S^{(M)} \\ 0 & 1 \end{bmatrix}, \end{aligned} \tag{5.2}$$

Where the initial length correction $\Delta l^{(0)}$ is given by [85]

$$\Delta l^{(0)} = A^{(1)} \Omega \sum_{n=1}^{\infty} \frac{\sin^2(n\pi\Omega)}{(n\pi\Omega)^3}, \tag{5.3}$$

with the initial porosity as $\Omega = S^{(1)}/S_t$. The pressure radiation at the discontinuity between each subsequent section is given by [72].

$$\begin{aligned} \Delta l^{(m)} &= 0.82 \left[1 - 1.35 \frac{A^{(m)}}{A^{(m-1)}} + 0.31 \left(\frac{A^{(m)}}{A^{(m-1)}} \right)^3 \right] A^{(m)} \quad \text{for} \quad m = \{1 \dots M-1\}, \\ \Delta l^{(M)} &= 0.82 \left[1 - 1.35 \frac{A^{(M)}}{A_t} + 0.31 \left(\frac{A^{(M)}}{A_t} \right)^3 \right] A^{(M)}. \end{aligned} \tag{5.4}$$

The impedance for a Helmholtz resonator with a porous inclusion within the cavity can be obtained with equation (2.67). It must be noted that within this chapter, the addition of a porous inclusion will not increase the depth of the cavity when in comparison to the non-porous alternative, i.e. $l_c^{(m)} + l_p^{(m)}$ is constant. The two port scattering coefficients can be determined from the final transfer matrix with the methodology set out in Section 2.6.3.

5.1.1 Results

5.1.1.1 At a Single Frequency

Within this section, results are presented highlighting how the inclusion of porous material within the cavity of a Helmholtz resonator can be used to achieve perfect absorption in a two port system. This is conducted at a single frequency with two sets of results presented to highlight the contrast between the inclusion of an optimised length of porous material. In order to achieve perfect absorption, the optimisation methodology was the method of Least Squares using the in-built MATLAB function 'lsqnonlin' with a cost function of $CF = 1-\alpha$ at a frequency of 300 Hz, with four optimisation parameters per Helmholtz resonator; r_n, l_n, l_c and l_p. The geometry for system is presented in Table 5.1, where the depth of the system is $A_w = 30$ mm.

m	r_n	l_n	A_c	l_c	$A^{(m)}$	l_p
1	2.9	14.9	30	40.3	14.8	9.0
2	3.0	15.5	30	52.5	2.0	0

Table 5.1: Geometric properties of optimised single frequency perfect absorber. All units are [mm].

To study the contrast between the inclusion of the porous layer within the first Helmholtz resonator, plots of the asymmetrical absorption and reflection coefficients, and the transmission coefficient, for the geometry presented in Table 5.1, with $l_p^{(1)} = 0$ mm, can be seen in Figure 5.3.

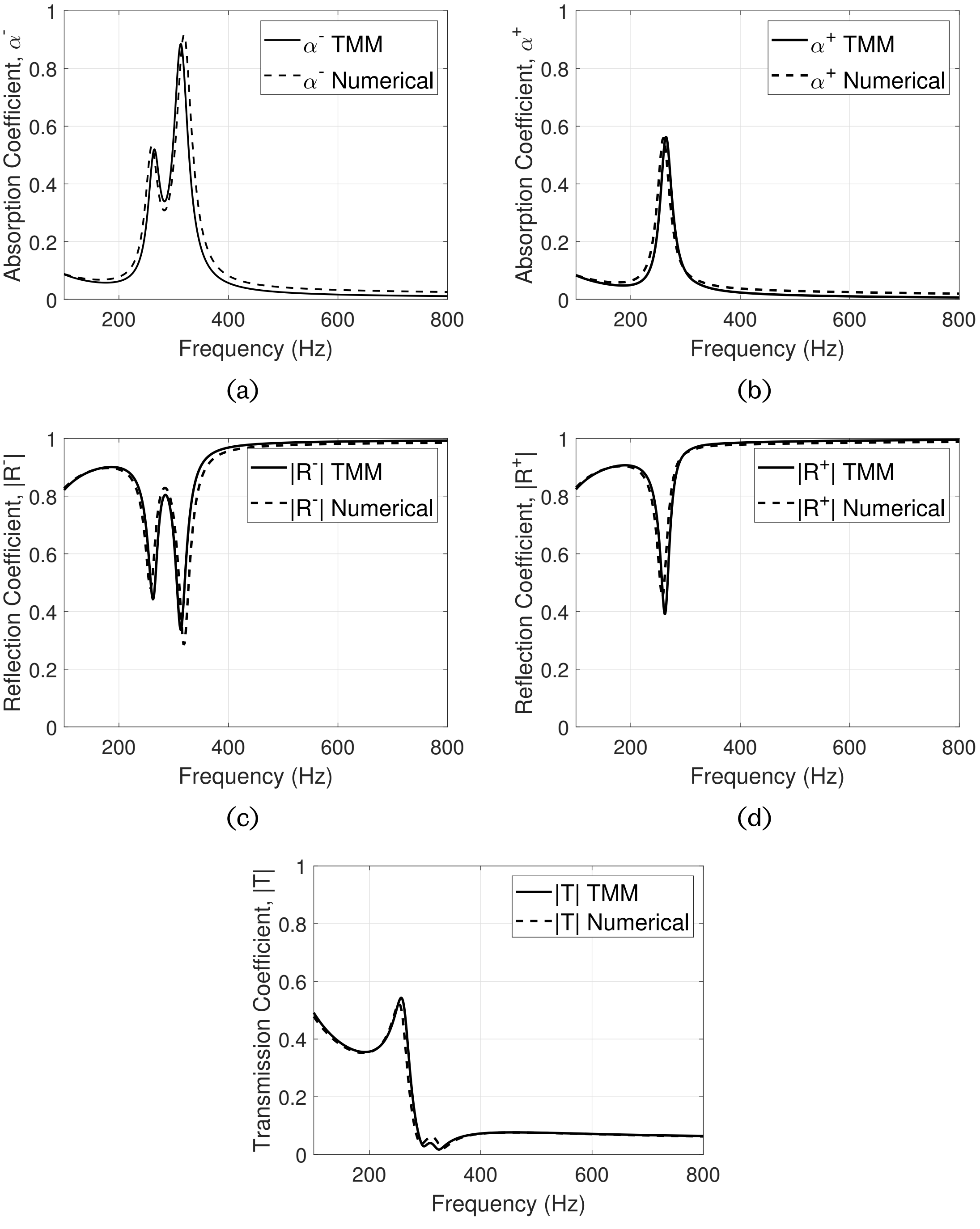

(a) (b)

(c) (d)

(e)

Figure 5.3: Plots of the absorption and reflection coefficients in the $-\mathrm{i}kx$ and $+\mathrm{i}kx$ directions, and the transmission coefficient, for the presented geometry when $l_p^{(1)} = 0$.

From this figure it is evident that the absorption properties of the system are highly asymmetrical with two absorption peaks present in the $-\mathrm{i}kx$ direction in Figure 5.3a, in contrast to the singular absorption peak in the $+\mathrm{i}kx$ direction in Figure 5.3b. This is reflected in the plots of the reflection coefficients in the negative and positive directions in Figures 5.3c and 5.3d, respectively. In both the negative and positive directions, the peaks in absorption are compensated by reductions in the reflection coefficient such that the transmission coefficient is the same for both propagative directions. This is due to the system being reciprocal, i.e. the determinant of the final transfer matrix is equal to one.

It can be seen that both resonant responses are present in the negative propagative direction due to the change in impedance being more gradual with the stepped changes in cross sectional area from the open waveguide to each subsequent Helmholtz resonator. This is in contrast to the positive propagative direction where there is a singular large change in cross sectional area by $HR^{(2)}$, this has resulted in the single resonant response by this resonator. In both directions there is near perfect reflection at frequencies above the response of $HR^{(2)}$ in the negative direction and $HR^{(1)}$ in the positive direction. The near perfect reflection is a result of the very large impedance contrast between the main waveguide section and the resulting waveguide portion from the inclusion $HR^{(2)}$. Finally, it can be seen that there is excellent agreement between the analytical and numerical models used, validating the phenomenon present here.

To see the benefit of the porous inclusion, plots of the asymmetrical absorption and reflection coefficients, and the transmission coefficient, for the geometry presented in Table 5.1, with $l_p^{(1)} = 9$ mm, can be seen in Figure 5.4.

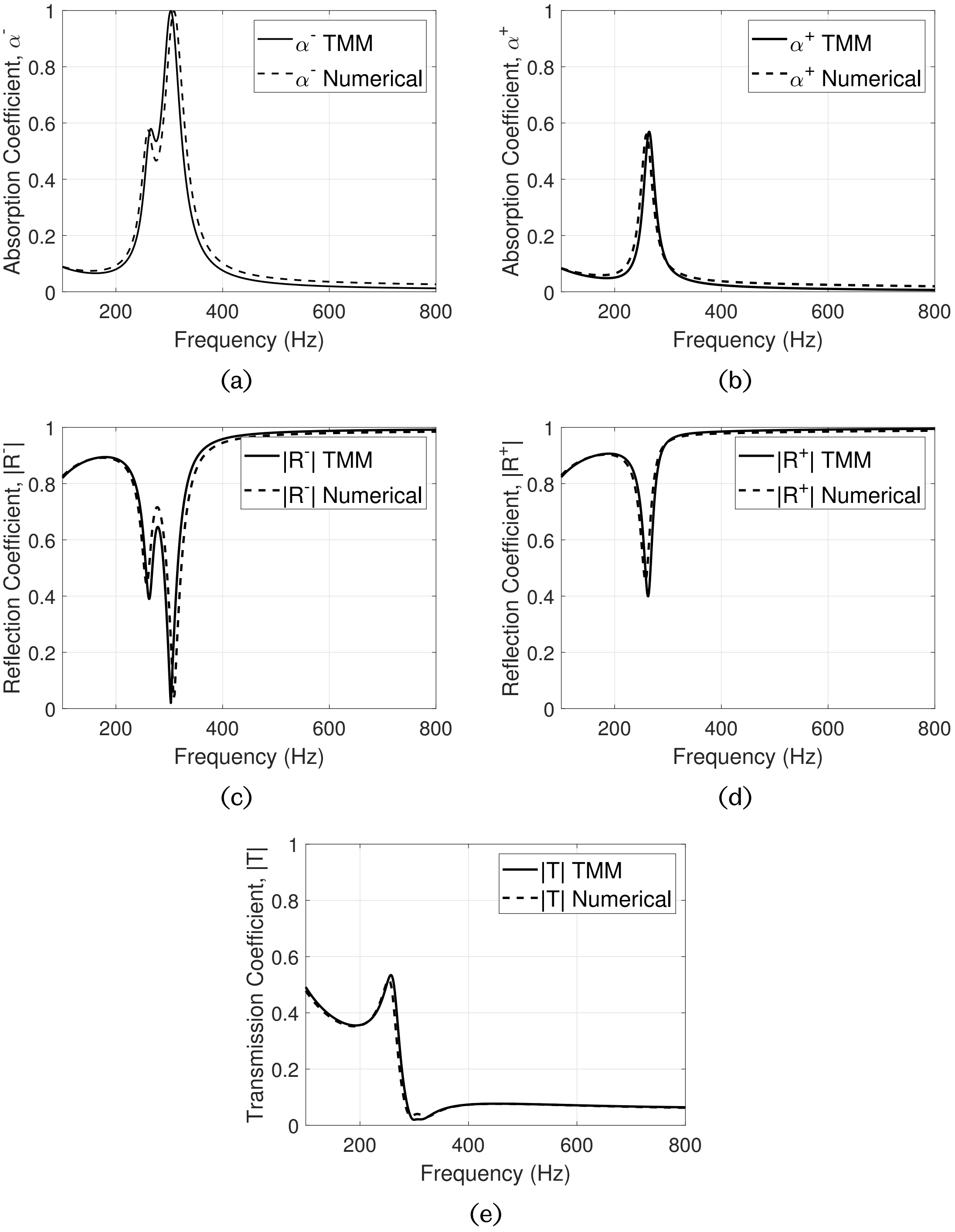

(a) (b)

(c) (d)

(e)

Figure 5.4: Plots of the absorption and reflection coefficients in the $-\mathrm{i}kx$ and $+\mathrm{i}kx$ directions, and the transmission coefficient, for the presented geometry when $l_p^{(1)} = 9$ mm.

From this figure it is evident that the addition of the porous inclusion in $HR^{(1)}$ has reduced the reflection coefficient to near zero in Figure 5.4c, such that the absorption coefficient has been increased to near unity in Figure 5.4a. This results in an impedance match and thus has critically coupled the system with the main waveguide such that perfect absorption is achieved at a frequency of approximately 300 Hz with a sample thickness of $\lambda/17$.

Additionally, the same phenomenon present in Figure 5.3 in which there is only a single resonant response in the positive propagative direction can also be seen in Figures 5.4c and 5.4d, indicating the benefit of the absorption layer is only realised in negative propagative direction for this system. There is little difference between the transmission coefficients for both systems.

To help further understand the physical mechanism behind the critical coupling condition attained by the inclusion of the porous layer, complex frequency plane plots based upon the eigenvalues and eigenvectors of the scattering matrices for each system are examined. To illustrate, if the total acoustic pressure either side of the structure is given by

$$\begin{aligned} p(x_1) &= A\mathrm{e}^{-\mathrm{i}kx_1} + B\mathrm{e}^{\mathrm{i}kx_1} \quad \text{for} \quad x_1 > 0, \\ p(x_2) &= C\mathrm{e}^{-\mathrm{i}kx_2} + D\mathrm{e}^{\mathrm{i}kx_2} \quad \text{for} \quad x_2 < -L, \end{aligned} \tag{5.5}$$

the relationship between the amplitudes is given by the scattering matrix, **S** [31],

$$\begin{bmatrix} A \\ D \end{bmatrix} = \mathbf{S} \begin{bmatrix} C \\ B \end{bmatrix} = \begin{bmatrix} T & R^+ \\ R^- & T \end{bmatrix}. \tag{5.6}$$

From the scattering matrix, two eigenvalues can be obtained

$$\lambda_{1,2} = T \pm \sqrt{R^+R^-}, \tag{5.7}$$

which have the corresponding eigenvectors,

$$\nu_1 = [R^+, \sqrt{R^+R^-}], \quad \nu_2 = [-\sqrt{R^+R^-}, R^-]. \tag{5.8}$$

Plots of the eigenvalues and eigenvectors for the single frequency absorber when $l_p = 0$ mm can be seen in Figure 5.5.

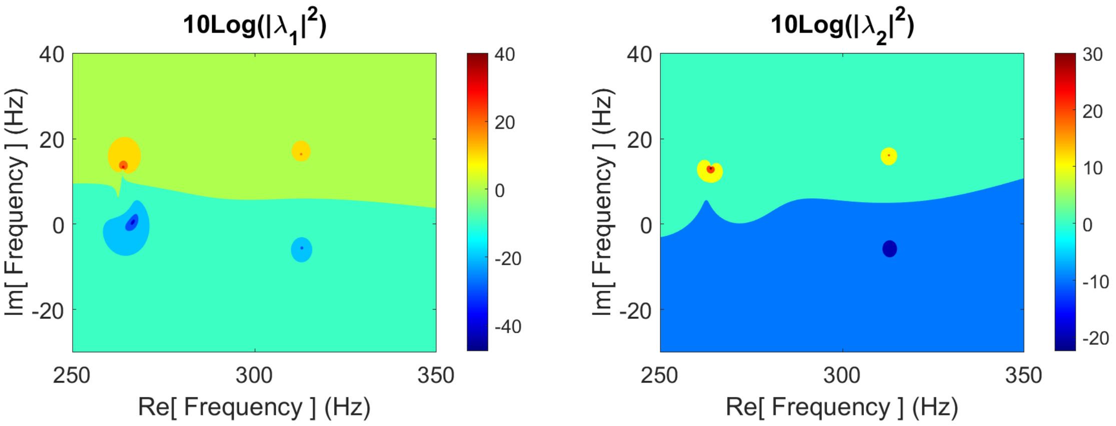

(a) $10\log(|\lambda_1|^2)$ (b) $10\log(|\lambda_2|^2)$

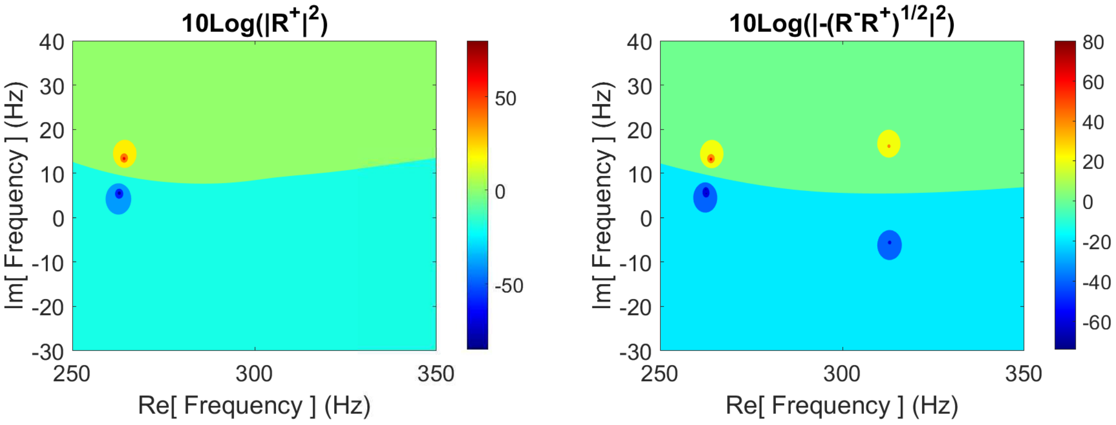

(c) $10\log(|\nu_1(1)|^2)$ (d) $10\log(|\nu_2(1)|^2)$

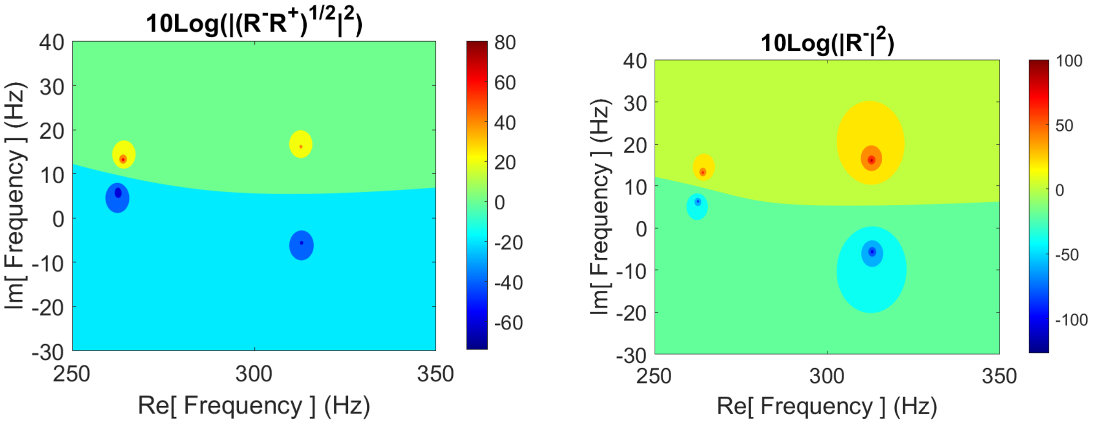

(e) $10\log(|\nu_1(2)|^2)$ (f) $10\log(|\nu_2(2)|^2)$

Figure 5.5: Plots of the eigenvalues and eigenvectors of the scattering matrix for the single frequency absorber when $l_p = 0$ mm.

From this figure it can be seen in the plot of λ_1 in Figure 5.5a, both pairs of poles and zeros are present for each resonator, whereas in the plot of λ_2 in Figure 5.5b, only one pair of poles and zeros is present for $HR^{(1)}$, with just the pole for $HR^{(2)}$ present. In each case the pole indicates a resonance within the system. There is no zero for $HR^{(1)}$ in the plot of λ_2 due to $HR^{(1)}$ not being excited in the $+\mathrm{i}kx$ direction. In both plots of the eigenvalues, the complex value of the zeros are negative indicating that the critical coupling condition has not been fulfilled within this system.

Upon examination of $\nu_1(1)$ in Figure 5.5c, only a single pole and zero is present, which is for $HR^{(2)}$. Again this is due to $HR^{(1)}$ not being excited by an incident acoustic wave in $+\mathrm{i}kx$ direction. Due to the complex value of the zero being greater than zero, the introduction of losses within this resonator would shift the zero further from the real frequency axis and thus reduce the impedance matching. Upon examination of $\nu_2(2)$ in Figure 5.5f both poles and zeros are present. Again the low frequency zero of $HR^{(2)}$ is greater than zero, indicating the introduction of lossy material will simply increase the impedance mismatch. This is in contrast to the high frequency zero of $HR^{(2)}$ which has a negative imaginary component, indicating the introduction of porous media within the cavity of the Helmholtz resonator could reduce the impedance mismatch such that $|R^{-}| = 0$. These observations can also be made from plots of $\nu_2(1)$ and $\nu_1(2)$ in Figures 5.5d and 5.5e, respectively. These plots are identical due to the absolute value of the eigenvectors being use within the scale.

Plots of the eigenvalues and eigenvectors of the scattering matrix for the perfect absorber, where $l_p^{(1)} = 9$ mm, can be seen in Figure 5.6. From the plots of the eigenvalues in Figures 5.6a and 5.6b it can be seen that the zero of the higher frequency resonator, $HR^{(1)}$ has been translated to sit on the real frequency axis, at a lower real frequency value, indicating that $T = \sqrt{R^{+}R^{-}} \approx 0$ and near perfect absorption has been achieved at approximately 300 Hz. To determine which propagative direction has perfect absorption, it is necessary to look at the eigenvector plots of $\nu_1(1)$ and $\nu_2(2)$ in Figures 5.6c and 5.6f, respectively. Upon examination of these figures it is evident the critically coupled zero is present in the eigenvector $\nu_2(2)$, indicating perfect absorption has be achieved in the $-\mathrm{i}kx$ direction.

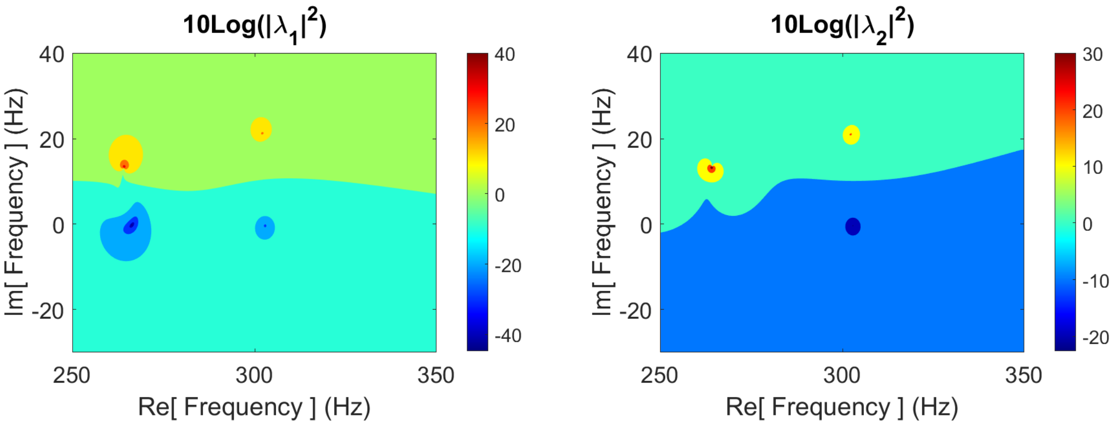

(a) $10\log(|\lambda_1|^2)$ (b) $10\log(|\lambda_2|^2)$

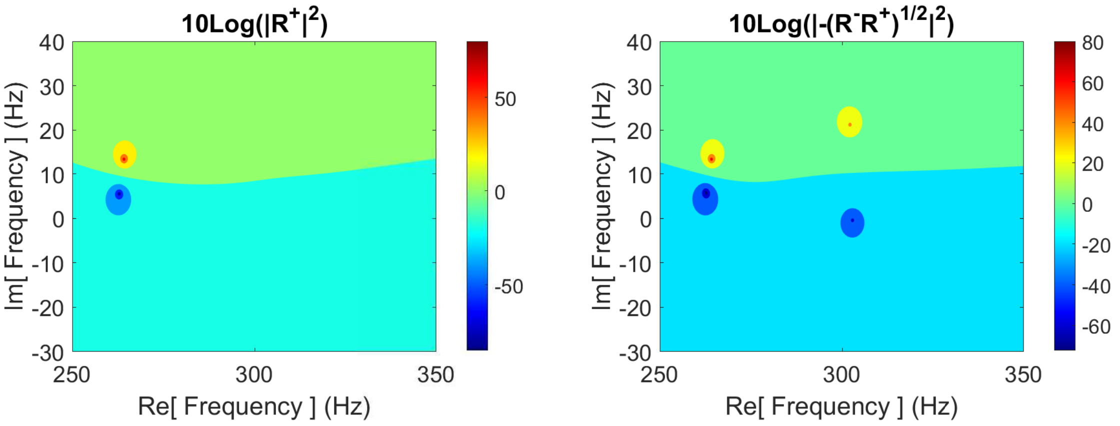

(c) $10\log(|\nu_1(1)|^2)$ (d) $10\log(|\nu_2(1)|^2)$

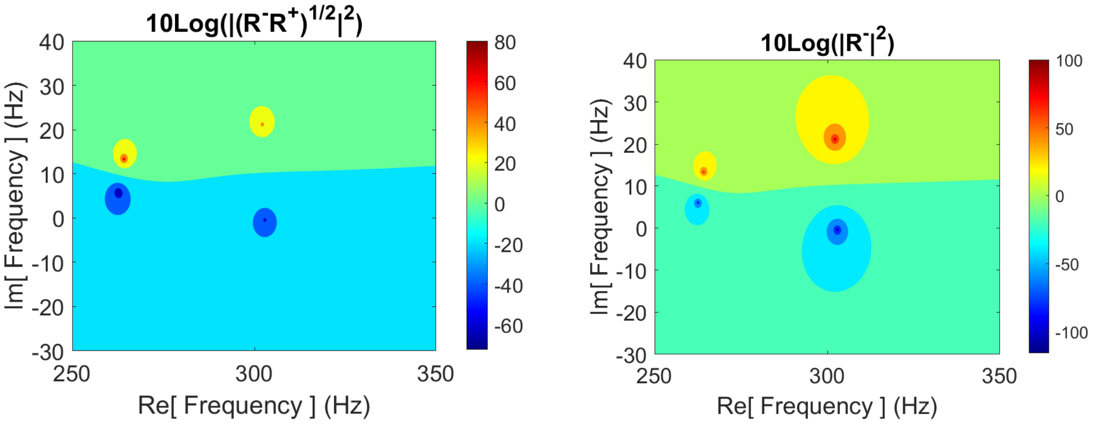

(e) $10\log(|\nu_1(2)|^2)$ (f) $10\log(|\nu_2(2)|^2)$

Figure 5.6: Plots of the eigenvalues and eigenvectors of the scattering matrix for the single frequency perfect absorber when $l_p = 9$ mm.

5.1.1.2 Broadband Frequency Range

Within this section, results are presented for the two port broadband perfect absorber which builds upon the phenomenon described for a single resonator perfect absorber. Here, the system consists of four Helmholtz resonators of differing resonant frequencies. Results are presented highlighting the difference between the inclusion of porous material of an optimised length within the cavity of each resonator and without a porous inclusion within each resonator cavity. To achieve an optimised geometry, the Least Squares method of optimisation was again used by utilising the in-built MATLAB function 'lsqnonlin'. It must be noted this selected optimisation methodology is not as effective for two port systems in comparison to one port systems.

Due to the large number of parameters and the general insensitivity of the cost function, an iterative design process was utilised to obtain the final optimised system geometry. This iterative process was undertaken by first achieving perfect absorption with the two lowest frequency resonators using the cost function $CF = 1 - \alpha$. These optimised resonators provide a large enough impedance contrast such that they behave almost as rigid backing and allow each subsequent resonator to be perfectly coupled with the waveguide. This was done iteratively, again with the cost function $CF = 1 - \alpha$ for each subsequent resonator. Finally, the following cost function was utilised to maximise the absorption coefficient within the desired frequency range and to account for any changes in the absorption coefficient due to additional coupling of resonators in the final complete system.

$$CF = (f_1 - f_0) - \int_{f_0}^{f_1} \alpha \, df, \tag{5.9}$$

where f_1 and f_0 are the upper and lower bounds of the desired frequency range, respectively. For the bounds $[300, 600]$ Hz, an optimised geometry was obtained and can be seen in Table 5.2. An additional wall thickness of 2 mm is incorporated within the geometry such that the walls have a finite thickness if desired. The total length of the system is $L = 13.6$ cm.

m	r_n	l_n	A_c	l_c	$A^{(m)}$	l_p
1	7.4	10	30	60	40	25
2	6.4	16	30	63	31	27
3	5.0	20	30	67	23	27
4	5.0	25	30	80	5.0	15

Table 5.2: Geometric properties of the two port broadband perfect absorber Helmholtz resonator system. All units are [mm].

Plots of the scattering coefficients for the geometry presented in Table 5.2 but no porous inclusions can be seen in Figure 5.7.

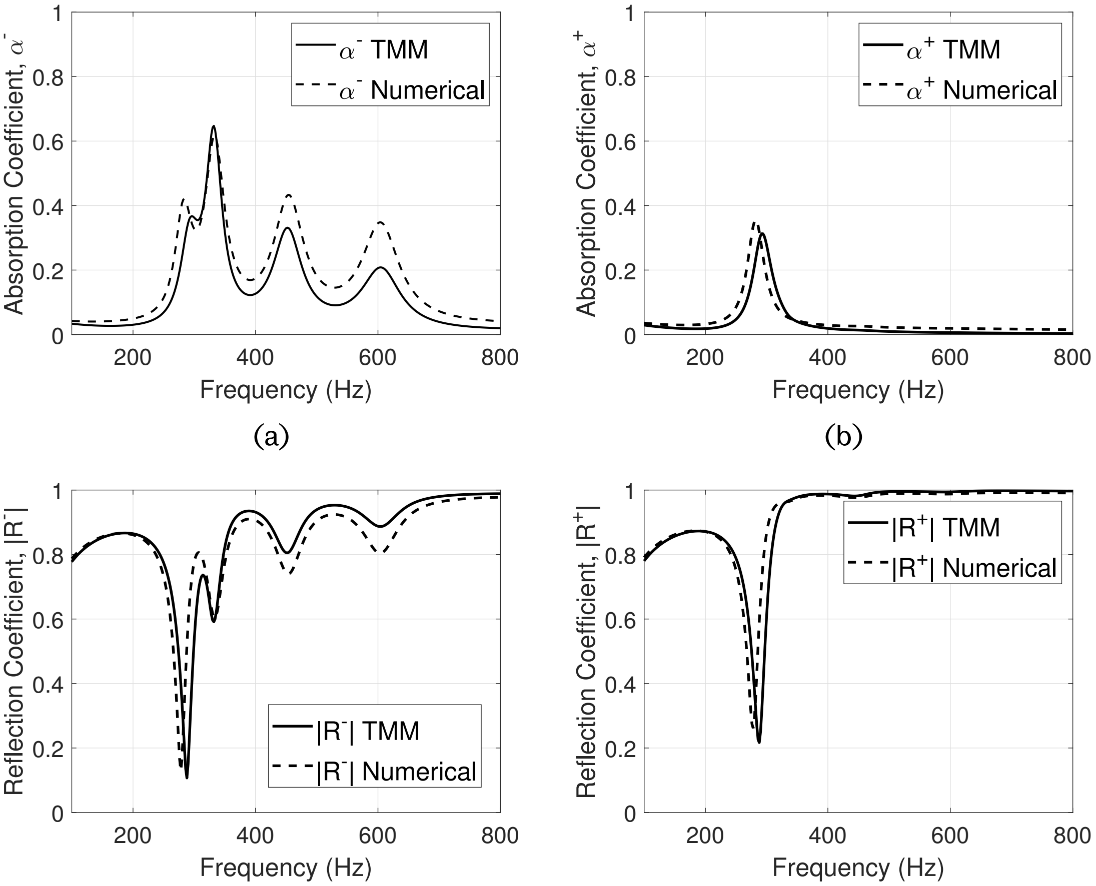

(a) (b)

(c) $10\log(|\lambda_2|^2)$ (d)

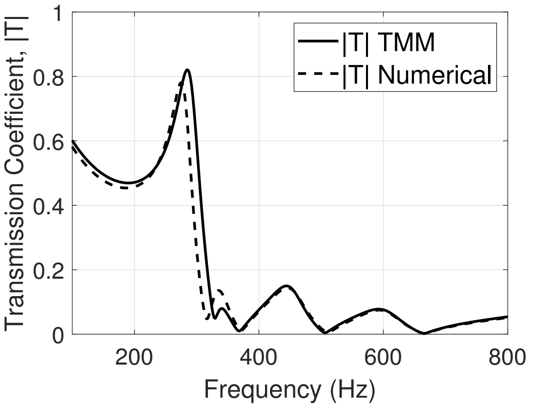

(e)

Figure 5.7: Plots of the absorption and reflection coefficients in the $-\mathrm{i}kx$ and $+\mathrm{i}kx$ directions, and the transmission coefficient, for the presented geometry of the broadband absorber but with no porous inclusions.

From this figure it can be seen that there is good agreement between the analytical and numerical plots, with the same phenomenon presented for the single frequency absorber also present here; namely the high asymmetry in the reflection and absorption coefficients. Again, it is evident that each resonance is excited effectively with impinging wave propagation in the $-\mathrm{i}kx$ direction, whereas only a single resonant response is present in the $+\mathrm{i}kx$ direction.

To illustrate the benefit of the inclusion of the optimised length of porous media within the cavities of the Helmholtz resonators, plots of the scattering coefficients can be seen in Figure 5.8. From this figure it can be seen that the inclusion of porous media has improved the absorption of the first three Helmholtz resonators to near unity in the $-\mathrm{i}kx$ direction. It can be seen that the mechanism for achieving this perfect absorption is present in the plots of $|R^{-}|$ in Figure 5.8c, where the reflection coefficient is reduced to near zero at each resonant frequency of the system. Again, the reflection and absorption coefficients display a large amount of asymmetry between impinging wave propagation directions. Here perfect absorption has been achieved over a broadband frequency range, with the lowest frequency perfectly absorbed being 312 Hz. This results in a system with a sample thickness of $\lambda/8$ at this frequency.

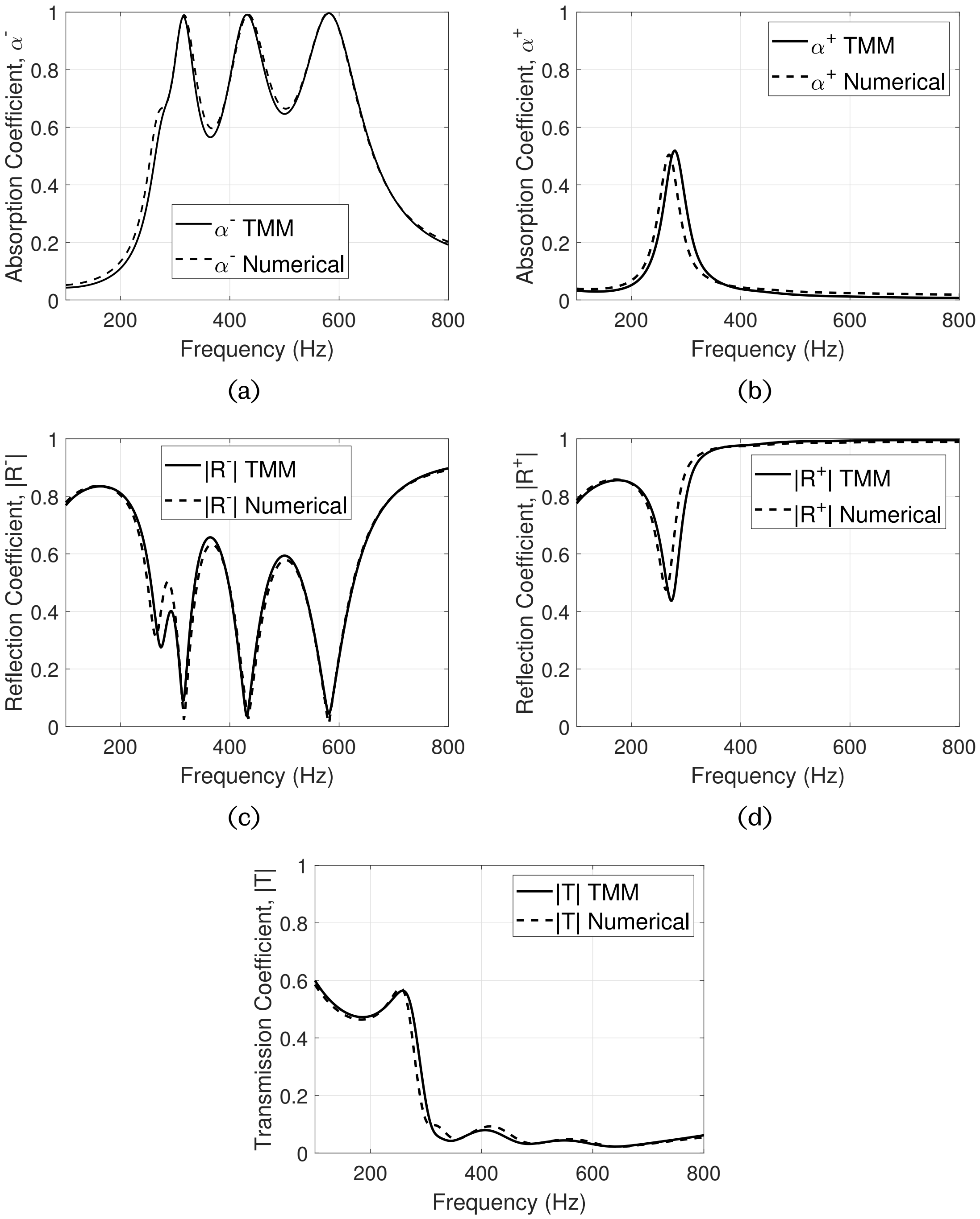

(a) (b)

(c) (d)

(e)

Figure 5.8: Plots of the absorption and reflection coefficients in the $-\mathrm{i}kx$ and $+\mathrm{i}kx$ directions, and the transmission coefficient, for the presented geometry of the broadband perfect absorber with porous inclusions.

To further illustrate the coupling phenomenon between the Helmholtz resonators, graphics of the numerically obtained acoustic pressure at each of the frequencies perfect absorption is achieved can be seen in Figure 5.9.

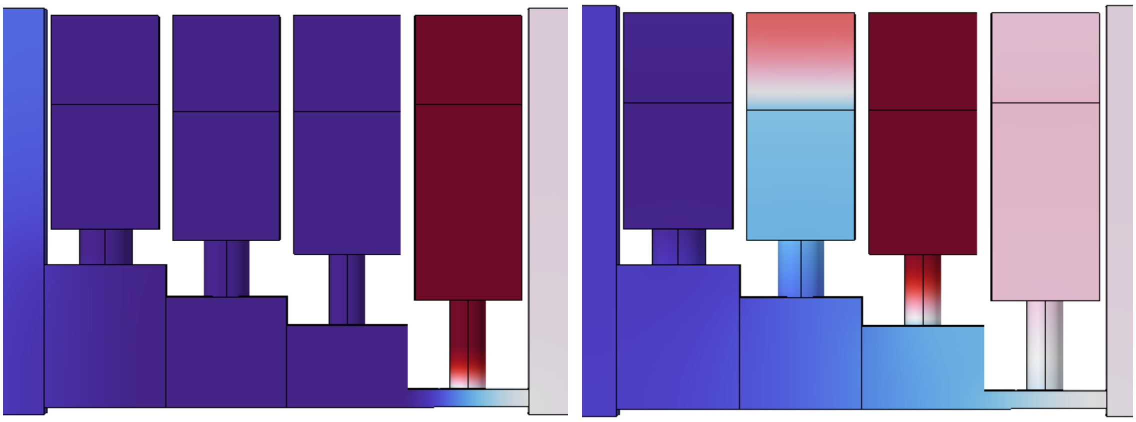

(a) 312 Hz (b) 426 Hz

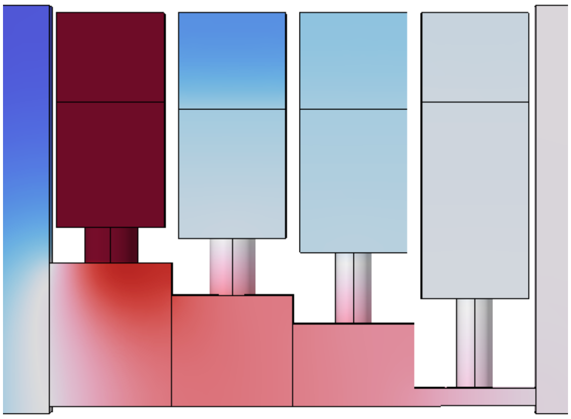

(c) 576 Hz

Figure 5.9: Pressure amplitude of the broadband perfect absorber at the three absorption peaks of 312 Hz, 426 Hz and 576 Hz. Red indicates positive pressure and blue indicates negative pressure. $HR^{(1)}$ is the first resonator from the left and $HR^{(4)}$ is the first from the right.

From this graphic it can be seen that at the lowest frequency in which perfect absorption is achieved, 312 Hz, the first three Helmholtz resonators are in phase, with the lowest frequency resonator $HR^{(4)}$ out of phase. Since the perfect absorption at this frequency is achieved by $HR^{(3)}$, it can be deduced that the strong response from $HR^{(4)}$ is to enable the soft boundary condition in the $+\mathrm{i}kx$ such that $|R^{+}| = 1$, allowing perfect absorption to be achieved in the $-\mathrm{i}kx$ direction. At 426 Hz, where perfect absorption is achieved by $HR^{(2)}$, it can be seen that there is strong coupling between $HR^{(2)}$ and $HR^{(3)}$. The influence of the porous inclusion is also evident in $HR^{(2)}$, shown by the large pressure gradient within the porous layer. At 576 Hz it is evident perfect absorption is primarily achieved by $HR^{(1)}$ due to the comparatively minimal response by the remaining resonators. At this frequency the pressure radiation occurring at the discontinuity between the main waveguide and the first section can also be seen.

Finally, complex frequency plane plots of the eigenvalues and eigenvectors for the system with no porous inclusions are presented in Figure 5.10. From the plots of the eigenvalues in Figures 5.10a and 5.10b, it can be seen there are four poles, one for each resonance, with an accompanying four zeros for λ_1, and three for λ_2. All have a negative imaginary components which indicates that the use of porous media can be used to translate their position to the real frequency axis. As there is only three zeros present in the plot of λ_2, it can be determined that the maximum possible number of critically coupled Helmholtz resonators in a system of this configuration will be $M-1$, due to there being no zero which can be tuned for the lowest frequency resonator.

Again when examining the eigenvectors for the system, the high asymmetry in the reflection coefficient is evident in the comparison of $\nu_1(1)$ and $\nu_2(2)$, in Figures 5.10c and 5.10f, respectively. In Figure 5.10f it can be seen that each zero has a negative imaginary component, indicating that each can be tuned to the real frequency axis by the addition of porous media within the resonator cavities.

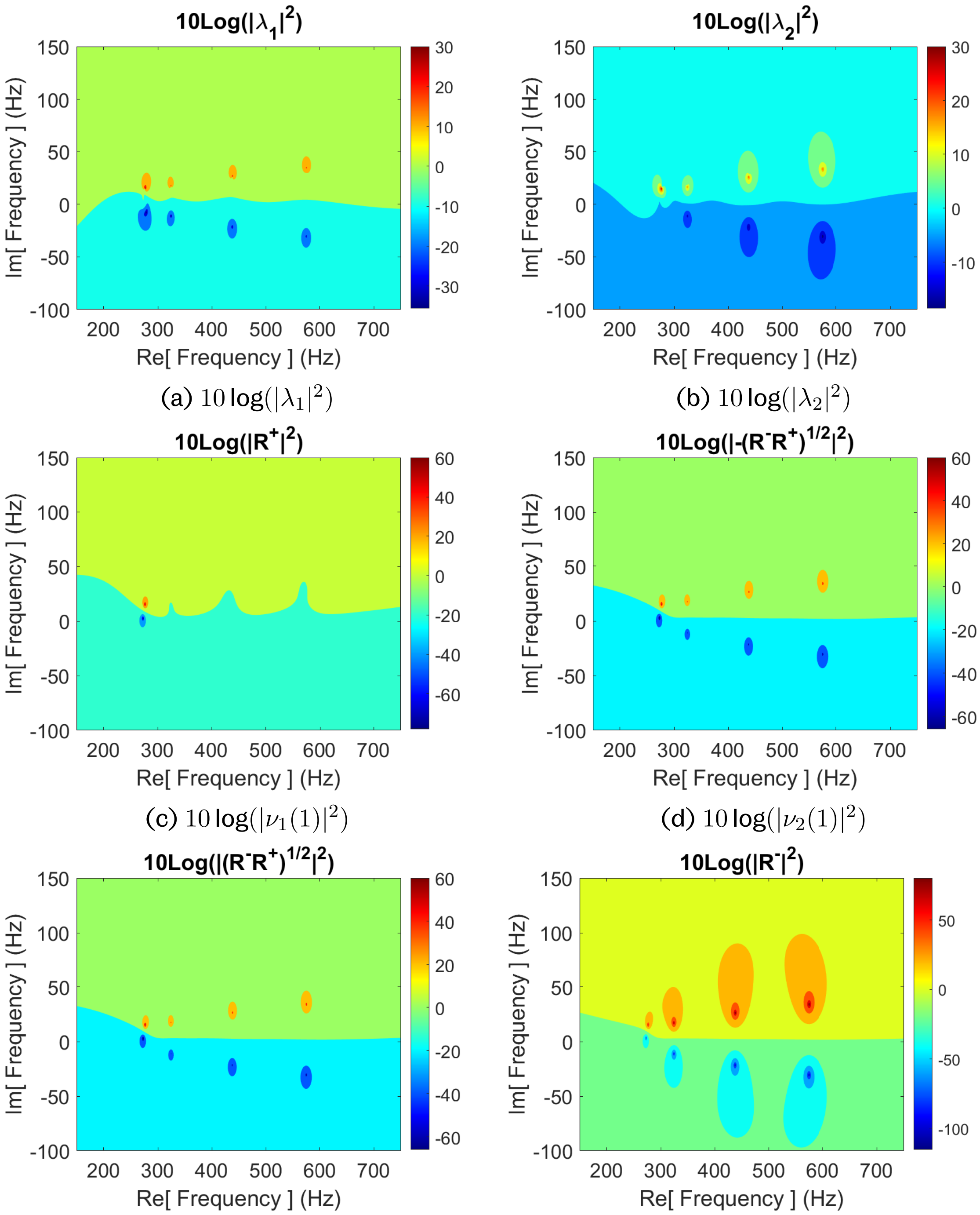

(a) $10\log(|\lambda_1|^2)$ (b) $10\log(|\lambda_2|^2)$

(c) $10\log(|\nu_1(1)|^2)$ (d) $10\log(|\nu_2(1)|^2)$

(e) $10\log(|\nu_1(2)|^2)$ (f) $10\log(|\nu_2(2)|^2)$

Figure 5.10: Plots of the eigenvalues and eigenvectors of the scattering matrix for the broadband absorber with no porous inclusions.

To help quantify the benefit of the porous inclusions in achieving perfect absorption, plots of the eigenvalues and eigenvectors of the broadband perfect absorber with porous inclusions can be seen in Figure 5.11.

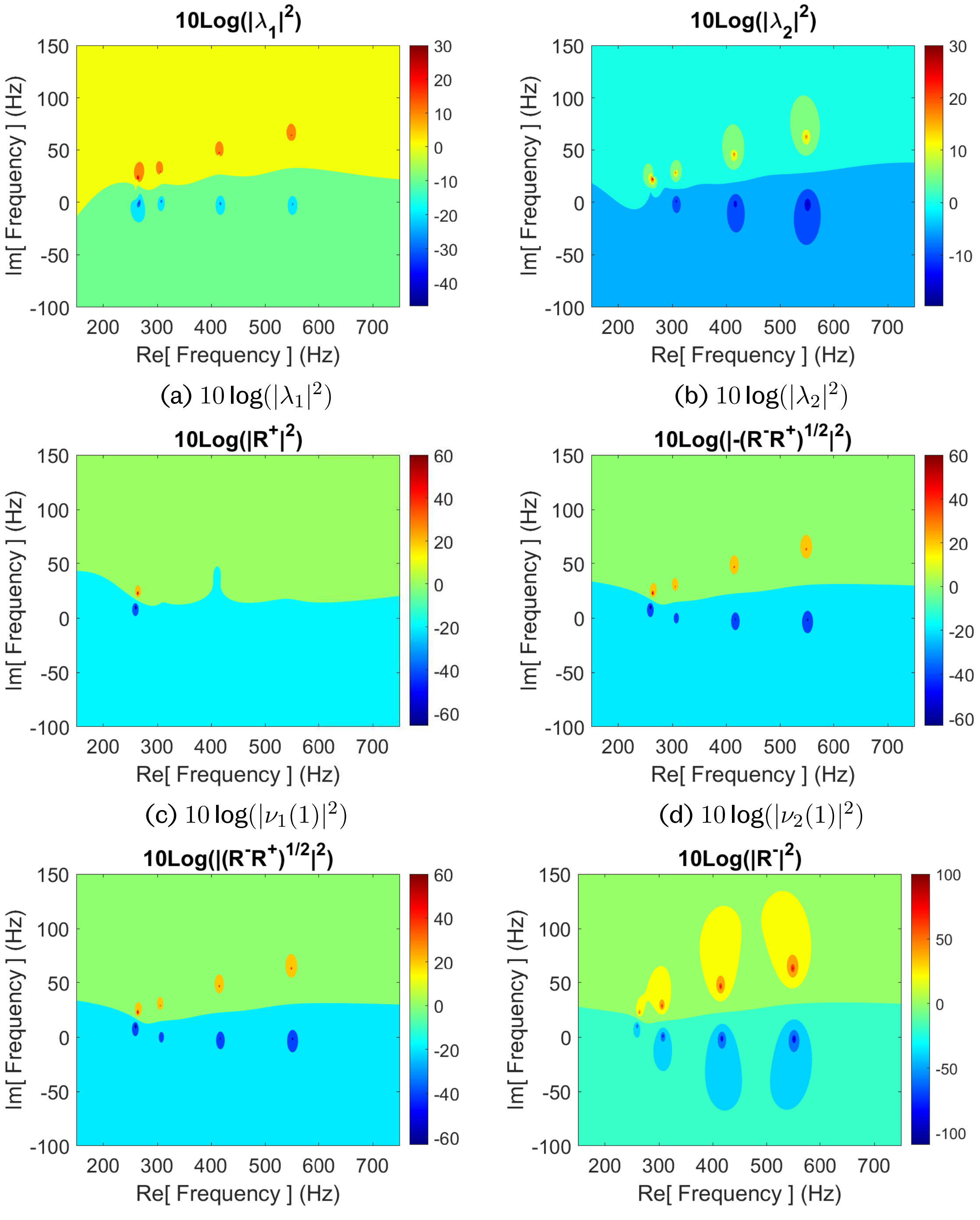

(a) $10\log(|\lambda_1|^2)$ (b) $10\log(|\lambda_2|^2)$

(c) $10\log(|\nu_1(1)|^2)$ (d) $10\log(|\nu_2(1)|^2)$

(e) $10\log(|\nu_1(2)|^2)$ (f) $10\log(|\nu_2(2)|^2)$

Figure 5.11: Plots of the eigenvalues and eigenvectors of the scattering matrix for the broadband absorber with porous inclusions.

From this figure it can be seen that the zeros of the eigenvalues λ_1 and λ_2, in Figures

5.11a and 5.11b, have been translated to the real frequency axis such that perfect absorption has been achieved, with a slight down-shift in the resonant frequencies. In comparison of $\nu_1(1)$ with $\nu_2(2)$ in Figures 5.11c and 5.11f, respectively, it is evident that perfect absorption is achieved in the $-\mathrm{i}kx$ direction, with only one resonant response visible in the $+\mathrm{i}kx$ direction. The fulfilment of the critical coupling condition is also evident in plots of $\nu_2(1)$ and $\nu_1(2)$ in Figures 5.11d and 5.11e, respectively.

5.2 Chapter Conclusion

Within this chapter, the mechanism to achieve asymmetrical perfect absorption in two port systems has been explored. Here, systems of coupled Helmholtz resonators have been optimised by the inclusion of porous media within the cavity such that the critical coupling condition is fulfilled and thus perfect absorption is obtained. This was undertaken at a single frequency of approximately 300 Hz through the use of two coupled Helmholtz resonators with a porous inclusion in the higher frequency resonator. The configuration of the geometry is such that at the critical frequency, impinging waves from one direction are perfectly absorbed, whilst waves impinging in the opposite direction are perfectly reflected. This was illustrated through the plotting of the eigenvalues and eigenvectors of the scattering coefficients in the complex frequency plane. The optimised geometry presented in with this chapter has a sample thickness of $\lambda/16$.

This methodology was then extended to a broadband system in the frequency range of 300 Hz to 600 Hz. This utilised four coupled Helmholtz resonators. The utility of the porous inclusions was displayed by contrasting the system with and without the porous inclusions, highlighting the stark contrast in absorptive performance. Due to required coupling of the two lowest frequency resonators, it was shown through the use of the complex frequency plane plots of the eigenvectors that a system of this geometry can only exhibit $M-1$ critically coupled frequencies. The resulting broadband perfect absorber presented within this chapter exhibited perfect absorption at $312, 426$ and 576 Hz, with a sample thickness of $\lambda/8$ at the lowest critically coupled frequency.

Chapter 6

Approximation of Impedance of Identical Coupled Helmholtz Resonators

A common methodology in the simplification of analytical models for low frequency resonant structures is that of the low frequency approximation. This allows for simple approximate expressions to be obtained that describe the effective fluid properties of systems. This is typically done by taking the low frequency, $kL \ll 1$, such that the analytical models can be simplified so that the equations for the effective fluid properties can be obtained, as in [84, 17, 15], for example.

Also, it has been shown that by constructing serial arrays of Helmholtz resonators, strong coupling and is observed allowing for attenuation at multiple distinct frequencies, dependant on the number of resonators in the series [88]. These systems can be modelled with a lumped parameter approach [89, 90, 91, 92], or using the TMM to obtain the acoustic properties of the system [93].

Within this chapter, an alternative simplification methodology is presented that is based upon the asymptotic approximation of the full transfer matrix for the system derived using the TMM. This is applied to the impedance expressions for one port systems composed of M identical coupled Helmholtz resonators in series. The geometry is such that the neck of each subsequent Helmholtz resonator is directly interfaced with the cavity of the preceding Helmholtz resonator, resulting in a highly coupled and mutli-resonant structure. By undertaking this asymptotic approximation, the characteristic impedances for these systems of M coupled identical Helmholtz resonators are polynomials of the same order as the number of Helmholtz resonators within the system. Solving these polynomials provides an analytical methodology to determining the resonant frequency of one port coupled Helmholtz resonators.

This chapter is set out as follows; first an array of M identical Helmholtz resonators coupled in series are modelled using the transfer matrix method. A method of simplification is then applied to the impedance term obtained using the TMM. This method of simplification utilises the large impedance contrast that exists between the neck and cavity of a Helmholtz resonator. Analytical and numerical verification is then undertaken to assess the validity of the approximation. Comments on the effectiveness of the modelled system for low frequency absorption are also made. Finally, further analytical analysis is undertaken to explore other useful aspects to the derived polynomials, such as a simplified expression for the impedance of a Helmholtz resonator and the approximation of the resonant frequencies of the systems from the solution to the derived polynomials.

6.1 Theory

Consider an array of coupled identical cylindrical Helmholtz resonators, as depicted in Figure 6.1. Here S_w is the waveguide cross sectional area, S_n is the neck cross sectional area, S_c is the cavity cross sectional area, l_n is the neck length and l_c is the cavity length.

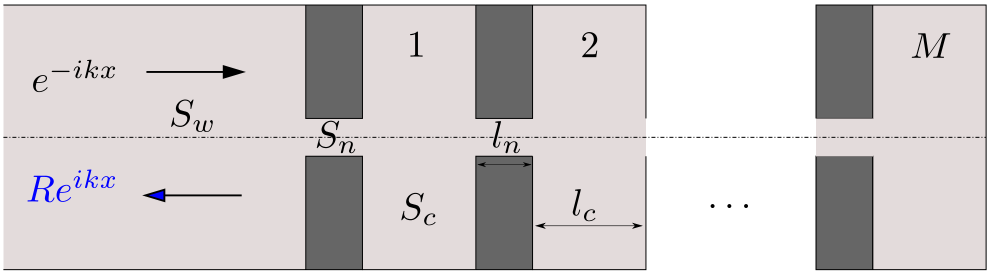

Figure 6.1: Graphic depicting a serial array of M coupled identical cylindrical Helmholtz resonators.

To calculate the impedance of this system, the transfer matrix method is used. The full matrix, T, can be derived from the following expression:

$$T = \prod_{m=1}^{M} M_n M_{\Delta l} M_c. \tag{6.1}$$

where m denotes the Helmholtz resonator, up to M. Here M_n and M_c are the transfer matrices for a fluid layer within the neck and cavity, respectively, and $M_{\Delta l}$ is the transfer matrix to capture the pressure discontinuity from the neck to the waveguide and cavity, which in this instance is expressed as

$$M_{\Delta l} = \begin{bmatrix} 1 & \mathrm{i} Z_n k_n \Delta l \\ 0 & 1 \end{bmatrix}. \tag{6.2}$$

Where Δl is arrived at from the addition of two correction lengths, $\Delta l = \Delta l_1 + \Delta l_2$. Δl_1 is due to pressure radiation at the discontinuity from the neck to the cavity of the HR [71] and Δl_2 comes from the pressure radiation at the discontinuity from the neck to the surrounding medium [72].

$$\Delta l_1 = 0.82\left[1 - 1.35\frac{r_n}{r_c} + 0.31\left(\frac{r_n}{r_c}\right)^3\right] r_n. \tag{6.3}$$

and

$$\Delta l_2 = 0.6 r_n. \tag{6.4}$$

The expression for the radiation impedance in equation 6.2 is different to that expressed in Section 2.6.5, as typically lossless impedance and wavenumber values in the radiation impedance result in marginally more accurate results when in comparison to numerically produced results. Although in this instance, this slight discrepancy is deemed appropriate to approximate the impedance of the system. This is due to the need to simplify the overall impedance terms to allow for the collection of like terms.

The surface impedance of the system of M identical coupled Helmholtz resonators can be derived from the full transfer matrix of the system as

$$Z_{(m)HR} = \frac{P_{x=0}}{v_{x=o}} = \frac{T_{11}}{T_{21}}. \tag{6.5}$$

The resulting expression of which can be deemed unwieldy for use beyond the single resonator system, expressed in equation 2.66, with further increases in the number of resonators exponentially increasing the number of terms within the impedance expression.

To simplify the impedance expressions obtained via the TMM for arrays of coupled identical Helmholtz resonators, a method of asymptotic approximation is used. The premise being the utilisation of the impedance contrast between the neck, Z_n, and cavity, Z_c, facilitated by the large contrast in cross sectional area which allows for a small order term to be obtained. This small order term, ϵ, is defined as

$$\epsilon = \sqrt{\frac{Z_c}{Z_n}}. \tag{6.6}$$

The rest of the terms can be rendered dimensionless with the following expressions:

$$\begin{aligned} c &= \frac{k_c l_c}{\epsilon}, \\ n &= \frac{k_n l_n}{\epsilon}, \\ \phi &= 1 + \frac{\Delta l}{l_n}. \end{aligned} \tag{6.7}$$

For simplification purposes a new term, x, is defined as $x = cn\phi$. This explicitly becomes

$$x = \frac{\omega^2 V_c l_n' \rho_n(\omega)}{S_n K_c(\omega)}. \tag{6.8}$$

Here, V_c is the cavity volume, l_n' is the length of the neck plus the correction terms, $\rho_n(\omega)$ is the dynamic density of air within the neck and $K_c(\omega)$ is the bulk modulus of air within the cavity.

By undertaking the full analytical matrix expansion of the final dimensionless transfer matrix, up to $M = 3$, a Taylor series expansion of the impedance can be undertaken about $\epsilon = 0$. This process was undertaken in Maple which is a symbolic and numeric computing software. From the Taylor series expansion, the following impedance expressions are obtained from the leading order terms. The subscript number denotes the number of identical Helmholtz resonators within the system.

$$\begin{aligned} Z_{1HR} &= \frac{\mathrm{i} K_c(\omega)(x-1)}{\omega V_c}, \\ Z_{2HR} &= \frac{\mathrm{i} K_c(\omega)(x^2-3x+1)}{\omega V_c (x-2)}, \\ Z_{3HR} &= \frac{\mathrm{i} K_c(\omega)(x^3-5x+6x-1)}{\omega V_c (x^2-4x+3)}. \end{aligned} \tag{6.9}$$

From these expressions it is evident that by increasing M, you increase the order of the polynomial composed of x terms, with the numerator polynomial being of the same order as M, and the denominator being of the order $M - 1$.

The impedance expression for a single HR can be further simplified and expressed as

$$Z_{1HR} = \mathrm{i}\left(\frac{\omega l_n' \rho_n(\omega)}{S_n} - \frac{K_c(\omega)}{\omega V_c}\right). \tag{6.10}$$

From the configuration of the effective property expressions of the fluid within the neck and cavity, it is evident viscous effects dominate within the neck and thermal effects dominate in the cavity.

6.2 Results

To assess the validity of the derived approximations for the surface impedance of an array of coupled identical cylindrical Helmholtz resonators, the absorption coefficients obtained with these approximate expressions, the TMM with both a lossy radiation impedance, as in the approximation, and a lossless radiation impedance. These results are compared with results computed numerically using COMSOL Multiphysics 5.9. The geometry of modelled Helmholtz resonator can be found in the Table 6.1 and has been chosen based upon achieving the critical coupling condition with the single resonator system using the derived approximation expression for the surface impedance of the system.

r_w	r_n	r_c	l_n	l_c
30	2	30	12	30

Table 6.1: Geometric properties of the serial array of HRs. All units are [mm].

A plot of the resulting absorption coefficients can be seen in Figure 6.2, where the single Hemholtz resonator system is presented in Figure 6.2a, the two resonator system in Figure 6.2b and the three resonator system in Figure 6.2c.

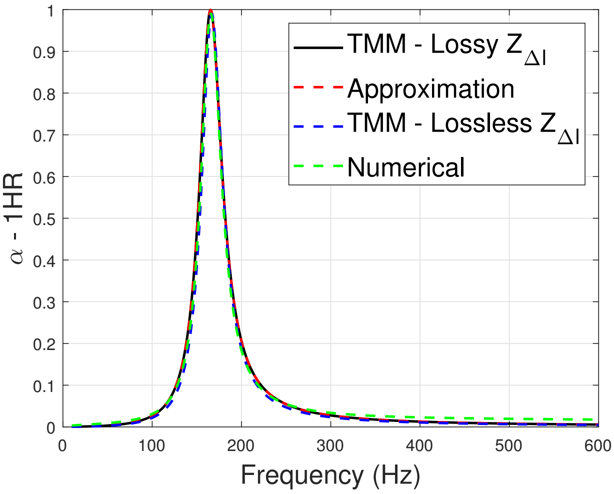

(a) Single Helmholtz resonator system.

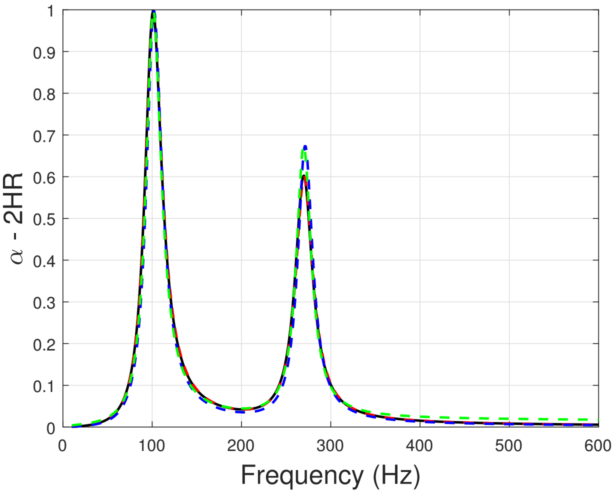

(b) Two Helmholtz resonator system.

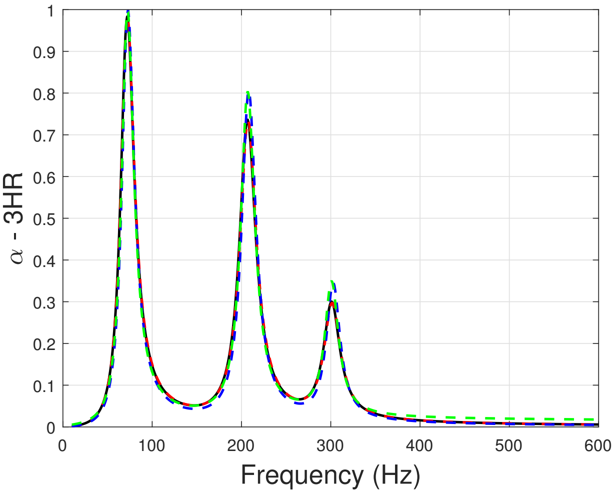

(c) Three Helmholtz resonator system

Figure 6.2: Plots of the absorption coefficient for a serial array of coupled identical Helmholtz resonators, up to $M = 3$. Results are obtained with the TMM assuming a lossy radiation impedance, with the proposed approximation, with the TMM assuming a lossless radiation impedance and numerically.

From this figure it is evident that there is good agreement between all four methodologies for the proposed geometry. When comparing the approximation against the TMM with a lossy radiation impedance, there is excellent agreement. This indicates that the approximation provides a reliable and robust method to simplify expressions with the TMM. However, when comparing these plots with those produced by the TMM with a lossless radiation impedance and numerically, it is evident that there is a slight discrepancy. In all cases the resonant frequency is in excellent agreement, but the maximum value of the absorption coefficient differs slightly. This is logical as the approximation and TMM with lossy radiation impedance will be overestimating the losses within the system, which can increase or reduce the absorption coefficient at resonance depending upon the location of the zero within the complex frequency domain. This discrepancy is most visible in Figures 6.2b and 6.2c, where the absorption coefficient is greater at resonance with the numerical and TMM with lossless radiation impedance methods.

To investigate the accuracy of the derived approximation for a single Helmholtz resonator, presented in equation 6.10, plots of the absorption coefficients produced with the three analytical methodologies for varying neck to cavity width rations are presented in Figure 6.3. This is an important consideration as the approximation is derived upon the basis that there is a large impedance contrast between the neck and cavity such that a small order term can be obtained.

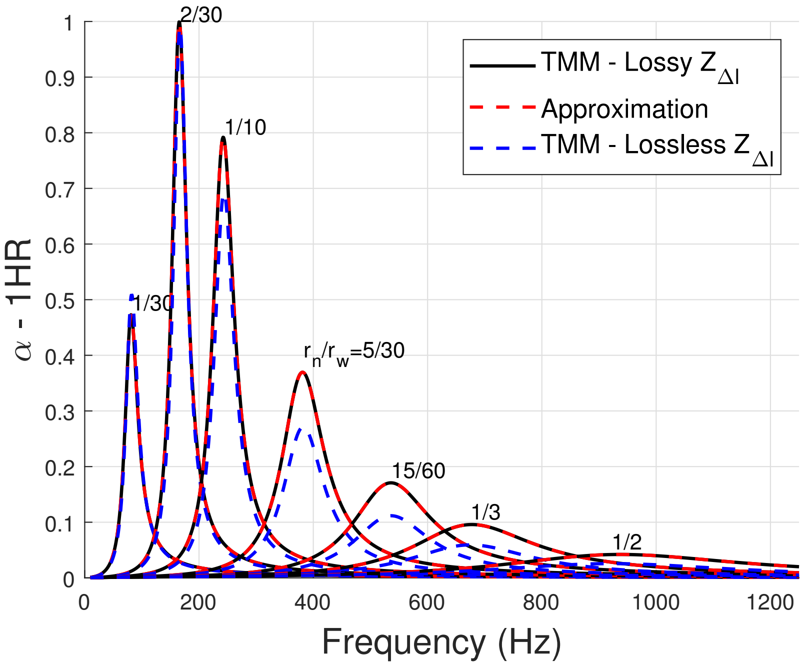

Figure 6.3: Plots of the absorption coefficient for a single Helmholtz resonator system with various neck to cavity width rations produced with all three analytical methodologies.

From this figure it is evident that at every neck to cavity ration, there is excellent agreement between the approximation and the TMM with lossy radiation impedance. This indicates that the selection of the small order term based upon the impedance contrast provides a robust approach when approximating the surface impedance of Helmholtz resonator systems. However, when in comparison with the TMM with lossless radiation impedance, which had excellent agreement with the numerical methodology in Figure 6.2, it can be seen that there is a discrepancy in the absorption amplitude at resonance. This is the same issue that was evident in Figure 6.2, both the approximation and the TMM with lossy radiation impedance, which it approximates, overestimates the losses within the system. However, the frequency at which resonance occurs are in excellent agreement between the three analytical methodologies, indicating that the overestimation of losses is not significant enough to result in a material decease in the resonant frequency of the system .

To assess the viability of this type of resonant system with an array of M identical coupled Helmholtz resonators for low frequency sound absorption, complex frequency domain plots of the reflection coefficient obtained with the approximation expression in equation 6.10 can be seen in Figure 6.4. Figure 6.4a is a plot for $M = 1$, Figure 6.4b is a plot for $M = 2$ and Figure 6.4c is a plot for $M = 3$,.

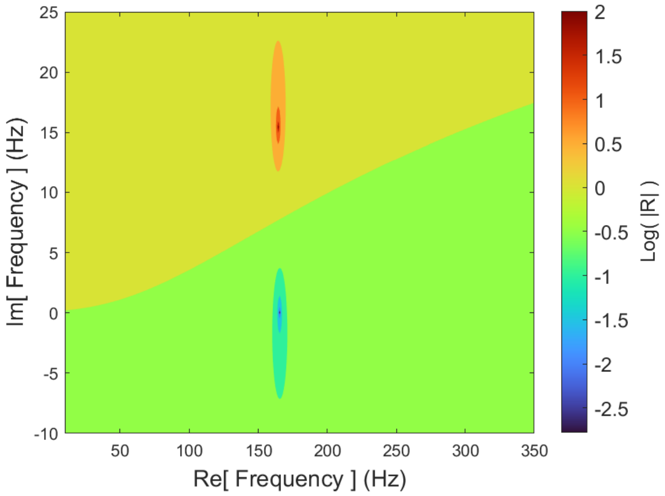

(a) Complex frequency domain plot of Log($|R|$) when $M = 1$.

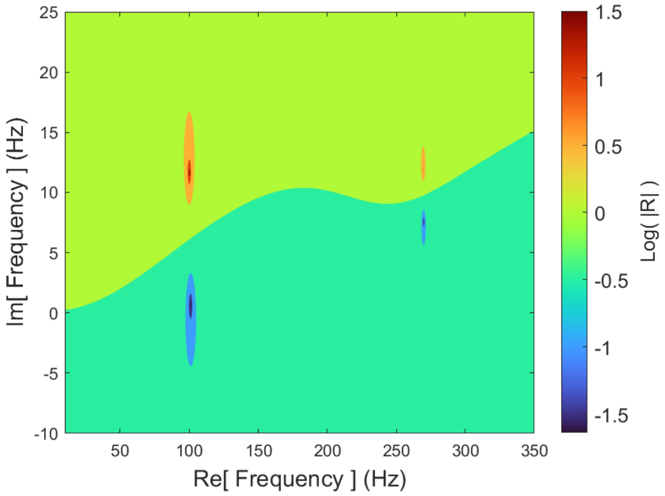

(b) Complex frequency domain plot of Log($|R|$) when $M = 2$.

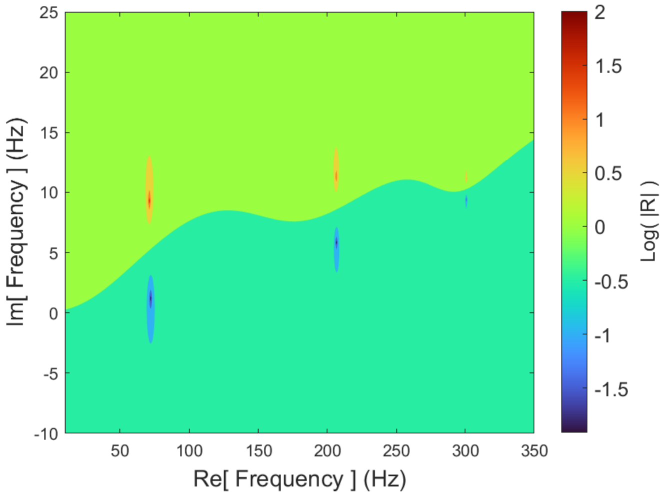

(c) Complex frequency domain plot of Log($|R|$) when $M = 3$.

Figure 6.4: Complex frequency domain plots of Log($|R|$) for the array of coupled identical Helmholtz resonators when $M = 1, 2, 3$.

From Figure 6.4a it is evident that for the single resonator system, the critical coupling condition is fulfilled such that the zero of the system is on the real frequency axis. This is evident by the perfect absorption seen in Figure 6.2a. In Figure 6.4b, the introduction of the second Helmholtz resonator has introduced a second, higher frequency pole and zero pair. There is also a material decrease in the real value of the frequency of the zero coupling of the resonators [94], resulting in a reduction in the resonant frequency of this Helmholtz resonator. Additionally, by adding the second resonator, the critically coupled zero of the first Helmholtz resonator has been shifted up in to the positive complex frequency domain, reducing the absorptive performance. It must also be noted that the zeros are not located on the same plane of complex frequency values. This is further evidenced in Figure 6.4c by the introduction of the third resonator. Due to this phenomenon, it can be deduced that it is only possible to achieve critical coupling with one zero of the system, meaning perfect absorption at multiple frequencies is not possible. One possible use case, however, would be to optimise the system such that the most lowest frequency resonator becomes critically coupled. This could provide a methodology to achieving perfect absorption at a very low frequency.

One interesting avenue which could be further explored is that of a very low frequency absorption with an absorption peak with a large Q factor. Typically, the Q factor of an absorption peak produced by a Helmholtz resonator is determined by the ratio of the neck and cavity widths. This is evident in Figure 6.3, where the Q factor of the absorption peak increases with an increase in neck to cavity width ratio. Adversely, beyond the critical coupling point, an increase in the neck width produces worse absorptive performance, again, as evident in Figure 6.3. By utilising the strong coupling within a system of identical Helmholtz resonators, a system could be optimised such that Helmholtz resonator with a large width to cavity ratio is critically coupled within the very low frequency regime by the addition of coupled identical Helmholtz resonators. This would allow for very low frequency absorption with a peak of high Q factor.

6.3 Resonant Frequency Analysis

Due to the simple nature of the approximated impedance expressions and the fact that they are constructed of polynomials, it is a simple matter to derive the resonant frequencies of the three presented systems for $m = 1, 2$ and 3. To illustrate, the imaginary component of Z_{HR} is 0 at resonance, therefore it is a simple matter of finding the x value for which the respective polynomial is also equal to 0. Consider an arbitrary solution $x = A$, by rearranging (6.8), the following relation can be found

$$f_{res} = \frac{1}{2\pi}\left(\frac{S_n}{V_c l'_n}\right)^{1/2} Re\left[\frac{K_c(\omega)}{\rho_n(\omega)}\right]^{1/2}\left(A\right)^{1/2}. \tag{6.11}$$

Furthermore, by assuming a lossless system and taking the high frequency limit

$$\lim_{\omega\to\infty} Re\left[\frac{K_c(\omega)}{\rho_n(\omega)}\right]^{1/2} = c_0, \tag{6.12}$$

as depicted in Figure 6.5,

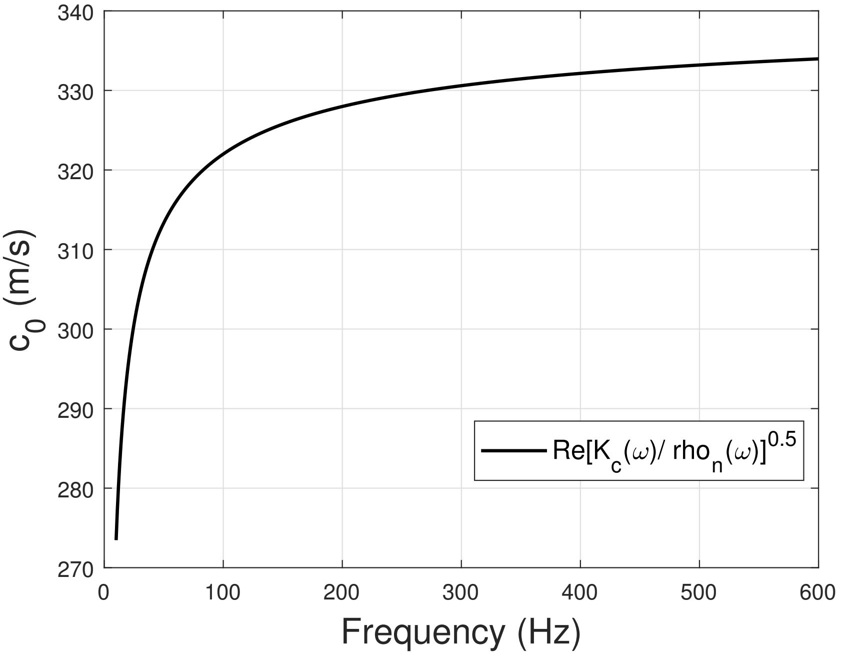

Figure 6.5: Plot of the high frequency limit for Re$[K_c(\omega)/\rho_n(\omega)]^{1/2}$.

equation (6.11) can be simplified to

$$f_{res} = \frac{c_0}{2\pi}\left(\frac{S_n}{V_c l'_n}\right)^{1/2}\left(A\right)^{1/2}. \tag{6.13}$$

To determine the resonant frequencies of the three systems, it is necessary to find A. This is done by solving the numerator polynomials in the approximate surface impedance expressions in equation 6.9, which can be found in Table 6.2.

m	A
1	1
2	$(3-\sqrt{5})/2$, $(3+\sqrt{5})/2$
3	$0.19806, 1.5550, 3.2470$

Table 6.2: Values of A for the three HR systems.

From this it is evident that for a single HR , the classical formula for the resonant frequency of a Helmholtz resonator is obtained;

$$f_{res} = \frac{c_0}{2\pi}\left(\frac{S_n}{V_c l'_n}\right)^{1/2}. \tag{6.14}$$

To assess the validity of equation (6.13), the resonant frequencies for the three HR systems obtained using TMM with and without a lossy radiation impedance, numerically and with equation (6.13) have been obtained. The values of which can be seen in the Table 6.3.

f_{res}	TMM - Lossy $Z_{\Delta l}$	Equation (6.13)	TMM - Lossless $Z_{\Delta l}$	Numerical
$m = 1$	173	186	167	168
$m = 2$	$101, 270$	$107, 280$	$102, 271$	$102, 270$
$m = 3$	$72, 207, 301$	$77, 216, 311$	$73, 208, 303$	$73, 207, 301$

Table 6.3: Values of f_{res} [Hz] for the three HR systems obtained using TMM with and without a lossy radiation impedance, numerically and with equation (6.13).

From this table it is evident that there is relatively good agreement between the determination of the lossless resonant frequencies with equation (6.13) with the other presented methodologies. It can be seen that the resonant frequency obtained by the approximation is consistently higher for every resonance. This is the influence of viscothermal losses not being captured within equation (6.13), as the introduction of losses within the system typically reduces the resonant frequencies due to dampening effect. An indicator to the influence that the introduction of losses has upon the resonant frequency can be seen in Figure 6.5. Typically, the lower the frequency of resonance, the larger influence the losses has upon the resonant frequency. This is displayed by c_0 being lower at these lower frequencies. One method to improve the accuracy of equation 6.13 would be to input the values of c_0 at each numerically computed resonant frequency. The results of this can be seen in Table 6.4.

f_{res}	Equation (6.13) with lossy c_0 value	Numerical	c_0 [m/s]
$m = 1$	165	168	327
$m = 2$	$101, 270$	$102, 270$	$322, 330$
$m = 3$	$72, 207, 301$	$73, 207, 301$	$318, 328, 331$

Table 6.4: Values of f_{res} [Hz] for the three HR systems obtained with equation (6.13) with a lossy value for c_0 at resonance compared with the numerical results.

Using this methodology there is now a much better agreement in the determination of the resonant frequencies, this is due to the influence of viscothermal losses being accounted for.

6.4 Chapter Conclusion

Within this chapter a method of simplification has been proposed for impedance terms derived by the TMM. This has been applied to the case of a serial array of M coupled identical Helmholtz resonators. The simplification method is reliant upon the use of an impedance contrast to create a small order term which can be used in the Taylor expansion of the TMM impedance expressions. By utilising the leading order term from the Taylor series expansions, simple expressions were found composed of polynomials of the same order as M. Excellent agreement was found when comparing the absorption coefficient obtained via the TMM with a lossy radiation impedance and with this approximation method. However when a comparison is made between the approximation and the TMM with a lossless radiation impedance and numerical results, there is a slight discrepancy in the amplitude of the absorption peaks. This is due to the TMM with lossy radiation impedance and the expressions which approximate this overestimate the amount losses within the system, changing the location of the zero in the complex frequency domain. This was further exacerbated with greater resonator neck to width ratios.

Upon analysis of the complex frequency domain of the modelled systems it was concluded that it is only possible to achieve critical coupling with one zero of the system, meaning perfect absorption at multiple frequencies is not possible. One possible use case could be to optimise the system such that the lowest frequency resonator becomes critically coupled. This could provide a methodology to achieving perfect absorption at a very low frequency.

It was also found that the resonant frequencies of the systems can be obtained through the solution of the polynomials present within the numerator of the impedance approximations. However, it is evident that there is a slight discrepancy between the approximate resonant frequency equations and those achieved by the other methodologies. This is due to viscothermal loss effects not being taken in to account. By adjusting the speed of sound within the approximate resonant frequency expression to that of a lossy system at specific resonant frequencies, accurate predictions to the resonant frequencies of systems of identical coupled Helmholtz resonators can be determined.

Chapter 7

Low frequency attenuation of acoustic waves in a perforated pipe

The attenuation of acoustic waves in a pipe by silencers is typically achieved through the employment of rigidly backed cavities, connected to the pipe by a perforated panel. For silencers with partitioned cavities with a single perforation, i.e. a Helmholtz resonator, excellent attenuation can be achieved at the resonant frequency of the resonator. Multiple Helmholtz resonators can be side-loaded to the pipe, all tuned to different frequencies in order to achieve the broadband attenuation of noise [56]. Side-loaded Helmholtz resonators can be optimised to increase their absorptive performance by changing the separation distance between subsequent resonators and by adjusting their geometry and thus visco-thermal losses to critically couple them with the pipe. A similar technique has been employed in the design of sound absorbing acoustic metamaterials in order to achieve perfect broadband absorption in one and two port systems much smaller than the wavelength of the sound wave [18, 45].

For silencers with non-partitioned cavities and panels composed of multiple identical perforations along the length of the silencer a similar phenomenon occurs. If the perforated separating panel has a low porosity, a Helmholtz resonator type of attenuation occurs. As the porosity increases, the silencer behaves more like an expansion chamber [5]. Different configurations of partitions can be used to alter the number of resonances. Dissipative materials can be introduced to achieve broadband attenuation [95]. A limitation of these types of silencers is the requirement for large cavity volumes or narrow neck regions to achieve low frequency attenuation. A large cavity volume is often impractical and having narrow regions often results in poor attenuation of acoustic waves due to large amounts of visco-thermal losses often resulting in over-damping of the system [57].

Through the use of a metamaterial consisting of an array of perforations along a waveguide, where no cavities are present, it has been theoretically and experimentally shown that negative bulk modulus can be obtained from zero to an upper bound [52]. This is due to the non-local resonant effect of the perforations allowing for the occurrence of a bandgap where zero transmission occurs and where the band gap upper bound is determined by the system geometry. This has been corroborated in the non-linear regime through the employment of high amplitude excitation [53] and it has also been shown that through the coupling of the perforations within an array of elastic membranes, both negative bulk modulus and dynamic density can be achieved [54]. Finally, it has been theoretically shown that a sonic crystal in which the surfaces of each scatterer is modelled with an acoustically soft boundary condition, a band gap is created from zero to an upper bound frequency determined by the surface area and periodicity of the soft scatterers [96].

In this chapter an ideal analytical model is created to examine the influence periodic arrangements of sound-soft backed perforations have within a waveguide formed by an air-filled pipe. It is observed that the presence of periodically arranged soft scatterers result in a band gap from 0 Hz to an upper bound. The upper bound of this band gap is determined by the dimensions and separation of the perforations. Results are validated numerically with two modelling approaches employed to further refine the analytical model. Experimental evidence of a band gap produced by acoustically soft scatterers is presented. This concept of acoustically soft scatterers much smaller than the wavelength enables us to achieve high attenuation at a very low frequency [97].

This chapter is set out as follows. In the background theory section an analytical model is derived using the transfer matrix method. This model is then used to assess the acoustic transmission loss of a pipe that wall is composed of periodic arrays of acoustically soft scatterers. Results from this analytical model are parametrically compared with those computed numerically for a variety of perforation geometries. This enables us to assess the relationship between variations in geometry and the width of the band gap attained. Then, further numerical results are presented for a non-rigidly backed perforated pipe to understand better the acoustically soft boundary phenomenon occurring within the perforations. Finally, experimental results are presented and used to validate the numerical model.

7.1 Ideal Analytical Model

7.1.1 Impedance of a perforation with soft boundary conditions

To determine the impedance of a single circular perforation of length d, characteristic impedance Z_p and wavenumber k_p, with a soft boundary condition at depth $x = d$, the transfer matrix method is used. The full matrix, T, is derived from:

$$T = M_{\Delta l} M_p, \tag{7.1}$$

where M_p models the cavity and is given by

$$M_p = \begin{bmatrix} \cos(k_p d) & \mathrm{i} Z_p \sin(k_p d) \\ \frac{\mathrm{i}}{Z_p} \sin(k_p d) & \cos(k_p d) \end{bmatrix}. \tag{7.2}$$

$M_{\Delta l}$ in eq. (7.1) models the length correction due to pressure radiation at the interface between the perforation and the pipe, given by:

$$M_{\Delta l} = \begin{bmatrix} 1 & \mathrm{i} Z_p k_p \Delta l \\ 0 & 1 \end{bmatrix}. \tag{7.3}$$

For a circular perforation, the length correction is: [72]

$$\Delta l = 0.82 \left[1 - 0.235 \frac{r_p}{r_w} - 1.32 \left(\frac{r_p}{r_w} \right)^2 + 1.54 \left(\frac{r_p}{r_w} \right)^3 - 0.86 \left(\frac{r_p}{r_w} \right)^4 \right] r_p. \tag{7.4}$$

Here, r_w is the radius of the pipe (waveguide) and r_p is the radius of the perforation. To account for the acoustically soft boundary at the end of the perforation, the final T matrix is multiplied by $[0, 1]^T$, which provides a soft termination to the perforation at $x = d$ where acoustic volume flux is $V_{x=d}$ and pressure is $p_{x=d} = 0$. The characteristic impedance of the perforation with an acoustically soft boundary, Z_s, can then be found as:

$$Z_s = \frac{P_{x=0}}{V_{x=0}} = \frac{T_{12}}{T_{22}} = \mathrm{i} Z_p \tan(k_p (d + \Delta l)). \tag{7.5}$$

7.1.2 Finite periodic system of sound-soft scatterers

Consider a finite length of a pipe with n_t periodic arrangements of sound soft scatterers. Each unit cell has a length h and cross sectional area S_w. The general geometry of the system can be seen in Figure 7.1.

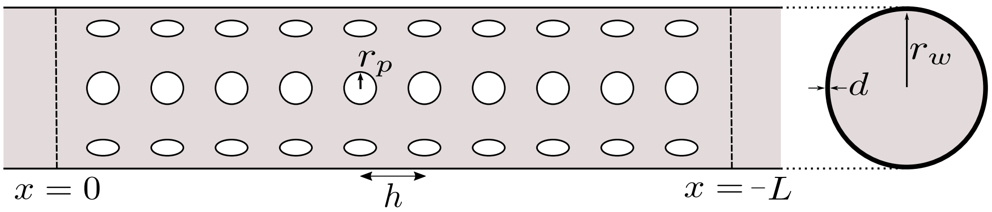

Figure 7.1: Graphical representation of a finite system of sound-soft scatterers.

The transfer matrix for the total system is given by

$$T = \left(M_w M_s M_w\right)^n . \tag{7.6}$$

M_w is the transfer matrix for a fluid layer of length $h/2$ and M_s is given by

$$M_s = \begin{bmatrix} 1 & 0 \\ N/Z_s & 1 \end{bmatrix}, \tag{7.7}$$

where N denotes the number of scatterers per unit cell. The total length of the system $L = nh$. The transmission loss (TL) of the total system can then be obtained as

$$TL = 20 \log_{10} \left| \frac{T_{11} + T_{12}/Z_w + Z_w T_{21} + T_{22}}{2} \right|, \tag{7.8}$$

where Z_w is the characteristic impedance of the waveguide. As this system is symmetric and reciprocal, the transmission, reflection and absorption coefficients can be determined as:

$$T = \frac{2\mathrm{e}^{-\mathrm{i}kL}}{T_{11} + T_{12}/Z_w + Z_w T_{21} + T_{22}}, \tag{7.9}$$

$$R = \frac{T_{11} + T_{12}/Z_w - Z_w T_{21} - T_{22}}{T_{11} + T_{12}/Z_w + Z_w T_{21} + T_{22}}, \tag{7.10}$$

$$\alpha = 1 - |R|^2 - |T|^2. \tag{7.11}$$

7.1.3 Infinitely periodic structure of sound-soft scatterers

Assuming plane wave propagation in a pipe with periodic imperfections, the Bloch Floquet theorem (as presented in Section 2.3) can be fulfilled so that the transfer matrix of a single unit cell can be described as follows [34, 37, 38]:

$$\begin{bmatrix} p \\ V \end{bmatrix}_{x=o} = T \begin{bmatrix} p \\ V \end{bmatrix}_{x=-h} = \begin{bmatrix} T_{11} & T_{12} \\ T_{21} & T_{22} \end{bmatrix} \begin{bmatrix} p \\ V \end{bmatrix}_{x=-h} = \begin{bmatrix} T_{11} & T_{12} \\ T_{21} & T_{22} \end{bmatrix} \begin{bmatrix} \mathrm{e}^{\mathrm{i}qh} p \\ \mathrm{e}^{\mathrm{i}qh} V \end{bmatrix}_{x=0}, \tag{7.12}$$

where q is the Bloch wavenumber. By rearranging we obtain:

$$\left(\begin{bmatrix} T_{11} & T_{12} \\ T_{21} & T_{22} \end{bmatrix} - \begin{bmatrix} \mathrm{e}^{-\mathrm{i}qh} & 0 \\ 0 & \mathrm{e}^{-\mathrm{i}qh} \end{bmatrix} \right) \begin{bmatrix} p \\ V \end{bmatrix}_{x=-h} = 0. \tag{7.13}$$

By substituting $\Lambda = \mathrm{e}^{\mathrm{i}qh}$, the following eigenvalue problem can be constructed:

$$\begin{vmatrix} T_{11} - \Lambda & T_{12} \\ T_{21} & T_{22} - \Lambda \end{vmatrix} = \Lambda^2 - \Lambda \left(T_{11} + T_{12} \right) + |T| = 0. \tag{7.14}$$

In the above equation the determinant, $|T| = 1$, through the principle of reciprocity and therefore the forward and backward propagating Bloch waves display the same dispersion and the Bloch dispersion relation can be found as:

$$\cos(qh) = \frac{1}{2}(T_{11} + T_{22}). \tag{7.15}$$

As such, the dispersion relationship for an infinitely periodic array of sound-soft backed perforations can be expressed as

$$\cos(qh) = \cos(kh) + \frac{\mathrm{i}ZN}{2Z_s} \sin(kh). \tag{7.16}$$

7.2 Ideal Analytical Model Parametric Study

In this section, a parametric study is undertaken where the relationship between the separation, depth and area of the perforations and the width of the band gap produced is investigated. The analytical model is validated using 3D numerical models in COMSOL Multiphysics 6.0.

Details of the selected geometries can be seen in Table 7.1 where the perforation radius is r_p, the perforation depth is d and the unit cell length is h. In all the cases the radius of the pipe, r_w, is 40 mm, the total number of unit cells, n_t, is 10 and the number of perforations per unit cell, N, is 6. These perforations are distributed evenly along the circumference of the pipe. Plots comparing the absorption, transmission and reflection coefficients predicted with the analytical and numerical model in the lossless and lossy cases can be seen in Figure 7.2. In the lossless case the effective fluid properties of the pipe and perforation are calculated with the lossless acoustic impedance and wavenumber such that visco-thermal losses are not taken into consideration. In the lossy cases, all visco-thermal losses are included using equations 2.15 and 2.16 to calculate the acoustic impedance and wavenumber. Plots of the transmission loss predicted with analytical and numerical models and real and imaginary components of the Bloch wavenumber predicted with the analytical model are presented in Figure 7.3. These results are also presented for the lossless and lossy cases. The results shown in Figures 7.2 and 7.3 suggest that there is excellent agreement between the ideal analytical and 3D numerical models.

Table 7.1: Geometrical parameters of the four models validated numerically.

Geometry	r_p (mm)	d (mm)	h (mm)
1	2	5	50
2	2	5	25
3	3	5	50
4	2	10	50

From Figure 7.2a, it is evident that in the lossless case, the introduction of acoustically soft backed perforations results in the reflection coefficient value close to unity at 0 Hz. This behaviour extends to approximately 300 Hz before the reflection coefficient begins returns to 0. Consequently, the transmission coefficient behaves in the opposite manner. This phenomenon is also clear in Figure 7.2b. In the lossless case there is no absorption present, whereas there is in the lossy case. Additionally, with losses the strength of the band gap is reduced, with the reflection coefficient dropping from near unity immediately at frequencies above 0 Hz. There is no discernible change in transmission loss.

In Figure 7.3a a band gap is evident, denoted by the purely imaginary Bloch wavenumber. This purely imaginary Bloch wavenumber indicates that the propagating wave within the the band gap frequency range is evanescent, which is evidenced by the transmission loss across the same frequency range. It can be seen in Figure 7.3b that the introduction of losses reduces the strength of the gap, with real values for the Bloch wavenumber occurring at 0 Hz.

In Geometry 2, the length of the unit cell has been halved, reducing the separation between the rows of perforations. Upon comparison of Figure 7.2c to Figure 7.2a, it can be seen that by decreasing the unit cell length, the width of the band gap is increased. It is worth noting that the reflection and transmission coefficients appear to change more gradually in this scenario. Again, as seen in Figure 7.2d, the introduction of losses induces absorption within the system. When looking at Figures 7.3c and 7.3d, the transmission loss seems similar in amplitude to that predicted for Geometry 1, indicating that whilst the separation distance influences the width of the band gap, it does not greatly impact transmission loss.

To further investigate the relationship between the perforation geometry and the width of the band gap produced, Geometry 3 is chosen to have the same geometrical parameters as Geometry 1, but an increase in perforation radius by 1 mm. When examining Figures 7.2e and 7.2f, the main difference to Geometry 1 is, an increase in the width of the band gap. This time, the change in the reflection and transmission coefficients is similar to that produced by Geometry 1. From Figures 7.3e and 7.3f it can be seen that by increasing the radius of the perforations it is possible to increase the width of the band gap and amount of transmission loss within the band gap. This result indicates that the overall surface area of soft boundary conditions influences the transmission loss produced by the perforations.

The final parameter is the depth of the perforation and how it influences the width of the band gap produced. In Geometry 4, the depth of perforations is doubled, whilst the remaining parameters are kept consistent with Geometry 1. From Figures 7.2g and 7.2h, it can be seen that the width of the band gap is reduced, with the reflection and transmission coefficients changing more gradually. In Figures 7.3g and 7.3h, it can be seen that by increasing the depth of the perforations, the transmission loss is reduced in comparison to Geometry 1.

Therefore, for this system it can be determined that the size and strength of the band gap is dependant on multiple factors. Reducing the unit cell length, but keeping the total number of unit cells increases the width of the gap, but it does not increase the transmission loss within the band gap. Increasing the size of the perforation increases the surface area where a sound-soft boundary condition is present, which increases the size and transmission loss of the band gap. Finally, an increase of the perforation depth reduces the size and transmission loss within the band gap.

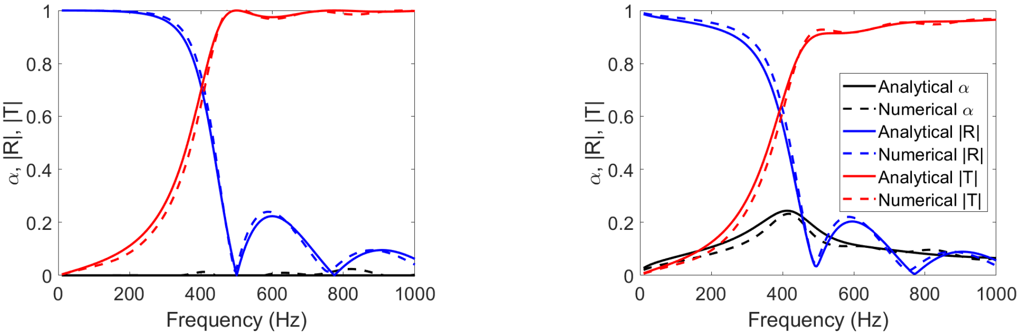

(a) Geometry 1 - Lossless (b) Geometry 1 - Lossy

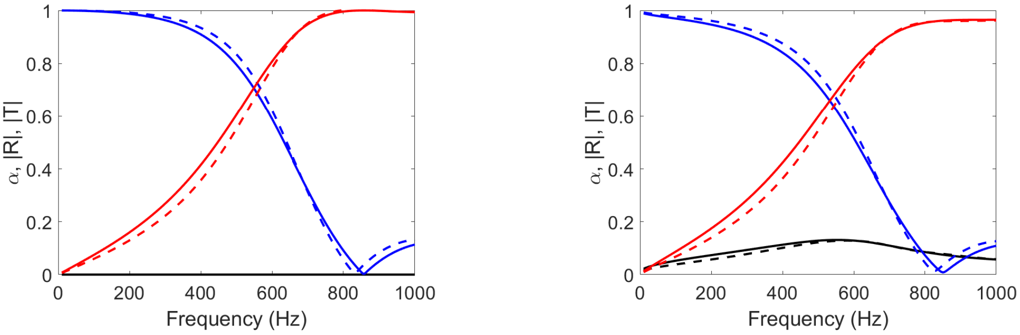

(c) Geometry 2 - Lossless (d) Geometry 2 - Lossy

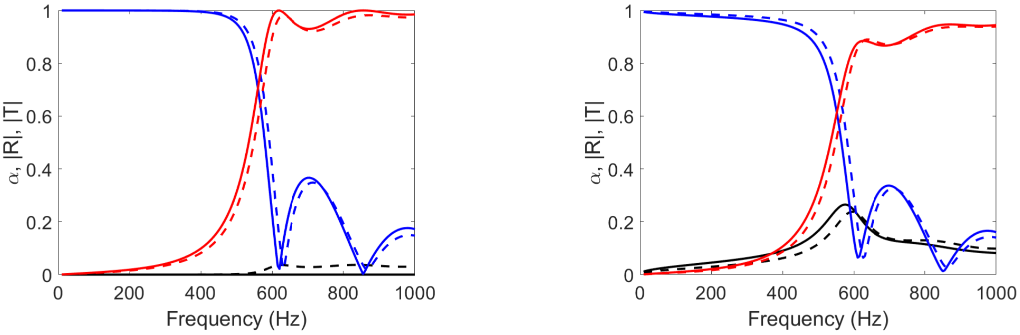

(e) Geometry 3 - Lossless (f) Geometry 3 - Lossy

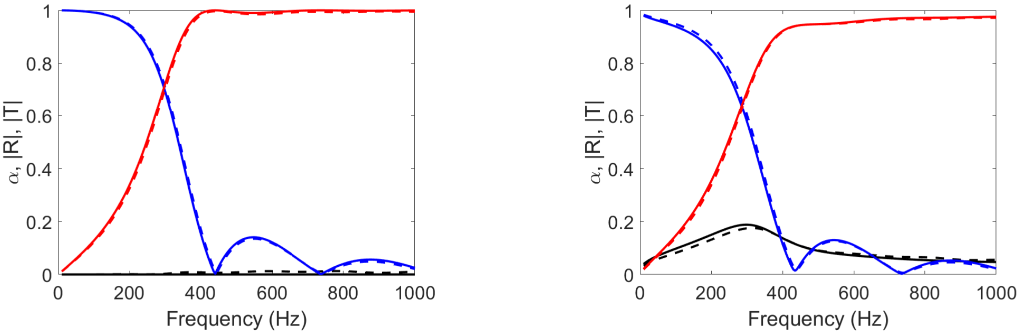

(g) Geometry 4 - Lossless (h) Geometry 4 - Lossy

Figure 7.2: Analytical and numerical plots of α, $|R|$ and $|T|$ for Geometries 1-4 (Table 7.2) in the lossless and lossy cases.

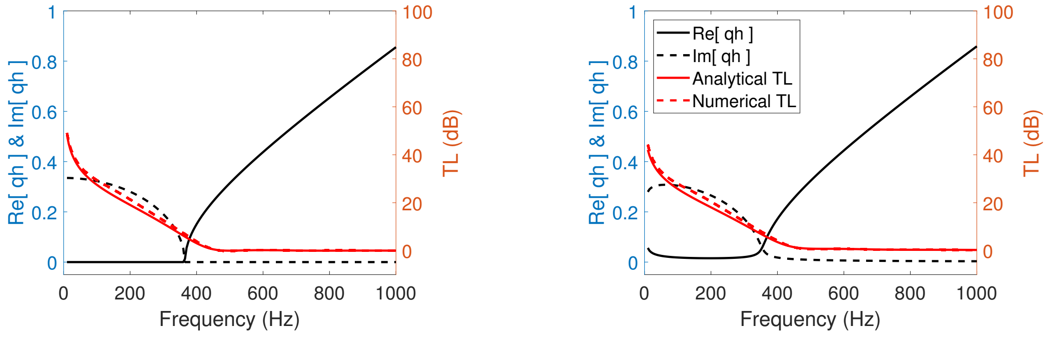

(a) Geometry 1 - Lossless (b) Geometry 1 - Lossy

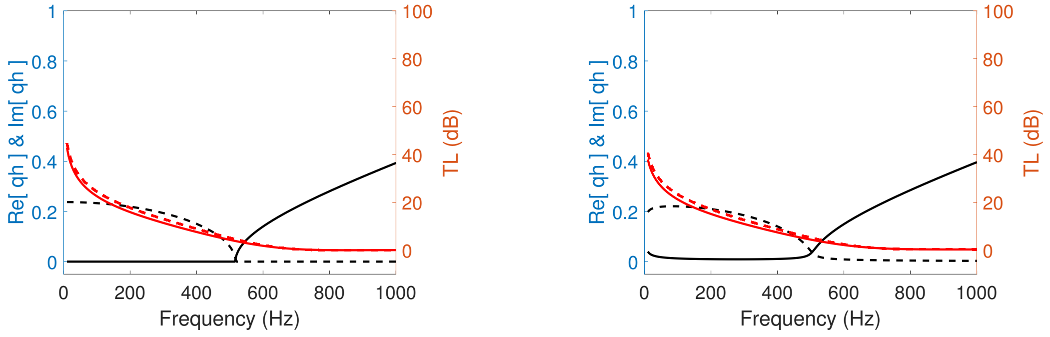

(c) Geometry 2 - Lossless (d) Geometry 2 - Lossy

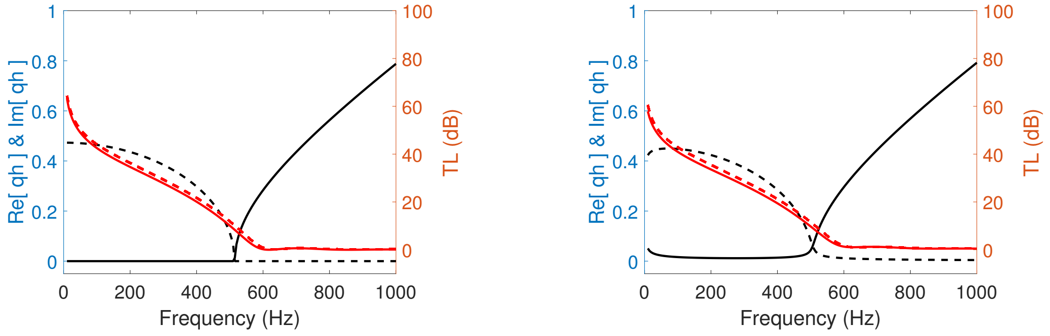

(e) Geometry 3 - Lossless (f) Geometry 3 - Lossy

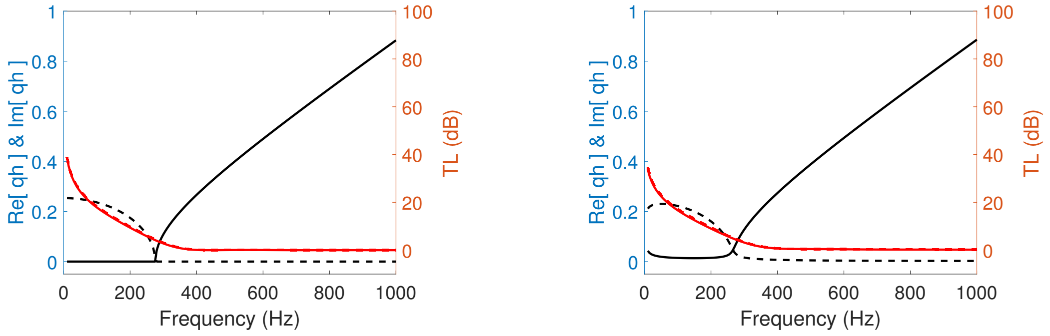

(g) Geometry 4 - Lossless (h) Geometry 4 - Lossy

Figure 7.3: Analytical plots of the real and imaginary components of the Bloch wavenumber, and analytical and numerical plots of the transmission loss (TL) for Geometries 1-4 (Table 7.2) in the lossless and lossy cases.

7.3 Numerical Study of sound soft phenomenon

In this section, a numerical study is undertaken to further understand the acoustically soft boundary effect produced by non-rigidly backed perforations. To do this, two variants of numerical models are used which model the soft boundary condition differently. In the first variant the perforations are encompassed by an air gap and then a perfectly matched layer (PML), whereas in the other variant the outer boundary of the perforations are modelled with an ideal acoustically soft boundary condition. The PML is used to artificially attenuate any acoustic wave propagating away from the perforated pipe and minimise reflections back in to the pipe from the boundary of the fluid domain surrounding the pipe [75]. Graphical representations of these two variants can be seen in Figures 7.4a and 7.4b, respectively.

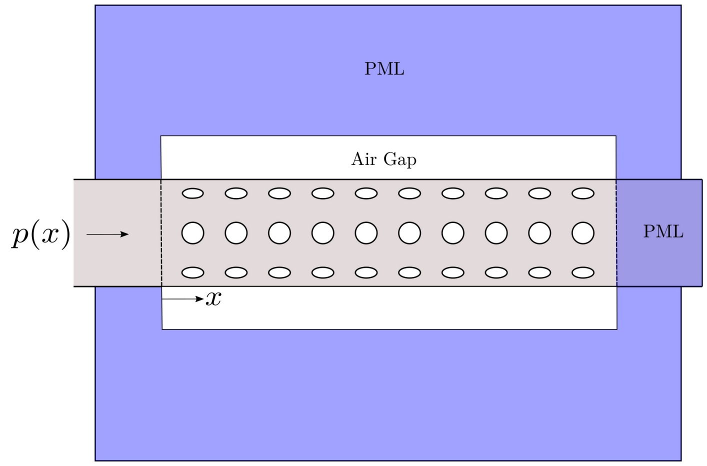

(a) Perforated pipe encompassed by an air gap and PML.

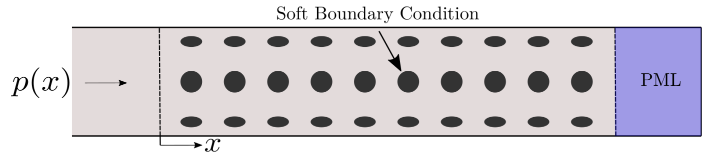

(b) Perforated pipe with sound-soft backed perforations.

Figure 7.4: Graphical representation of the numerically modelled perforated pipes for an investigation in to the sound-soft phenomenon.

Three perforation geometries and spacing are modelled with the parameters summarised in Table 7.2.

Table 7.2: The parameters of the the three geometries of perforations used in the numerical model of the perforated pipe.

Geometry	r_p (mm)	d (mm)	h (mm)	n
1	5	5	50	11
2	5	5	25	21
3	2.5	5	25	21

The radius of the pipe is kept constant between each model at $r_w = 40$ mm, and the number of perforations per unit cell is always $N = 1$. The transmission, reflection and absorption coefficient spectra for Geometries 1 - 3 (see Table 7.2) are shown in Figure 7.5. These results are given for the perforated pipe surrounded with an air gap (dashed lines) and ideal acoustically soft boundary (solid lines).

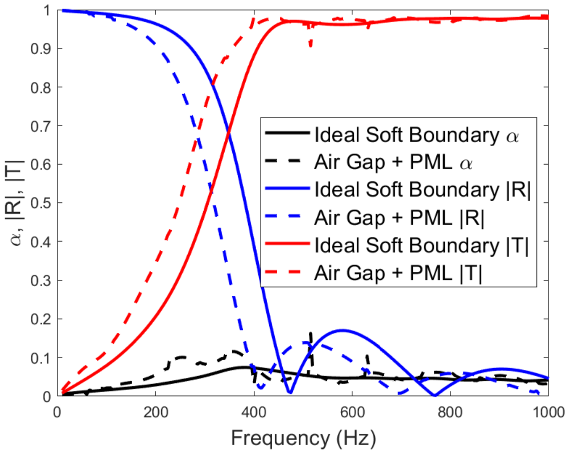

(a) Geometry 1

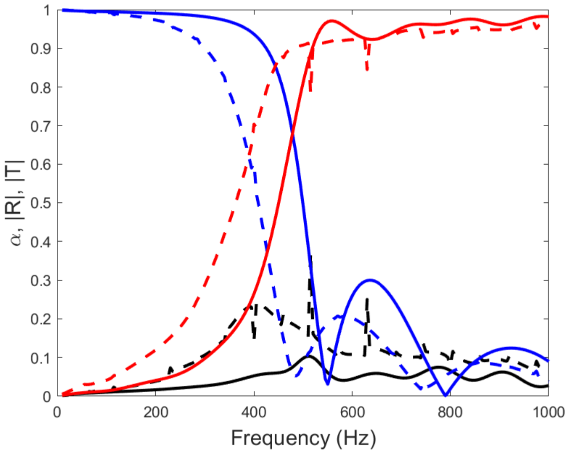

(b) Geometry 2

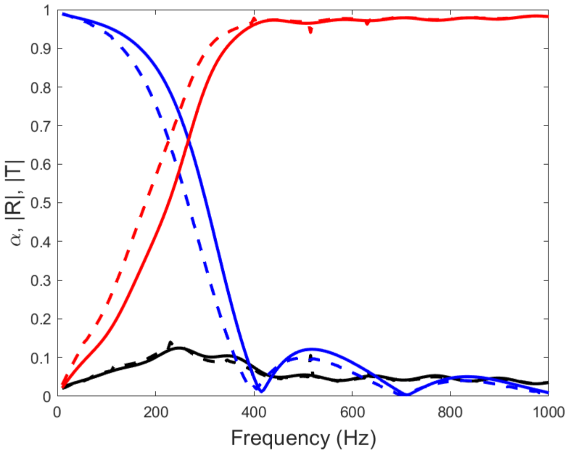

(c) Geometry 3

Figure 7.5: Plots of α, $|R|$ and $|T|$ for both numerical variants for models 1 - 3.

The behaviour of the absorption, reflection and transmission coefficients shown in Figure 7.5 suggests that the band gap phenomenon cased by the perforations is present in the both variants of the numerical model. This is evidenced by the near unity reflection coefficient as the frequency reduces to 0 Hz. The width of the band gap differs between the two variants of the numerical model. In the case of the model for the ideal acoustically soft boundary conditions, the high attenuation band extends over a larger frequency range for each of the three perforation geometries considered in this study. It can therefore be determined that an additional length correction due to pressure radiation at the soft boundary of the perforation is required. Additionally, in Figures 7.5 (a) and (b), it can be seen that the numerical results produced for the variant with the air gap and PML are noisy due to numerical artifacts resulting from the PML.

To gain further insight, graphics showing the absolute acoustic pressure for geometry 1 - 3 from the air gap with PML numerical variant can be seen in Figure 7.6. In each graphic the chosen frequency was based upon the condition $|R| = 0.5$. This criteria was used to select the frequency due to the large discrepancy in results between the two numerical variants at these values.

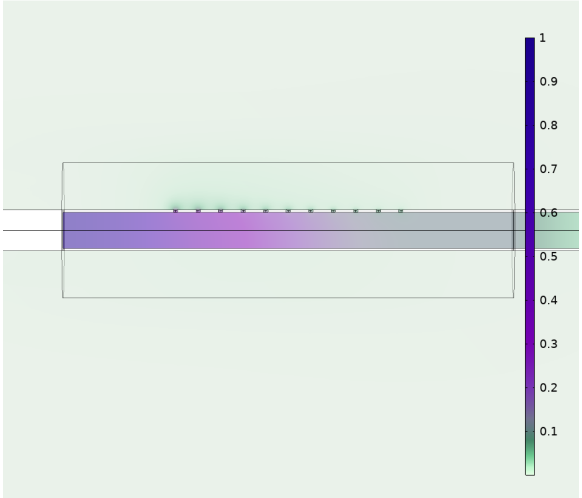

(a) Geometry 1 at 315 Hz

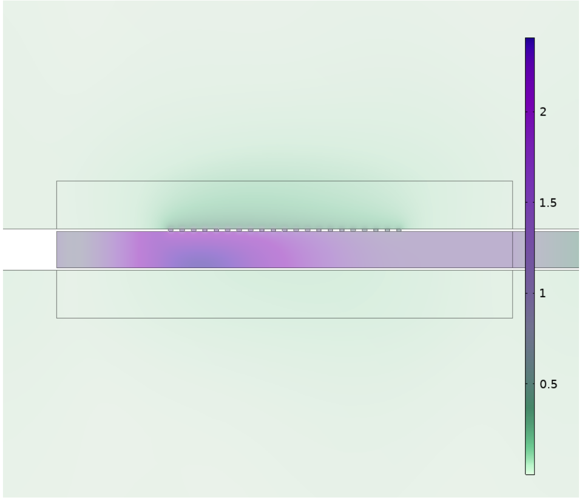

(b) Geometry 2 at 410 Hz

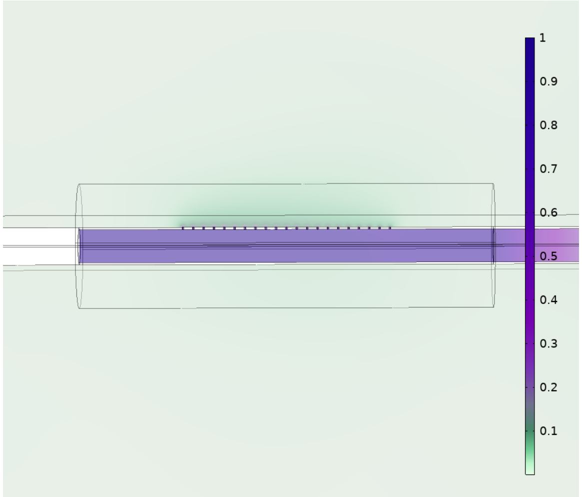

(c) Geometry 3 at 265 Hz

Figure 7.6: Absolute acoustic pressure for Geometries 1 -3 for the numerical variant where the perforated pipe is encompassed by an air gap and PML.

From Figure 7.6 it can be seen that there is pressure radiation occurring at the discontinuity between the perforations and the surrounding medium. This indicates that the sound boundary is acting beyond the perforation. There is an additional added length which is causing an overall decrease in the maximum frequency achieved by the band gap. This additional length is increasing the depth of the perforation.

7.4 Revised Soft-backed Perforation Impedance

In order to account for the extra pressure radiation that occurs at the discontinuity from the perforation and the surrounding medium, an additional length correction to the perforation depth must be accounted for in the expression for the impedance of a perforation with a soft boundary condition. Equation 7.4 gives the length correction, Δl, for the pressure radiation at the discontinuity between the perforation and fluid within the perforated pipe. In addition to this, an expression of the length correction for the pressure radiation from an orifice in a tube wall into free space is required. This is given by the following equation [85]

$$\Delta l_2 = \frac{U_p}{8} + k_0^{-1}\chi_0\left(2k_0\sqrt{\frac{S_p}{\pi}}\right), \tag{7.17}$$

where U_p is the perimeter of the perforation, $k_0 = \omega/c_0$ and

$$\begin{aligned}\chi_0(\xi) &= \frac{4}{\pi}\int_0^{\pi} \text{sin}(\xi\,\text{cos}(a))\,\text{sin}^2(a)\;\;\text{da}\\ &\approx \frac{\xi^2}{8}\;\;\text{for}\;\;\xi \ll 1.\end{aligned} \tag{7.18}$$

Here $\xi = 2k_0\sqrt{S_p/\pi}$. If the length correction for the pressure radiation at the discontinuity between the perforation and pipe is

$$\Delta l_1 = 0.82\left[1 - 0.235\frac{r_p}{r_w} - 1.32\Big(\frac{r_p}{r_w}\Big)^2 + 1.54\Big(\frac{r_p}{r_w}\Big)^3 - 0.86\Big(\frac{r_p}{r_w}\Big)^4\right] r_p, \tag{7.19}$$

as described in equation 7.4, then the equation for the revised impedance for a perforation with a sound soft boundary (see equation 7.5) is

$$Z_s = \text{i}Z_p\,\text{tan}(k_p(d + \Delta l_1 + \Delta l_2)). \tag{7.20}$$

The methodology presented in Section 7.1.2 and equation 7.20 were used to compare the revised analytical model against the numerical simulation detailed in Section 7.3. The results of this comparison are shown in Figures 7.7 for the three geometries presented in Table 7.2. Figures 7.7 presents the absorption, reflection and transmission coefficients for the perforated pipe encompassed by an air gap and PML. From these figures it can be seen that there is now excellent agreement between the revised analytical and numerical models suggesting that the revised analytical model now provides a simple and robust way to determine the acoustic attenuation in a pipe with non-rigidly backed circular perforations.

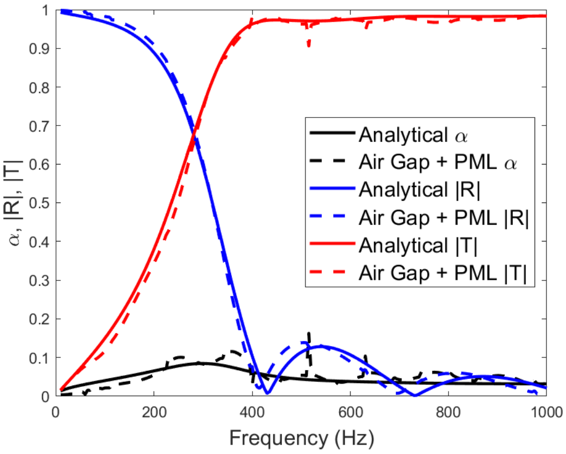

(a) Model 1

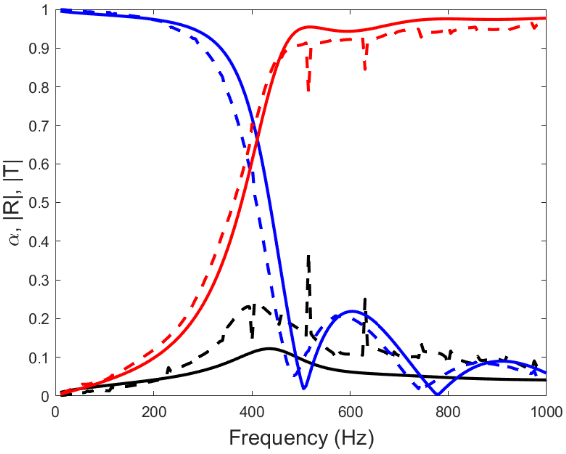

(b) Model 2

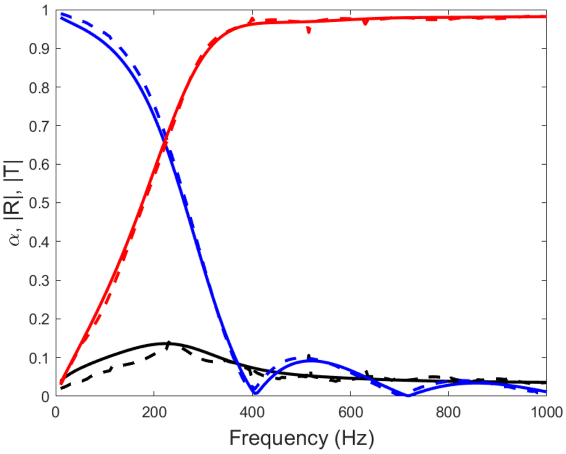

(c) Model 3

Figure 7.7: The spectra of the absorption, α, reflection, $|R|$, and transmission, $|T|$, coefficients predicted with the revised analytical model and numerical model for the pipe with the peroration geometries defined in Table 7.2.

7.5 Experimental Results

In order to validate the proposed analytical and numerical models and to illustrate practically the existence of the low frequency band gap, an experimental pipe rig was set up in the ICAIR laboratory at the University of Sheffield. The experimental rig included a 1.32 m perforated pipe with a smooth inner radius 0.8 m and a corrugated outer radius, with three perforations per cross-section and approximately 1 m of separation between the speaker and an array of 9 microphones as illustrated in Figures 7.8 (a)-(c). The speaker was piston-on-a-sphere which is designed to act like a source with high radiation efficiency [98]. The speaker was installed at one end of the perforated pipe as shown in Figure 7.8 (a). The speaker was driven by a sine sweep generated between 50 Hz and 25 kHz with the help of NI-9260 analog output module and B&K type 2716C amplifier.

The microphone array made of 9 GRAS 46AE 1/2" CCP free-field standard microphones was installed at the other end of the pipe. It was arranged along the pipe diameter as shown in Figure 7.8 (b). The microphone array was used to filter out the plane wave mode in a sufficiently broad frequency range. It is noted that the location of holes in the perforated pipe along the pipe circumference were not consistent and varied along the pipe length. The spacing between the rows of perforation was fixed at $h = 20$ mm and the width of each perforation was approximately 20 mm as shown in Figures 7.9 (a) and (b), respectively. A National Instrument data acquisition module Type NI-9232 was used to acquire data at the sampling rate of 51.2 kHz.

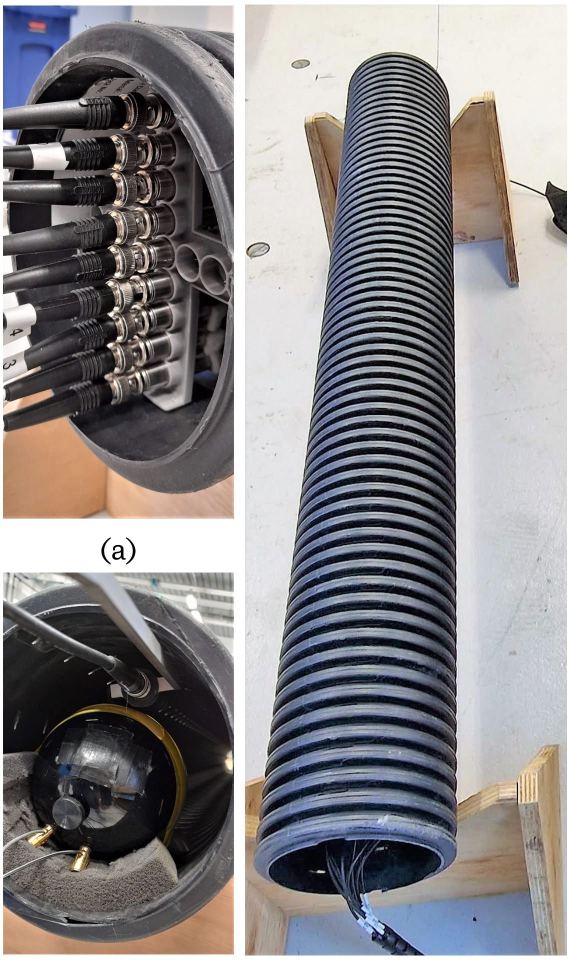

(a)

(b)

(c)

Figure 7.8: The experimental pipe set up at the Integrated Civil and Infrastructure Research Centre (ICAIR): (a) sound speaker at the source end; (b) array of 9 microphones at the receiver end; (c) perforated pipe with speaker and microphone array installed at the opposite ends of the pipe.

Figure 7.10 illustrates the transmission loss obtained with the following equation

$$TL = 20 \log_{10} \left| \frac{p_{ref}}{p_{rec}} \right| , \tag{7.21}$$

where p_{ref} is the acoustic pressure recorded at the reference microphone in the vicinity of the sound speaker and p_{rec} is the acoustic pressure recorded at the receiver side with the array microphones.

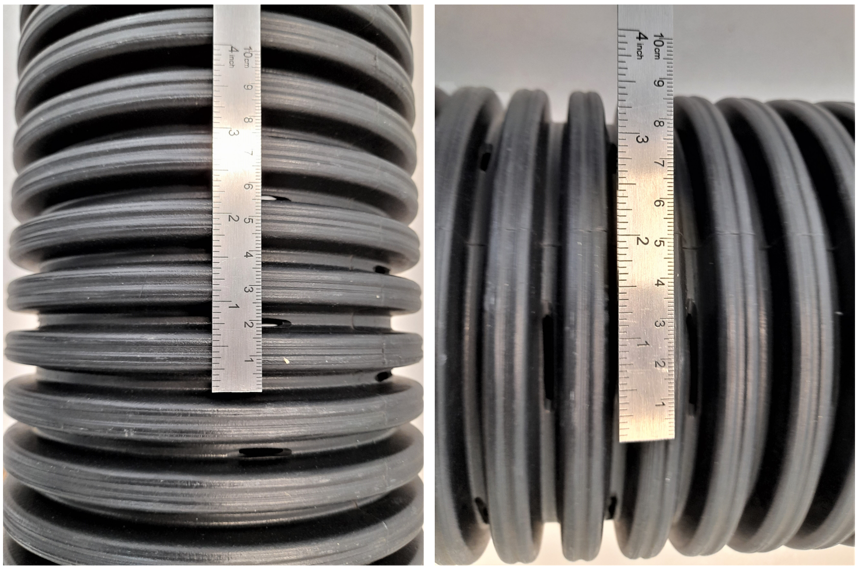

(a) (b)

Figure 7.9: Pipe perforation: (a) Axial distance between perforation; (b) Width of a single perforation

The experimental pipe geometry was replicated in a 3D FEM model in COMSOL multiphysics 6.0 with ideal soft boundary conditions at the interface of the perforation and Perfectly Matched Layer (PML) imposed at the end of the pipe away from the sound source. The sound source was modelled as a piston generating plane wave. The perforations were modelled as ellipses of constant cross sectional area. The results of the numerically and experimentally obtained transmission loss can be seen in Figure 7.10.

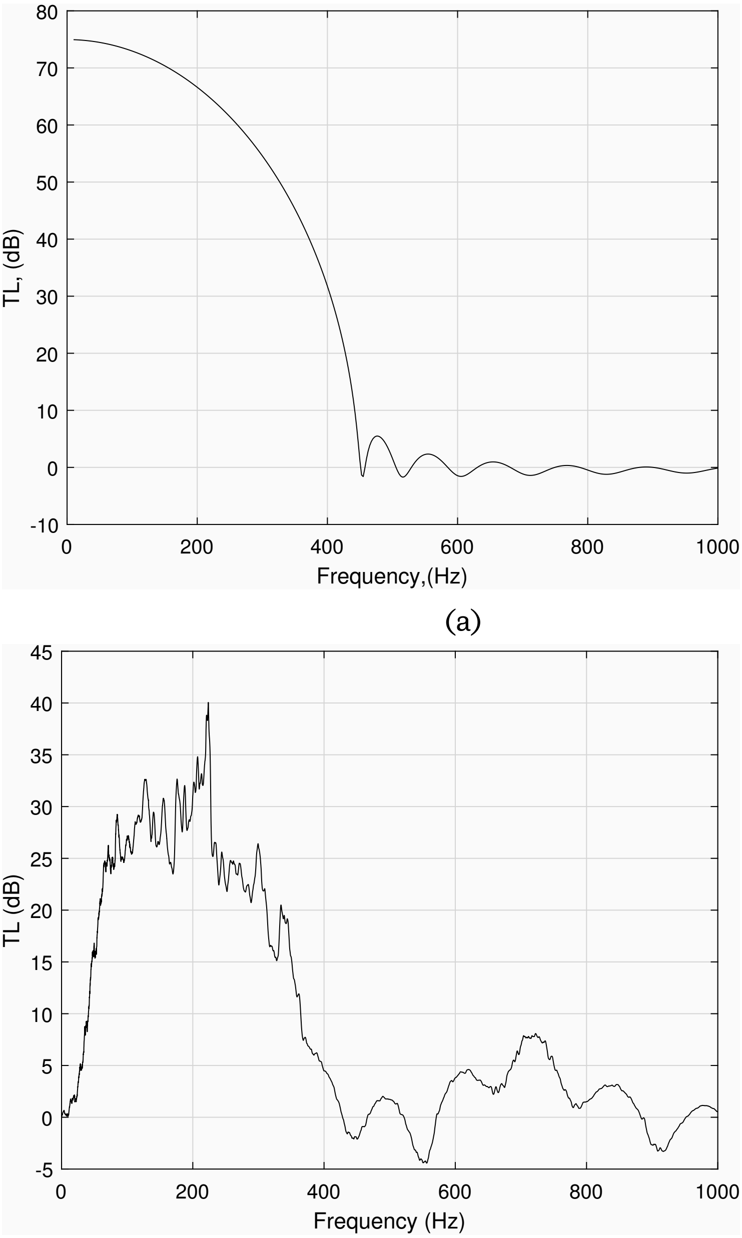

(a)

(b)

Figure 7.10: (a) Numerical and (b) Experimental plots of the Transmission Loss defined by equation (7.21)

The measured transmission loss illustrated in Figure 7.10(b) offers the evidence that the periodically arranged perforations in the rigid pipe create a low frequency band gap that extends to approximately 460 Hz. The width of this band gap matches that predicted for the simplified perforation geometry, i.e. where the perforations are idealised with an elliptical geometry in the 3D finite element model. It is evident, however, that the experimental data set is noisy and that the level of the experimental transmission loss is limited by the signal to noise ratio. This difference can also be attributed to a structure-borne vibrations excited in the wall of the pipe or sound leakage due to the experimental perforated pipe being open-ended. Despite this, it can be seen that the acoustically soft scattering phenomenon does occur when the pressure release condition is imposed on a non-rigidly backed perforation allowing for very low frequency attenuation of acoustic waves with a sample size much smaller than the wavelength of sound being attenuated.

7.6 Chapter Conclusion

An analytical model based upon the transfer matrix method has been developed to predict the acoustic attenuation in a pipe caused by a periodic array of non-rigidly backed perforations acting like acoustically soft scatterers. It has been shown that periodic arrays of acoustically soft scatterers produce a low frequency band gap from 0 Hz to an upper bound determined by the geometry of the perforations and the unit cell length. Acoustic waves within the frequency range of the band gap become evanescent causing a significant attenuation. As a result, there is no wave propagation in infinite pipe with perforation. Reducing the unit cell length, but keeping the total number of unit cells constant, increases the width of the gap, but does not increase the attenuation within the band gap. Increasing the size of the perforation increases the surface area where an acoustically soft boundary condition is present. This causes an increase in the width of the band gap and attenuation within it. Additionally, it is possible to adjust the width of the band gap and attenuation by changing the depth of the perforations. An increase in the perforation depth results in a reduction in the width of the band gap and attenuation achieved within it. All of these observations are numerically validated indicating in the ideal case the analytical model is valid. An experiment has been carried out to illustrate that the models predict the width of the band gap.

Chapter 8

Conclusion

The aims of this thesis were to investigate and develop broadband low frequency acoustic metamaterials for noise absorption and attenuation in one and two port systems, with a sample length much smaller than the wavelength being manipulated; develop analytical models to obtain simple expressions for the effective material properties of metamaterial structures to help gain an insight into the underlying physics; and to develop an acoustic metamaterial structure for very low frequency attenuation of noise in waveguides through the exploitation of novel acoustic phenomenon.

In chapter 3 a general effective property model has been proposed to obtain explicit analytical expressions for complex systems. By discretising a system into segments, it is possible to utilise the transfer matrix method to predict the acoustic properties in these segments. Through the application of linear superposition, these individual segment effective properties can be summated to achieve the total effective properties of the system. By taking the low frequency limit, simple analytical expressions for complex acoustic systems were obtained. It was shown that there was generally good agreement when in comparison to the results produced with TMM Multiplication method and numerically. However, all the effective property models fail to capture the evanescent coupling between Helmholtz resonators such that asymmetrical reflection properties are produced.

In Chapter 4 the mechanism to achieve perfect absorption for a one port system has been explored with the development of single frequency and broadband frequency perfect absorbing acoustic metamaterial unit cell. This was achieved at 290 Hz using a single Helmholtz resonator with a sample thickness of $\lambda/28$, and over a broadband frequency range between 275 and 625 Hz using a system of three Helmholtz resonators with a sample thickness of $\lambda/10$. The main premise that has been explored is on the use of porous inclusions to help optimise the acoustic properties of the Helmholtz resonators such that the system becomes critical coupled with the outer waveguide at each resonant frequency.

In Chapter 5 the mechanism to achieve asymmetrical perfect absorption in two port systems has been explored. Here, systems of coupled Helmholtz resonators were optimised by the inclusion of porous media within the cavity such that the critical coupling conditions were fulfilled and thus perfect absorption was obtained. This was undertaken at a single frequency of approximately 300 Hz through the use of two coupled Helmholtz resonators with a porous inclusion in the higher frequency resonator. The configuration of the geometry was such that at the critical frequency, impinging waves from one direction were perfectly absorbed, whilst waves impinging in the opposite direction were nearly perfectly reflected. The single frequency perfect absorber has a sample thickness of $\lambda/16$. This methodology was then extended to a broadband system in the frequency range of 300 Hz to 600 Hz. This utilised four coupled Helmholtz resonators. The utility of the porous inclusions was displayed by contrasting the system with and without the porous inclusions, highlighting the stark contrast in absorptive performance. Due to required coupling of the two lowest frequency resonators, it was shown through the use of the complex frequency plane plots of the eigenvectors that a system of this geometry can only exhibit $M-1$ critically coupled frequencies. The resulting broadband perfect absorber presented within this chapter exhibited perfect absorption at 312, 426 and 576 Hz, with a sample thickness of $\lambda/8$ at the lowest critically coupled frequency.

In Chapter 6 a method of simplification has been proposed for impedance terms derived by the TMM. This was applied to the case of a serial array of M coupled identical Helmholtz resonators. The simplification method is reliant upon the use of an impedance contrast to create a small order term which can be used in the Taylor expansion of the TMM impedance expressions. Upon analysis of the complex frequency domain of the modelled systems it was concluded that it is only possible to achieve critical coupling with one zero of the system, meaning perfect absorption at multiple frequencies is not possible. It was also found that the resonant frequencies of the systems can be obtained through the solution of the polynomials present within the numerator of the impedance approximations. However, it is evident that there is a slight discrepancy between the approximate resonant frequency equations and those achieved by the other methodologies. This is due to viscothermal loss effects not being taken in to account.

In Chapter 7 an ideal analytical model based upon the transfer matrix method has been developed to model the acoustic attenuation achieved by periodic arrays of non-rigidly backed perforations acting as sound-soft scatterers. It has been shown that periodic arrays of sound-soft scatterers produce a low frequency band gap from 0 Hz to a frequency determined by the geometry of the perforations and the unit cell length. Through extensive numerical modelling using two different numerical model variants to produce the soft-scatterer effect, it has been shown that two length corrections are required to account for the pressure radiation at the discontinuity between the perforation and the waveguide and outside free air. A revised analytical model was proposed which accounts for this fact and is in excellent agreement with the numerical model variant in which the perforated waveguide is encompassed by an air gap and PML. The experimental transmission loss highlights that periodically arranged holes in the rigid pipe create a low frequency band gap. The band gap produced experimentally matches the predictions obtained for the simplified numerical model in which the perforations were idealised with an acoustical soft backed elliptical geometry in the 3D finite element model.

Chapter 9

Bibliography

[1] Michael R. Haberman and Matthew D. Guild. Acoustic metamaterials. *Physics Today*, 69(6):42–48, jun 2016.

[2] Mathias Basner, Wolfgang Babisch, Adrian Davis, Mark Brink, Charlotte Clark, Sabine Janssen, and Stephen Stansfeld. Auditory and non-auditory effects of noise on health. *The Lancet*, 383(9925):1325–1332, apr 2014.

[3] Noureddine Atalla Jean F. Allard. *Propagation of Sound in Porous Media*. John Wiley & Sons, 2009.

[4] Trevor Cox and Peter D'Antonio. *Acoustic Absorbers and Diffusers, Third Edition*. Taylor and Francis Group, 2016.

[5] Joseph W. Sullivan and Malcolm J. Crocker. Analysis of concentric-tube resonators having unpartitioned cavities. *Journal of the Acoustical Society of America*, 64(1):207, feb 1978.

[6] Lee Fok, Muralidhar Ambati, and Xiang Zhang. Acoustic metamaterials. *MRS Bulletin*, 33(10):931–934, oct 2008.

[7] Guancong Ma and Ping Sheng. Acoustic metamaterials: From local resonances to broad horizons. *Science Advances*, 2(2):e1501595, feb 2016.

[8] Richard M. Christensen. *Mechanics of Composite Materials*. Dover Publications, 2005.

[9] Konstantin Y. Bliokh, Yury P. Bliokh, Valentin Freilikher, Sergey Savel'ev, and Franco Nori. Colloquium: Unusual resonators: Plasmonics, metamaterials, and random media. *Reviews of Modern Physics*, 80(4):1201–1213, oct 2008.

[10] Steven A. Cummer, Johan Christensen, and Andrea Alù. Controlling sound with acoustic metamaterials. *Nature Reviews Materials*, 1(3), feb 2016.

[11] Zhengyou Liu, Xixiang Zhang, Yiwei Mao, Y. Y. Zhu, Zhiyu Yang, C. T. Chan, and Ping Sheng. Locally resonant sonic materials. *Science*, 289(5485):1734–1736, sep 2000.

[12] Jensen Li, Xinhua Wen, and Ping Sheng. Acoustic metamaterials. *Journal of Applied Physics*, 129(17):171103, may 2021.

[13] V. Romero-García, G. Theocharis, O. Richoux, A. Merkel, V. Tournat, and V. Pagneux. Perfect and broadband acoustic absorption by critically coupled subwavelength resonators. *Scientific Reports*, 6(1), jan 2016.

[14] V. Romero-García, G. Theocharis, O. Richoux, and V. Pagneux. Use of complex frequency plane to design broadband and sub-wavelength absorbers. *The Journal of the Acoustical Society of America*, 139(6):3395–3403, jun 2016.

[15] N. Jiménez, W. Huang, V. Romero-García, V. Pagneux, and J.-P. Groby. Ultra-thin metamaterial for perfect and quasi-omnidirectional sound absorption. *Applied Physics Letters*, 109(12):121902, sep 2016.

[16] J.-P. Groby, W. Huang, A. Lardeau, and Y. Aurégan. The use of slow waves to design simple sound absorbing materials. *Journal of Applied Physics*, 117(12):124903, mar 2015.

[17] J.-P. Groby, R. Pommier, and Y. Aurégan. Use of slow sound to design perfect and broadband passive sound absorbing materials. *The Journal of the Acoustical Society of America*, 139(4):1660–1671, apr 2016.

[18] Noé Jiménez, Vicent Romero-García, Vincent Pagneux, and Jean-Philippe Groby. Quasiperfect absorption by subwavelength acoustic panels in transmission using accumulation of resonances due to slow sound. *Physical Review B*, 95(1), jan 2017.

[19] Junfei Li, Wenqi Wang, Yangbo Xie, Bogdan-Ioan Popa, and Steven A. Cummer. A sound absorbing metasurface with coupled resonators. *Applied Physics Letters*, 109(9):091908, aug 2016.

[20] Yong Li and Badreddine M. Assouar. Acoustic metasurface-based perfect absorber with deep subwavelength thickness. *Applied Physics Letters*, 108(6):063502, feb 2016.

[21] Min Yang, Shuyu Chen, Caixing Fu, and Ping Sheng. Optimal sound-absorbing structures. *Materials Horizons*, 4(4):673–680, 2017.

[22] Chi Zhang and Xinhua Hu. Three-dimensional single-port labyrinthine acoustic metamaterial: Perfect absorption with large bandwidth and tunability. *Physical Review Applied*, 6(6), dec 2016.

[23] C. Lagarrigue, J. P. Groby, V. Tournat, O. Dazel, and O. Umnova. Absorption of sound by porous layers with embedded periodic arrays of resonant inclusions. *The Journal of the Acoustical Society of America*, 134(6):4670–4680, dec 2013.

[24] J.-P. Groby, C. Lagarrigue, B. Brouard, O. Dazel, V. Tournat, and B. Nennig. Enhancing the absorption properties of acoustic porous plates by periodically embedding helmholtz resonators. *The Journal of the Acoustical Society of America*, 137(1):273–280, jan 2015.

[25] V. Romero-García, N. Jiménez, G. Theocharis, V. Achilleos, A. Merkel, O. Richoux, V. Tournat, J.-P. Groby, and V. Pagneux. Design of acoustic metamaterials made of helmholtz resonators for perfect absorption by using the complex frequency plane. *Comptes Rendus. Physique*, 21(7-8):713–749, jan 2021.

[26] Ting S. Luk, Salvatore Campione, Iltai Kim, Simin Feng, Young Chul Jun, Sheng Liu, Jeremy B. Wright, Igal Brener, Peter B. Catrysse, Shanhui Fan, and Michael B. Sinclair. Directional perfect absorption using deep subwavelength low-permittivity films. *Physical Review B*, 90(8):085411, aug 2014.

[27] Yves Aurégan. Ultra-thin low frequency perfect sound absorber with high ratio of active area. *Applied Physics Letters*, 113(20):201904, nov 2018.

[28] Guancong Ma, Min Yang, Songwen Xiao, Zhiyu Yang, and Ping Sheng. Acoustic metasurface with hybrid resonances. *Nature Materials*, 13(9):873–878, jun 2014.

[29] Valentin Leroy, Anatoliy Strybulevych, Maxime Lanoy, Fabrice Lemoult, Arnaud Tourin, and John H. Page. Superabsorption of acoustic waves with bubble metascreens. *Physical Review B*, 91(2):020301, jan 2015.

[30] Antonio A. Fernández-Marín, Noé Jiménez, Jean-Philippe Groby, José Sánchez-Dehesa, and Vicente Romero-García. Aerogel-based metasurfaces for perfect acoustic energy absorption. *Applied Physics Letters*, 115(6):061901, aug 2019.

[31] A. Merkel, G. Theocharis, O. Richoux, V. Romero-García, and V. Pagneux. Control of acoustic absorption in one-dimensional scattering by resonant scatterers. *Applied Physics Letters*, 107(24):244102, dec 2015.

[32] Pengjiang Wei, Charles Croënne, Sai Tak Chu, and Jensen Li. Symmetrical and anti-symmetrical coherent perfect absorption for acoustic waves. *Applied Physics Letters*, 104(12):121902, mar 2014.

[33] Jun Mei, Guancong Ma, Min Yang, Zhiyu Yang, Weijia Wen, and Ping Sheng. Dark acoustic metamaterials as super absorbers for low-frequency sound. *Nature Communications*, 3(1), jan 2012.

[34] C. E. Bradley. Time harmonic acoustic bloch wave propagation in periodic waveguides. part i. theory. *The Journal of the Acoustical Society of America*, 96(3):1844–1853, sep 1994.

[35] C. E. Bradley. Time harmonic acoustic bloch wave propagation in periodic waveguides. part II. experiment. *The Journal of the Acoustical Society of America*, 96(3):1854–1862, sep 1994.

[36] C. E. Bradley. Time-harmonic acoustic bloch wave propagation in periodic waveguides. part III. nonlinear effects. *The Journal of the Acoustical Society of America*, 98(5):2735–2744, nov 1995.

[37] Charles E. Bradley. Acoustic bloch wave propagation in a periodic waveguide. Technical report, jul 1991.

[38] N. Sugimoto and T. Horioka. Dispersion characteristics of sound waves in a tunnel with an array of helmholtz resonators. *The Journal of the Acoustical Society of America*, 97(3):1446–1459, mar 1995.

[39] Nicholas Fang, Dongjuan Xi, Jianyi Xu, Muralidhar Ambati, Werayut Srituravanich, Cheng Sun, and Xiang Zhang. Ultrasonic metamaterials with negative modulus. *Nature Materials*, 5(6):452–456, apr 2006.

[40] G Theocharis, O Richoux, V Romero García, A Merkel, and V Tournat. Limits of slow sound propagation and transparency in lossy, locally resonant periodic structures. *New Journal of Physics*, 16(9):093017, sep 2014.

[41] Yong Xu, Yi Li, Reginald K. Lee, and Amnon Yariv. Scattering-theory analysis of waveguide-resonator coupling. *Physical Review E*, 62(5):7389–7404, nov 2000.

[42] Taehwa Lee, Tsuyoshi Nomura, and Hideo Iizuka. Damped resonance for broadband acoustic absorption in one-port and two-port systems. *Scientific Reports*, 9(1), sep 2019.

[43] B.R. Mace. Reciprocity, conservation of energy and some properties of reflection and transmission coefficients. *Journal of Sound and Vibration*, 155(2):375–381, jun 1992.

[44] Houyou Long, Ying Cheng, and Xiaojun Liu. Asymmetric absorber with multiband and broadband for low-frequency sound. *Applied Physics Letters*, 111(14):143502, oct 2017.

[45] Noé Jiménez, Vicent Romero-García, Vincent Pagneux, and Jean-Philippe Groby. Rainbow-trapping absorbers: Broadband, perfect and asymmetric sound absorption by subwavelength panels for transmission problems. *Scientific Reports*, 7(1):13595, October 2017.

[46] Xue Jiang, Bin Liang, Rui qi Li, Xin ye Zou, Lei lei Yin, and Jian chun Cheng. Ultra-broadband absorption by acoustic metamaterials. *Applied Physics Letters*, 105(24):243505, dec 2014.

[47] Yuchi Yu, Han Jia, Yuzhen Yang, Han Zhao, Quanquan Shi, Peng Kong, Jun Yang, and Ke Deng. Multi-order resonators for acoustic multiband asymmetric absorption and reflection. *Journal of Applied Physics*, 131(13):135102, apr 2022.

[48] Pyung-Sik Ma, Hyun-Sil Kim, Seong-Hyun Lee, and Yun-Ho Seo. Quasi-perfect absorption of broadband low-frequency sound in a two-port system based on a micro-perforated panel resonator. *Applied Acoustics*, 186:108449, jan 2022.

[49] Jessica R. Piper, Victor Liu, and Shanhui Fan. Total absorption by degenerate critical coupling. *Applied Physics Letters*, 104(25):251110, jun 2014.

[50] V. Romero-García, N. Jiménez, J.-P. Groby, A. Merkel, V. Tournat, G. Theocharis, O. Richoux, and V. Pagneux. Perfect absorption in mirror-symmetric acoustic metascreens. *Physical Review Applied*, 14(5):054055, nov 2020.

[51] Min Yang, Chong Meng, Caixing Fu, Yong Li, Zhiyu Yang, and Ping Sheng. Subwavelength total acoustic absorption with degenerate resonators. *Applied Physics Letters*, 107(10):104104, sep 2015.

[52] Sam Hyeon Lee, Choon Mahn Park, Yong Mun Seo, Zhi Guo Wang, and Chul Koo Kim. Acoustic metamaterial with negative modulus. *Journal of Physics: Condensed Matter*, 21(17):175704, mar 2009.

[53] Jiangyi Zhang, Vicente Romero-García, Georgios Theocharis, Olivier Richoux, Vassos Achilleos, and Dimitrios J. Frantzeskakis. Second-harmonic generation in acoustic waveguides loaded with an array of side holes. *Acta Acustica united with Acustica*, 104(2):235–242, mar 2018.

[54] Sam Hyeon Lee, Choon Mahn Park, Yong Mun Seo, Zhi Guo Wang, and Chul Koo Kim. Composite acoustic medium with simultaneously negative density and modulus. *Physical Review Letters*, 104(5):054301, feb 2010.

[55] Yvan Champoux and Michael R. Stinson. On acoustical models for sound propagation in rigid frame porous materials and the influence of shape factors. *The Journal of the Acoustical Society of America*, 92(2):1120–1131, aug 1992.

[56] Sang-Hyun Seo and Yang-Hann Kim. Silencer design by using array resonators for low-frequency band noise reduction. *The Journal of the Acoustical Society of America*, 118(4):2332–2338, oct 2005.

[57] Uno Ingard. On the theory and design of acoustic resonators. *The Journal of the Acoustical Society of America*, 25(6):1037–1061, nov 1953.

[58] R. Martínez-Sala, J. Sancho, J. V. Sánchez, V. Gómez, J. Llinares, and F. Meseguer. Sound attenuation by sculpture. *Nature*, 378(6554):241–241, nov 1995.

[59] M. Sigalas and E.N. Economou. Band structure of elastic waves in two dimensional systems. *Solid State Communications*, 86(3):141–143, apr 1993.

[60] F. R. Montero de Espinosa, E. Jiménez, and M. Torres. Ultrasonic band gap in a periodic two-dimensional composite. *Physical Review Letters*, 80(6):1208–1211, feb 1998.

[61] J.-P. Groby. A. Cebrecos, V. Romero-Garcia. Acoustic metamaterials and sonic crystals: Block 2(a): Introduction to the brillouin zone and plane wave expansion. In *EAA Summer School*, Leuven, September 2019.

[62] A. Srikantha Phani, J. Woodhouse, and N. A. Fleck. Wave propagation in two-dimensional periodic lattices. *The Journal of the Acoustical Society of America*, 119(4):1995–2005, apr 2006.

[63] G. Floquet. Sur les équations différentielles linéaires à coefficients périodiques. *Annales scientifiques de l'École normale supérieure*, 12:47–88, 1883.

[64] Daniel Peter Elford. *Band Gap Formation in Acoustically Resonant Phononic Crystals*. PhD thesis, Loughborough University, 2010.

[65] Sir Lawrence Bragg. *The Crystalline State*. G. BELL AND SONS LTD, 1933.

[66] Michael R. Stinson. The propagation of plane sound waves in narrow and wide circular tubes, and generalization to uniform tubes of arbitrary cross-sectional shape. *The Journal of the Acoustical Society of America*, 89(2):550–558, feb 1991.

[67] David Linton Johnson, Joel Koplik, and Roger Dashen. Theory of dynamic permeability and tortuosity in fluid-saturated porous media. *Journal of Fluid Mechanics*, 176(-1):379, mar 1987.

[68] Yvan Champoux and Jean-F. Allard. Dynamic tortuosity and bulk modulus in air-saturated porous media. *Journal of Applied Physics*, 70(4):1975–1979, aug 1991.

[69] Bryan H. Song and J. Stuart Bolton. A transfer-matrix approach for estimating the characteristic impedance and wave numbers of limp and rigid porous materials. *The Journal of the Acoustical Society of America*, 107(3):1131–1152, mar 2000.

[70] O Richoux and V Pagneux. Acoustic characterization of the hofstadter butterfly with resonant scatterers. *Europhysics Letters (EPL)*, 59(1):34–40, jul 2002.

[71] J. Kergomard and A. Garcia. Simple discontinuities in acoustic waveguides at low frequencies: Critical analysis and formulae. *Journal of Sound and Vibration*, 114(3):465–479, may 1987.

[72] V Dubos, Jean Kergomard, Ali Khettabi, Jean-Pierre Dalmont, D.H. Keefe, and C.J. Nederveen. Theory of sound propagation in a duct with a branched tube using modal decomposition. *Acta Acustica united with Acustica*, 85:153–169, 03 1999.

[73] O. C. Zienkiewics. *The finite element method*. Elsevier/Butterworth-Heinemann, 2005.

[74] W.R. Kampinga. *Viscothermal accoustics using finite elements*. PhD thesis.

[75] Qing-Huo Liu and Jianping Tao. The perfectly matched layer for acoustic waves in absorptive media. *The Journal of the Acoustical Society of America*, 102(4):2072–2082, oct 1997.

[76] *COMSOL Multiphysics User's Guide, Version 4.3*.

[77] *BS EN ISO 10534-2:2001 Acoustics - Determination of sound absorption coefficient and impedance in impedance tubes - part 2: transfer function method. s.l.*, 2001.

[78] MARTIN WOLKESSON. Evaluation of impedance tube methods -a two microphone in-situ method for roadsurfaces and the three microphone transfer-function method for porous materials. Master's thesis, CHALMERS UNIVERSITY OF TECHNOLOGY, 2013.

[79] American Society for Testing and Materials. *ASTM E2611 – Standard Test Method for Normal Incidence Determination of Porous Material Acoustical Properties Based on the Transfer Matrix Method*, 2017.

[80] Edoardo A. Piana, Nicolaas Bernardus Roozen, and Chiara Scrosati. Impedance tube measurements on the denorms roundrobin test material samples. In *26th Internation Congress on Sound and Vibration*, 2019.

[81] Kévin Verdière, Raymond Panneton, Saïd Elkoun, Thomas Dupont, and Philippe Leclaire. Transfer matrix method applied to the parallel assembly of sound absorbing materials. *The Journal of the Acoustical Society of America*, 134(6):4648–4658, dec 2013.

[82] Kirill V. Horoshenkov, Alistair Hurrell, and Jean-Philippe Groby. A three-parameter analytical model for the acoustical properties of porous media. *The Journal of the Acoustical Society of America*, 145(4):2512–2517, apr 2019.

[83] P. D. C. King and T. J. Cox. Acoustic band gaps in periodically and quasiperiodically modulated waveguides. *Journal of Applied Physics*, 102(1):014902, jul 2007.

[84] A. Dell, A. Krynkin, and K.V. Horoshenkov. The use of the transfer matrix method to predict the effective fluid properties of acoustical systems. *Applied Acoustics*, 182:108259, Nov 2021.

[85] M. L. Munjal, F. P. Mechel, Michael Vorländer, Peter Költzsch, and Martin Ochmann. *Formulas of Acoustics*. Springer London, Limited, 2008.

[86] MathWorks. lsqnonlin. https://uk.mathworks.com/help/optim/ug/lsqnonlin.html.

[87] A. I. Komkin, M. A. Mironov, and A. I. Bykov. Sound absorption by a helmholtz resonator. *Acoustical Physics*, 63(4):385–392, jul 2017.

[88] M.B. Xu, A. Selamet, and H. Kim. Dual helmholtz resonator. *Applied Acoustics*, 71(9):822–829, sep 2010.

[89] Chenzhi Cai and Cheuk Ming Mak. Acoustic performance of different helmholtz resonator array configurations. *Applied Acoustics*, 130:204–209, jan 2018.

[90] Chenzhi Cai and Cheuk Ming Mak. Hybrid noise control in a duct using a periodic dual helmholtz resonator array. *Applied Acoustics*, 134:119–124, may 2018.

[91] D.P. Jena, J. Dandsena, and V.G. Jayakumari. Demonstration of effective acoustic properties of different configurations of helmholtz resonators. *Applied Acoustics*, 155:371–382, dec 2019.

[92] Rasha Al Jahdali and Ying Wu. Coupled resonators for sound trapping and absorption. *Scientific Reports*, 8(1), sep 2018.

[93] Chenzhi Cai, Cheuk Ming Mak, and Xu Wang. Noise attenuation performance improvement by adding helmholtz resonators on the periodic ducted helmholtz resonator system. *Applied Acoustics*, 122:8–15, jul 2017.

[94] Philip M. Morse and K. Uno Ingard. *Theoretical Acoustics*. Princeton University Press, 1968.

[95] I. Lee. *Acoustic Characteristics of Perforated Dissipative and Hybrid Silencers*. PhD thesis, The Ohio State University, 2005.

[96] A. Krynkin and P. McIver. Approximations to wave propagation through a lattice of dirichlet scatterers. *Waves in Random and Complex Media*, 19(2):347–365, Jun 2009.

[97] A. Dell, A. Krynkin, K. V. Horoshenkov, and G. Sailor. Low frequency attenuation of acoustic waves in a perforated pipe. *The Journal of the Acoustical Society of America*, 153(3):1791–1801, mar 2023.

[98] Finn Jacobsen and Virginie Jaud. A note on the calibration of pressure-velocity sound intensity probes. *The Journal of the Acoustical Society of America*, 120(2):830–837, aug 2006.